1989

THE NITRIDING OF HIGH SPEED STEEL CUTTING TOOLS

Crust, Glen Alexander

http://hdl.handle.net/10026.1/2379

http://dx.doi.org/10.24382/1527
University of Plymouth

THE NITRIDING OF HIGH SPEED STEEL CUTTING TOOLS.

by

Glen Alexander Crust

Department of Mechanical Engineering
Polytechnic South West.

A thesis submitted to the Council for National Academic Awards in partial fulfilment of the requirements for the degree of Doctor of Philosophy.

April 1989.

The Nitriding Of High Speed Steel Cutting Tools.

G.A. Crust.

Abstract.

There is an interest in industry in cost reduction. Tool wear constitutes an important element in the cost of many metal working processes, not only because of the cost of the tool, but also because of the cost of machine downtime.

Saltbath nitriding of high speed steel tools adds only about 1% to the cost of a finished tool, but has been found to confer benefits considerably in excess of this over a range of cutting conditions.

A series of cutting tests is described, during which cutting forces and tool temperatures were recorded simultaneously using microcomputer based instrumentation developed at the Polytechnic as part of this study.

The shear mechanism for tools with a nose radius is investigated, and methods for evaluating the primary shear plane area are proposed and discussed. The variation in primary shear plane area with chip flow angle is evaluated.

The method for predicting chip flow angle from tool geometry is presented, and results from this analysis compared with experimental data.

A method for predicting primary shear angle from tool geometry, force measurements and workpiece material properties is developed.

A number of methods for measuring tool temperature are described. Temperature distributions obtained from finite element heat transfer analysis are presented, and a mechanism for the catastrophic failure of the toolnose is proposed.

A range of cutting conditions is described, over which the performance of high speed steel cutting tools is enhaced by saltbath nitriding.

Acknowledgements.

I am grateful to David Grieve, my director of studies, for his advice, support and flexibility during the course of this study. I would also like to thank David Short and David Plane for their assistance.

I very much appreciate the guidance provided by Dr S.M. Grove during numerous useful discussions concerning heat transfer modelling and mathematics, and by Dr J.M. Davies concerning mathematics and the use of the computer.

I am particularly grateful to Robin Crocker whose technical skill and patience were central to the successful completion of a great deal of experimental work.

Thanks also to Dr A.B. Smith (Department of Manufacturing Engineering, Loughborough University) for his help in the initial stages of the project, and to Dr P. O'Calaghan (School of Mechanical Engineering, Cranfield Institute of Technology) for informative discussions concerning boundary heat transfer.

Notation.

Aps	primary shear plane area
Ass	secondary shear plane area
Ff	frictional (secondary shear) force
Fn	normal force
Fs	primary shear force
Ft	Tangential force (= Fn when α = 0)
Ftf	secondary shear component of Ft
Fts	primary shear component of Ft
k	critical shear stress
l	undeformed chip length
lc	chip length
p	normal pressure
t	undeformed chip thickness
tc	chip thickness
va	chip velocity
vb	surface speed
vs	primary shear velocity
ϕ	primary shear angle
α	rake angle
τs	interface shear stress
γ	chip flow angle (see section 2.6.1)
μ	frictional coefficient (= tan Ψ)
Ψ	friction angle

Contents.

Page.

Page.

Page.

Page.

Page.

Page.

List Of Figures.

Chapter 1. Introduction.

1.1 Heat Treatment Of Tool Steels.

Tool steels were developed to maintain room temperature hardness at high temperatures. This is achieved by various alloying additions and heat treatment, leading to a fine grained martensitic structure. Several secondary hardening cycles are carried out in order to reduce the amount of austenite retained in the steel at room temperature.

1.2 Surface Heat Treatment.

For some applications it is desirable to harden only an outer layer of the steel while retaining a softer, tough ductile core to provide resistance to shock loading. To do this, the outside of the tool is subjected to rapid heating followed by rapid cooling as the heat is transfered to the bulk of the material. Laser hardening is such a process in which the heat is supplied by laser light [1]. In spark hardening [2] the case formed benefits from the transfer of tungsten carbide from the electrode. Alternatively, suitable elements, such as boron or nitrogen may be diffused into the surface layers.

1.3 Carbide Inclusions.

Precipitated carbide grains are another important feature of modern tool steels. Metal carbide grains have high hardness values, indicated in table 1.1, and, distributed throughout the microstructure in the form of fine particles bonded securely to the martensitic matrix, increase a tool steel's resistance to abrasive wear.

Table 1.1. Hardness Of Metal Carbides.

Material	Vickers Hardness Number
WC	2600
W_2C	2200
Mo_2C	1500
VC	2800
TiC	3200
B_4C	3700
SiC	2600
$(Fe,Cr)_7C_3$	1200-1600

The size of the carbide inclusions must be small, since large grains tend to increase internal stresses in the steel. Typically the maximum size of a carbide grain is 5 - 10 μm.

1.4 Thermochemical Treatments

There are a large number of thermochemical treatments available. These may be broken down into two main types - coating and diffusion processes. Coating processes result in the deposition of a thin metallic or ceramic layer on the surface of the steel. This may be achieved in a number of ways, including vapour deposition [3], powder coating [4], flame spraying [5], electroplating [6] and sputtering [7].

Diffusion processes rely on the introduction of elements including sulphur, nitrogen, carbon, silicon, boron, aluminium, and chromium into the steel by diffusion at elevated temperatures. These may then occupy interstices in the lattice or form refractory compounds with those elements already present in the steel.

Ion implantation increases the efficiency of the diffusion process by accelerating ions in a field of 100 - 200 KeV, producing a case depth of 0.1 μm. Both metallic and nonmetallic (principally nitrogen) ions may be implanted [8].

1.5 Nitriding.

1.5.1 Introduction

Nitriding is a term used to describe a number of industrial thermochemical processes used to introduce nitrogen into the surface layers of a metal, particularly steels. It is of particular interest in engineering, providing a surface with increased wear resistance and high fatigue strength.

Because of the low atomic radius of nitrogen (74pm) compared with the lattice spacing of body centred cubic iron (287pm) nitrogen may be retained interstitially in a steel. The nitrogen may also react with the iron and those alloying elements present in the steel to form nitrides and carbonitrides. Some of these are insoluble in the martensitic matrix typical of a tool steel at room temperature and may be observed as discrete precipitate particles under suitable magnification.

A large number of papers have been published describing the influence of nitriding on the tribological properties of mild steel and various austenitic steels [9,10,11,12,13]. The effect of nitriding on high alloy steels differs in a number of ways.

More specifically :-

(i) The diffusion layer formed in high alloy steels is less deep.

(ii) Owing to nitride formation with alloying elements (see 1.9) less interstitial nitrogen is found in the diffusion layer of high alloy steels.

(iii) There is no formation of a white layer during the saltbath nitriding of high alloy steels. This is not the case when treating mild steel or austenitic stainless steels.

The wear resistance of nitrided tools is often greatly increased. Results from a combination of ion implantation and nitriding [14] demonstrate a reduction in wear of up to two orders of magnitude. Auger electron spectrography and ion sputtering reveal contamination by oxygen and carbon and this is thought to contribute to the improvement in performance.

Opitz and Konig reported an increase in useful life of twist drills of up to thirty fold in some operations [15]. However a detrimental effect on the performance of high speed steel taps [16] has been reported, as has a softening of the nitrided layer at 500 °C [17].

1.5.2 Iron Nitrogen Phase Equilibria.

The solubility of nitrogen in the various phases of the iron nitrogen system has been reported. Nitrogen is soluble in alpha iron, with a maximum solubility of 0.10 wt % at 590 °C [18]. Solubilities at lower temperatures have also been measured using technical iron and values of 0.001, 0.005, 0.01, and 0.02 wt % N reported at temperatures of 100, 200, 300, and 400 °C respectively [19,20,21], (figure 1.1).

A number of discreet phases exist in the iron nitrogen system.

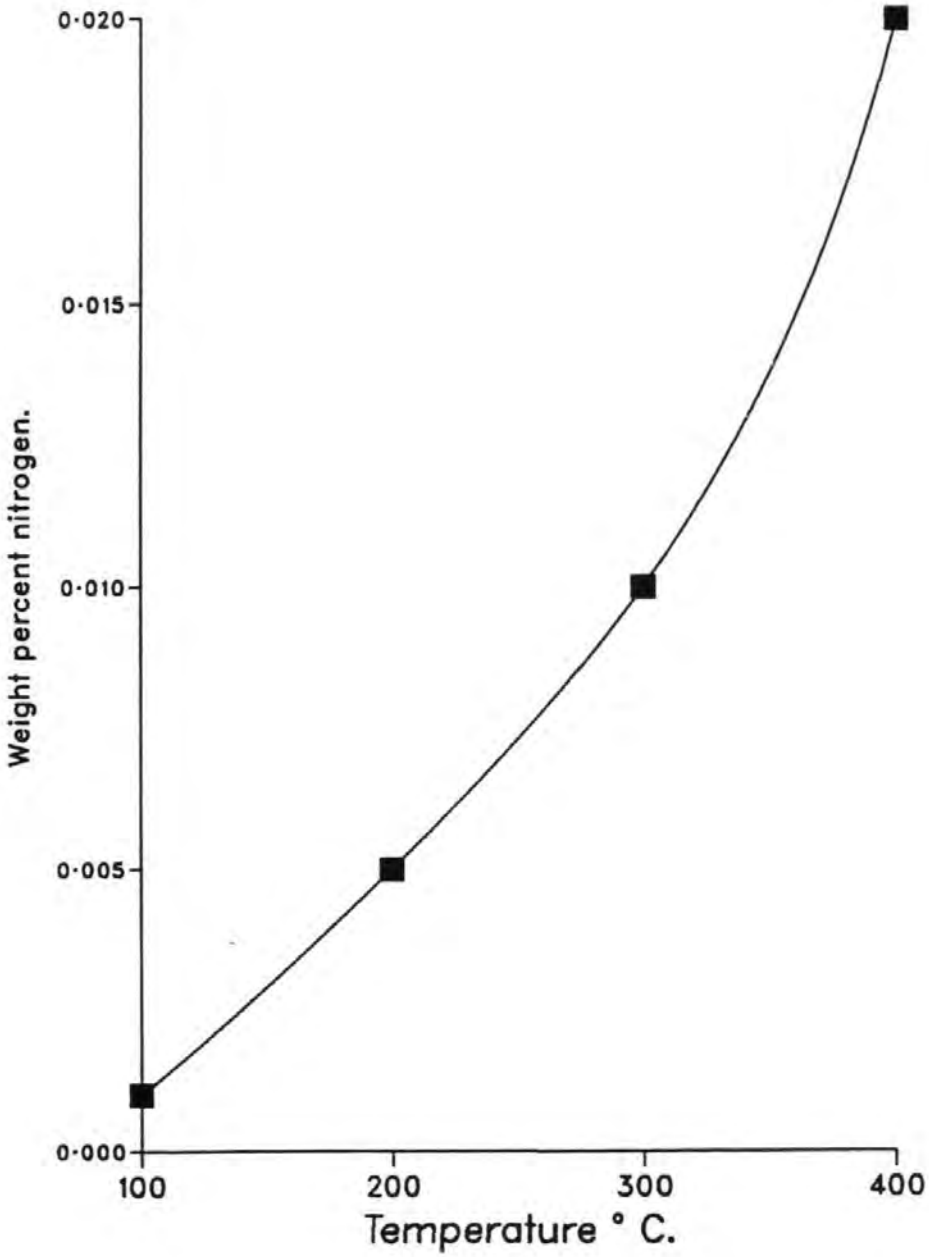

Figure 1.1 Solubility Of Nitrogen In Iron.

1.5.2.1 Alpha Phase.

The lattice parameter for this phase is practically identical with that of alpha iron [22,23,25].

1.5.2.2 Gamma Phase.

This phase is isomorphous with the gamma phase in the iron carbon system (austenite) and contains nitrogen randomly distributed in the interstices of the f.c.c. iron lattice. The lattice parameter is dependent on the composition of the phase and varies from a = 0.3594 nm at 0.81 wt. % N to a = 0.3646 nm at 2.33 wt % N [26].

1.5.2.3 Gamma Prime Phase.

This phase (Fe_4N) has a f.c.c. structure with nitrogen retained interstitially in an ordered pattern throughout the lattice [27,18], occupying one set of octahedral interstices. The lattice parameter is again composition dependent, varying from a = 0.3791 nm to a = 0.3801 nm [18].

1.5.2.4 Epsilon Phase.

The epsilon phase is h.c.p. with an ordered arrangement of nitrogen atoms [28]. Lattice parameters vary with composition from a = 0.2660 nm, c = 0.4344 nm, c/a = 1.633 at 5.7 wt % N to a = 0.2764 nm, c = 0.4420 nm, c/a = 1.599 at 11.0 wt. % N [28].

1.5.2.5 Zeta Phase.

The crystal structure of this phase (Fe N) is orthorhombic with an ordered arrangement of nitrogen atoms. The lattice parameters are a = 0.2764 nm, b = 0.4829 nm and c = 0.4425 nm [28].

1.6 Nitriding Techniques.

1.6.1 Gas Nitriding.

A method for case hardening iron and steel was patented in 1908 by Adolph W. Machlet in Elizabeth, New Jersey. His process involved the flow of ammonia over the material to be hardened at 480 to 980 °C. This formed the basis of the modern gas nitriding technique. Virtually any steel can be nitrided, but steels containing aluminium, chromium, vanadium, and molybdenum are most suitable, if increased hardness is required, as these elements form harder nitrides than iron.

Nitrogen released by the dissociation of ammonia

$$2NH_3 \xrightarrow{2Fe} 2FeN + 3H_2$$

becomes available at the metal surface, from where it is free to diffuse into the surface layers of the material.

However, contemporary gas nitriding is carried out with careful control of temperature and measured addition of hydrogen to the nitriding atmosphere. This has the beneficial effect of minimising the nucleation of the gamma prime and epsilon nitrides which form the white layer [29], discussed in section 1.7.1.

1.6.2 Ion Nitriding.

Ion nitriding [14] involves the introduction of nitrogen into the metal in the form of nitrogen cations. These are formed in a low pressure reactor, in which a large potential is maintained between the work and reactor wall. Nitrogen cations accelerated by this potential cause sufficient heating on collision with the metal surface for diffusion to occur.

This process is extremely flexible, since the composition and pressure of the nitriding atmosphere may be controlled as well as the temperature and process time. Because of the low nitriding potential, there is no problem with gamma prime phase white layer formation. Systems for ion nitriding have been commercially available since 1973, but are not widely used.

1.6.3 Salt Bath Nitriding.

A variety of fused salt baths are used for nitriding. Early salt baths contained high concentrations of cyanide salts and were, as a consequence unpleasant to use, producing extremely toxic waste. Typically the composition of these early baths was around 40 % KCN, 40 % KCNO, 20 - 30 % K_2CO_3. Such a bath would be operated at about 570 °C with frequent checks on composition, since small changes reduced operational efficiency considerably.

A number of variations on this theme have been investigated. Reducing the cyanide content is a particularly important consideration, as well as minimising running costs by reducing the temperature and process time. Liquid pressure salt baths, in which anhydrous ammonia is injected into the sealed bath at pressures of 7000 - 185000 Pa have also been developed,as have aerated baths.

1.6.4 The Tufftride Process.

The nitriding process used in the experimental studies described below was Tufftride TF1, a saltbath ferritic nitrocarburising process. The saltbath itself contains only 2.8 % cyanide and 35 % cyanate salts by weight and operates at around 580 °C. The cyanate is broken down catalytically by the ferrous component being treated, releasing nitrogen at the component surface.

$$4KNO \xrightarrow{Fe} K_2CO_3 + 2KCN + CN + CO + N$$

The process was chosen for a variety of reasons. By comparison with ion and plasma nitriding, saltbath nitriding is well understood. There are comparatively few control parameters to be adjusted in any saltbath process, so consistent results are easily maintained.

Finally, short process time and low running temperature contribute to the popularity of this process, both by minimising distortion of the treated components and reducing costs.

A brief summary of nitriding processes is presented in table 1.2.

Table 1.2. A Summary Of Nitriding Processes.

Process	Media	Normal Nitriding Temperature (°C)	Normal Nitriding Time	Diffused Elements
Gas nitriding	(i) Ammonia	490 - 510	up to 100 h	N, H
	(ii) Ammonia + H (+ N) (two stage process)	520 - 565	up to 30 h	N, H
Rapid gas nitriding	Ammonia + C (or C + O) releasing agent (S - releasing also possible.)	570 - 580	up to 6 h	N, H, C, (O, S)
Salt bath nitriding	(i) Cyanate/cyanide/ carbonate	570 - 580	(3 min) 2 - 4 h	N, C, O
	(ii) Cyanate/cyanide with S - releasing compounds.	570 - 580		N, C, O, S
Powder nitriding	Calcium cyanide and activator	470 - 480	up to 25h	N, H, C, O
Plasma nitriding	Ammonia	(350)	10 min to 36 h	N, H
	Nitrogen	450 - 600		N
	Nitrogen + C releasing gas (e.g. methane)			N, C

1.7 Structure Of The Nitrided Zone.

The case produced during nitriding may be divided into a number of zones, the presence and properties of which depend on the process used.

1.7.1 The White Layer.

In some processes, notably gas nitriding, an external layer which appears white under an optical microscope may be formed [24]. This has been studied by other workers during the nitriding of a stainless steel using ammonia and was found to consist of massive CrN precipitates containing epsilon and gamma prime phase iron (and nickel) nitrides. For a plain carbon steel the white layer is somewhat simpler, being formed by the precipitation of predominantly gamma prime phase iron nitride on the cooling of nitrogen - saturated austenite.

The unit cell dimensions of the precipitated phase are sufficiently larger than those of austenite to cause the gamma prime phase to grow in compression. As the layer increases in thickness some stress relaxation occurs at the free surface and a bending force across the thickness of the layer results, tending to lift the layer outwards and cause cracking.

This is not a problem when nitriding a steel such as BT42 using a relatively low temperature salt bath. At these temperatures the solubility of nitrogen in steels is sufficiently low for precipitated nitrogen to form gamma phase nitride. Martensitic steel has a more strained structure and this will inhibit the diffusion of nitrogen into high alloy steels such as BT42, again leading to conditions favouring the deposition of the gamma phase on cooling. The lattice parameter for gamma phase iron nitride is less than that for the gamma prime phase (see 1.5.2) and a less strained layer is formed with a more coherent substrate boundary.

1.7.2 The Compound Layer.

During saltbath nitriding carbon also diffuses into the surface layers of the material, but is less mobile. This carbon forms iron carbide particles which act as nuclei for the precipitation of epsilon iron nitride which forms the compound layer. Mitchell and Dawes [30] found that the best antiscuffing properties are obtained when the compound layer consists of a hexagonally close - packed phase of variable carbon and nitrogen concentrations.

Examination of an appropriate isothermal section through the Fe - C - N phase diagram [31] indicates epsilon iron carbonitride to be the phase in question.

Traces of nitrogen below the depth of the compound zone further enhance the wear resistance of the steel by occupying the interstitial lattice sites, strengthening the material further and providing increased resistance to fatigue.

1.8 Tool Steels

1.8.1 Low Alloy Carbon Steels.

Carbon steels derive their hardness from the martensitic transition. In carbon steels tempering occurs above 250 C, and so carbon steels are unsuitable for most metal cutting operations. The addition of alloying elements to carbon steel increases the tempering temperature allowing the steel to be used for metal cutting.

1.8.2 Alloying Elements.

Although alloying elements perform a variety of functions, their influence on the hardenability and red hardness of a steel are probably the two most important. Two of the alloying elements found commonly in tool steels influence red hardness considerably. These elements are tungsten and molybdenum. Thus two grades of tool steel have been developed, the M and T series, deriving their red hardness from molybdenum and tungsten respectively.

A number of the alloying elements used in tool steels, set out in table 1.3 [32] form refractory nitrides, and this effect is utilised in the nitriding process.

Table 1.3. Properties Of Alloying Elements In Steels.

Element	Influence on hardenability during heat treatment.	Other functions
Chromium	Increases	With high [C] resists abrasion and wear.
Cobalt	Decreases	Increases cutting ability considerably, improves red hardness.
Manganese	Increases	Reduces brittleness by combining with sulphur.
Molybdenum	Strongly increases	Eliminates temper brittleness, promotes red hardness.
Nickel	Slightly increases	Increases tendency to retain austenite.
Titanium	With carbide reduces	Prevents the formation of austenite in high Cr steel.
Vanadium	Very strong increase	Encourages fine grain in tool steels, forms hard abrasion resistant particles in HSS, gives marked secondary hardening.

1.9 Behaviour of Alloying Elements During Nitriding.

Nitriding is a precipitation hardening process, although X-ray diffraction studies indicate the presence of nitrogen regularly distributed within the Fe N lattice, which would cause further hardening due to lattice straining. Such straining is also consistent with the brittle nature of Fe N. Nitriding avoids the dimensional changes that result from the austenite/martensite transformation involved in normal heat treatment.

1.9.1 Nitride Formation

Nitrides are formed by one of two processes [24].

(i) The reaction of metals

i.e. $xM + yN \longrightarrow M_xN_y$

(ii) The reaction of carbides

i.e. $MC + N \longrightarrow MN + C$

or $N_2 + M_2C \longrightarrow MCN + MN$

The probability of carbide - nitride transformations decreases through the series Zr, Si, Hf, Ti, V, Nb, Mn, Cr, Fe. At concentrations less than 2% Mo, W, and Cr tend to form nitrides by scheme (i).

A third group may be identified whose members form nitrides by both schemes. It contains Cr at concentrations greater than 2 %, and V.

Elements forming nitrides by reaction (ii) require a minimum concentration of nitrogen in solid solution of between 10^{-2}% and 10^{-9}%. Vanadium requires about 10^{-3}% for the VC - VN reaction but only about 10^{-5}% to 10^{-7}% for the V - VN. Since about 90 % of the vanadium present in steel is present as carbide, however, the higher concentration is required for nitride formation.

Better nitriding is obtained after a relatively low temperature temper since some elements such as Cr, Mo, and W remain in solid solution and form nitrides preferentially from this state.

1.9.2 Physical Properties of Nitrides.

The physical properties of the nitrides are high melting points [33], low thermal conductivity and high microhardness [34]. Typical melting point and hardness values are shown in table 1.4.

Table 1.4. Physical Properties Of Metal Nitrides.

	Melting points (°C)	Microhardness (VPN)
TiN	2949	2000
VN	2177	1500
NbN	2050	1400
CrN	1450	1090
WN	< 800 *	
ZrN	2982	1520
HfN	3310	1640
Mn_5N_2, Mn_2N	900 *	

* indicates decomposition temperature.

1.10 Nitrogen In Metals.

1.10.1 General Use.

For some time nitrogen has been used to reduce wear in components subject to large dynamic contact forces, such as camshafts and gears. Drop hammers have shown an improvement in useful life of 400 % after nitriding [35].

1.10.2 Work On Tools.

Literature describing various aspects of nitriding of tool steels is available. Increased tool life following nitriding has been reported during turning [15], twist drilling and reaming operations using a variety of work materials and lubricants [16].

1.10.3 General Form Of Studies To Date.

Topics related to the effect of nitriding on the wear of HSS cutting tools have been studied by a few authors. Some papers have been published containing information on the improved performance of surface treated and nitrided tools [16,17]. Studies of the occurrence, [36,37] physical properties [24,38] and behaviour [32] of nitrides in steel are available in the literature.

However, although the mechanisms underlying the improvement in wear resistance are partly understood [32,39], little has been published correlating the improvement in tool performance with the factors responsible for the action of these mechanisms. It is this gap in the literature that this study is intended to fill.

1.11 Wear Tests.

A vast range of wear tests are available both to simulate working conditions and to isolate wear resulting from particular mechanisms. However, as many factors have an influence on wear it is frequently difficult to isolate individual mechanisms.

1.11.1 Use Of Standards.

A British and international standard, BS 5623:1979 ISO 3685 "Tool Life Testing With Single Point Turning Tools " is available as a set of guidelines for tool wear investigations. While acting as a useful standard, particularly for the presentation of results, it is not suitable for all studies.The following standards were of use in this study.

BS 5623:1979	Tool Life Testing With Single Point Turning Tools.
BS 4659:1971	Tool Steels.
BS 4139:1980	part 1 Indexable Inserts.
	part 7 Insert Toolholders .
BS 3002/1:1982	Tool Geometry.

1.11.2 Single Point Turning.

In this study single point turning tests were performed in order to assess the tribological performance of the treated surface. The geometric simplicity of the system produces forces which may be easily resolved into components relative to the cutting surface. The analysis of any long range temporal phenomena is simplified by the continuous passage of virgin material across the cutting surface.

Variation of the contact characteristics was achieved by the familiar practice of varying tool geometry and surface speed. The high loads imposed are characteristic of a variety of related metal forming operations. In addition, the behaviour of planar surfaces under normal and obliquely loaded sliding contact has applications in the analysis of wear in very heavily loaded sliding systems.

Although these factors promote the use of orthogonal cutting, developments in the understanding of oblique cutting and shear flow around the tool nose allowed for a more realistic cutting geometry to be used in these tests.

1.11.3 Insert Tooling.

The commercial popularity of indexable insert tooling demonstrates the cost benefits achieved by the use of disposable inserts. Regrinding a worn or damaged cutting edge is more expensive than replacing a worn insert edge. With surface hardened tools a further cost benefit associated with insert tooling emerges. The wear resistance of a surface hardened tool is lost when the case is penetrated by wear. Although nitriding is an inexpensive process, the cost of collecting, regrinding, renitriding and redelivery of wrought tools is a further economic disadvantage of their use.

Because of these considerations,tests were undertaken using indexable insert tools.

1.12 Metal Cutting.

The theory underlying the behaviour of the tool and workpiece during metal cutting is discussed in chapter 2.

1.13 Wear

A number of wear mechanisms effect tool life [48].

(i) Formation of a built up edge.

(ii) Diffusion.

(iii) Attrition.

(iv) High temperature shear.

(v) Abrasion.

(vi) Sliding wear.

Beside mechanical wear leading to the failure of the tool, a purely thermal mechanism may be responsible for softening of the tool material to a point where catastrophic failure of the tool nose occurs.

This is described in section 5.3.2.

Seizure is the normal condition over at least part the tool/work interface in most industrial turning operations since protective oxide films are quickly removed and steel maybe friction welded at a surface speed of 16-50 m/min [40]. Movement of the chip over the tool is by intense shear in a thin (10 - 75μm) layer of work material which is responsible for the generation of heat. Thermal conduction causes heating and softening of the tool nose, and hence to deformation of the cutting edge. The clearance angle is eliminated and contact between the tool and freshly cut surface extends down the tool flank producing a new source of heat and leading to the collapse of the tool nose.

This mode of failure is typical of high speed steel tools, particularly during cutting at high surface speeds. The initial stages of softening are of critical interest. After minimal flank wear, the heat input into the toolnose is increased, causing further softening of the cutting edge, promoting flank wear, which leads to a corresponding increase in tool temperature. Clearly those conditions leading to the initial wear are of interest, and it is these which have been examined in this study.

1.13.1 Mechanical Wear

1.13.1.1 The formation of a built up edge (BUE).

The formation of a BUE is generally recognised [41] to result from repetitive strengthening of the first adhering work material layers by shear strain, leading to yield occurring in the less strained layers further from the tool surface. Although the continuous build up and loss of BUE leads to abrasive wear, a stable BUE protects the tool by assuming the function of the cutting edge, and may restrict contact between the recently cut work material and tool clearance face.

1.13.1.2 Diffusion Wear

For diffusion wear to occur the following conditions must be met.

(i) The two surfaces should be metallurgically bonded so that atoms may move from one material to the other.

(ii) Temperatures must be high enough to allow rapid diffusion.

(iii) The tool material must be appreciably soluble in the work material.

In the case of high speed steel tools the loss of chromium from the tool material can be particularly pronounced.

1.13.1.3 Attrition

Attrition wear is particularly important for precipitation hardened material as it involves the removal of microscopic particles from the tool surface, including microcrystalline hard precipitates by undermining the surrounding steel matrix. Such particles may become involved in three body abrasive wear.

1.13.1.4 High Temperature Shear

High temperature shear occurs at seizure and although the worn faces resemble those produced by diffusion wear the shear process is more rapid. It occurs when the tool temperature exceeds the design temperature, i.e. when the stress required to shear the highly strained work material is greater than that required to shear the less - strained tool material. This wear mechanism is associated with the loss of the built up edge.

1.13.1.5 Abrasion

Abrasion may be divided into two and three body processes. Although both contribute to tool wear, the effect of the two body process is more important in metal cutting. Hard particles in the work material range from carbide inclusions to aluminium oxide particles in steels deoxidised using aluminium. These adversely affect the condition of the tool not only directly, by abrading the surface, but also indirectly by producing, as a result of this abrasion, a tool surface more prone to seizure.

Silica and silicates present in the workpiece are also responsible for a certain amount of wear by the abrasion mechanism. Hard precipitate microcrystals detached from the tool by attrition wear will also contribute to abrasive wear.

1.13.1.6 Sliding Wear

Sliding wear occurs at the position where the surface of the bar crosses the cutting edge of the tool. The resulting surface is extemely smooth by comparison with those produced by the mechanisms above [48].

1.13.2 Measurement of Wear

Many different techniques have been proposed for measuring tool wear. A number of these warrant discussion.

(i) Correlation with machined surface roughness.

(ii) Measurement of crater and flank wear.

(iii) Machining ratio.

(iv) Acoustic emission.

(v) Correlation with frictional force and coefficient.

1.13.2.1 Surface Roughness

Although machined surface roughness has been shown to vary with cutting conditions [41] and to a certain extent with tool wear [42] other workers report that the mechanisms responible for the surface finish are largely independent of the state of the worn tool [43]. In their opinion asperities generated at the tool nose by shear of work material and loss of the built up edge are modified by contact with the flank face of the tool.

1.13.2.2 Crater and Flank Wear.

Various techniques have been developed to assess crater and flank wear. Replica moulds with quick setting plastics are a non-destructive technique for studying crater wear profiles. The information from a series of spaced profiles read with a stylus profilometer, digitised for computer manipulation, gives a more complete description of the wear than may be obtained by measuring the three dimensions of the wear scar.

1.13.2.3 Machining Ratio.

Machining ratio (MR) is the ratio of tool material removed to work material removed [44].

$$MR = \frac{V.d.f.t}{V.w} = \frac{V.d.f.t.\rho}{W}$$

where V = cutting speed

d = depth of cut

f = feed

t = cutting time

ρ = tool material density

w = volume of tool wear

W = weight of tool wear

Rao and Lal [45] using an approximate method for calculating crater wear scar volume [46], found that machining ratio increases with cutting time and is at a maximum at the point of inflection on the flank wear growth curve.

1.13.2.4 Acoustic Emission

Acoustic emission at frequencies above the audible range and below 350 KHz have been studied as a source of data in tool wear. The power spectrum was found to increase during initial wear and to reach a saturation value which increased with cutting speed. The count rate of acoustic emissions was found to to increase with flank wear above a critical value [77].

1.13.2.5 Frictional Force

The frictional force on the tool and frictional coefficient between the tool and workpiece have also been studied as a function of wear [47]. These were found to decrease initially with increasing wear to a minimum value corresponding to critical wear, at which point the tool would normally be replaced. As the wear increased past this point however, a corresponding increase in frictional coefficient and force was observed.

Reduction of frictional force is an important factor in optimising tool performance. Not only are the critical conditions for seizure made more severe, but also decreasing the frictional force will lead to a greater proportion of shear occurring in the bulk of the chip, from which position less heat is able to flow into the tool itself.

1.14 Tool Temperature.

Cutting temperatures may be used to provide information in two broad fields.

(i) As an indication of wear on an individual tool.

(ii) To provide information concerning chip / tool contact.

A number of techniques for measuring tool temperature have been explored, including tool material phase transformations, implanted thermocouples, measurement of tool / workpiece potentials, and photodensitometric measurements of infra red images. These have been reviewed by Shaw [61].

1.15 Choice Of Experimental Techniques.

The variety of wear parameters available reflects the different approaches to tool wear. In assessing tool life in precision turning operations, a flank wear parameter would be studied. However, the failure of a H.S.S tool involved in the roughing stages of a machining process would best be predicted by a study of crater wear. In the development of a novel surface coating, frictional behaviour during cutting would yield useful data. In this study the following parameters were used:-

(i) Studies of frictional behaviour.

(ii) Tool temperature measurements.

Studies of frictional behaviour were carried out using data from dynamometry. In electing to perform these investigations it was assumed that the nitrided surface would exhibit modified frictional behaviour.

Cutting temperature was a particularly attractive parameter to measure for a number of reasons.

(i) Considerable literature is available on the subject with a number of reliable techniques already developed.

(ii) Finite element software was available, with which the system could be modelled.

(iii) Correlation of cutting temperatures and cutting force

measurements would provide a rich source of information concerning cutting conditions.

(iv) A technique, in this case implanted thermocouples, could be developed with the limited resources available.

The methods used in assessing cutting temperature and frictional behaviour are detailed in the chapter on experimental techniques.

Ideally, for a simple treatment of results, metal cutting would have been performed using tubular workpieces, to avoid corner effects and complications in modelling shear and chip dynamics. However, in order to simulate common machining practice, and maintain the industrial relevance of the work, bar cutting was performed, and the necessary adjustments and approximations made to demonstrate the benefits of cutting with nitrided tools in terms of conventional theory.

Chapter 2. Metal Cutting Theory.

2.1 Introduction.

A great deal has been written concerning the theory of metal cutting. An understanding of the mechanisms by which metal is removed during cutting is essential for the design of machining operations and for the prediction of tool performance and wear. In order to understand the effects that surface treatments such as nitriding might have on metal cutting processes, such as single point turning, certain key theoretical aspects should be understood. This section examines some of the theory relevant to the interpretation of experimental results obtained in this study.

2.2 Metal Cutting Geometry.

Figure 2.1 illustrates the geometry of orthogonal metal cutting. The rake face of the tool is inclined at an angle, α, the rake angle, to a perpendicular to the local workpiece motion, shown negative by convention in figure 2.1. The clearance angle, β, separates the tool clearance face from the recently cut work material. The work material is removed by shear in the plane of maximum shear stress, which lies at an angle, ϕ, the shear angle, to the local workpiece motion.

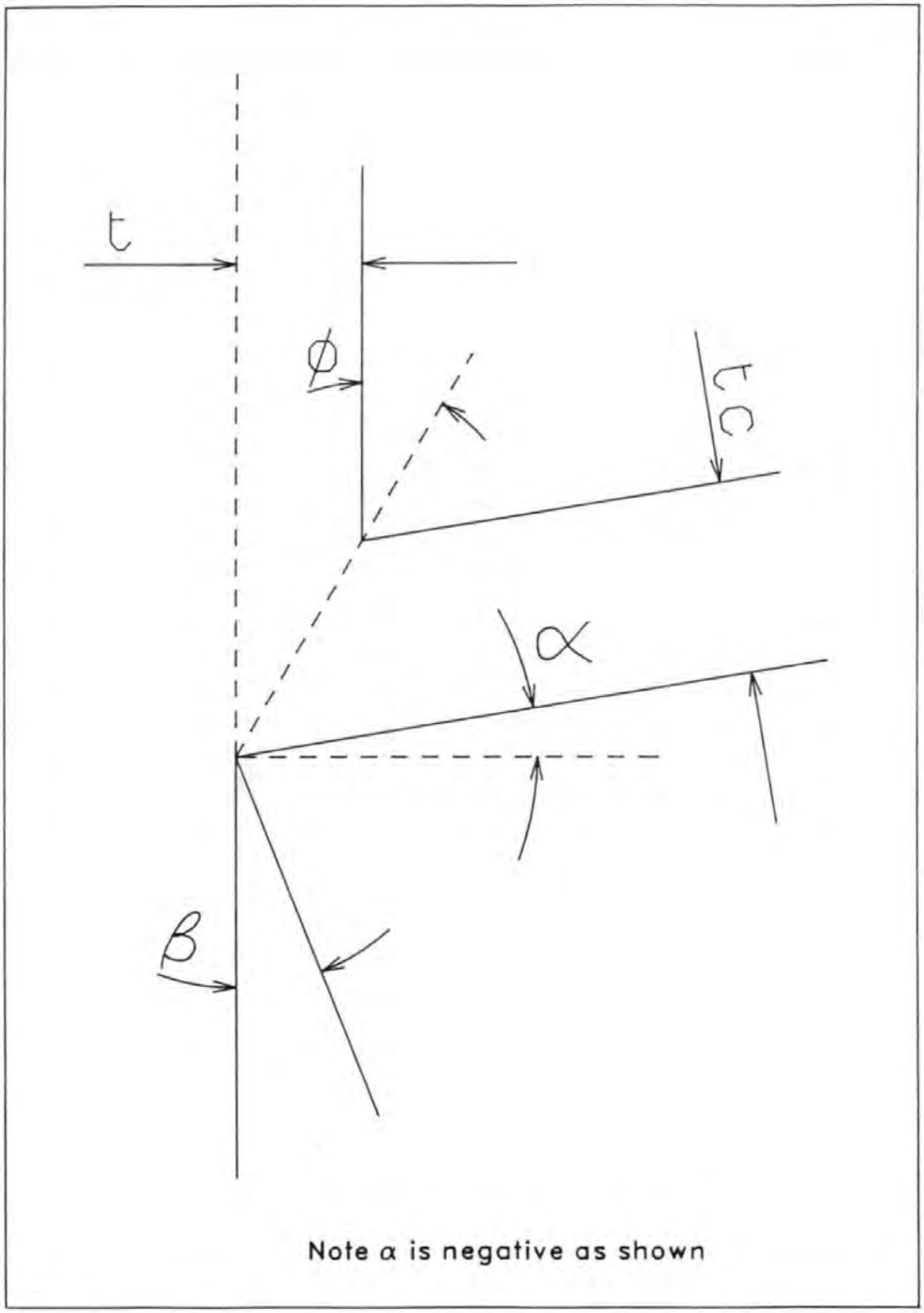

Figure 2.1 The Geometry of Orthogonal Metal Cutting.

2.3 Chip Formation.

Investigations of chip forms provide information concerning the geometry of the chip forming mechanism. The chip thickness ratio, rc, may be obtained using equation 2.1, and applied to obtain a value for shear angle using equation 2.2. In practice an accurate value for ϕ must be obtained from the cross sectional areas of the pre - shear and post - shear chip, since over a broad range of feeds and depths of cut a considerable change in chip cross section occurs during shear.

$$rc = \frac{t}{tc} = \frac{lc}{l} \qquad \text{eq. 2.1}$$

$$\tan\phi = \frac{rc.\cos\alpha}{1 - rc.\sin\alpha} \qquad \text{eq. 2.2}$$

where l = undeformed chip length

lc = chip length

In the tests undertaken as part of this study, chip geometry was further complicated by the use of non - orthogonal cutting conditions. Segmented features along the side of the chip caused cross sectional variations. For this reason, chip mass per length was found to be the most convenient criterion from which to determine the bulk primary shear angle.

2.4 Cutting Forces.

For a sharp tool with adequate clearance, friction on the clearance faces can be neglected [48]. To a first approximation, normal pressure and frictional shear stress are uniformly distributed over the chip / tool contact area (see section 2.5). Mean frictional shear stress and normal pressure are found by dividing force by apparent contact area between the two bodies. The apparent mean coefficient of friction, μ , is calculated experimentally from

$$\mu = \tan \Psi = \frac{Ff}{Fn}$$

The interdependence of primary and secondary shear forces is demonstrated in terms of an expression for primary shear angle in section 2.9.2.1. Most expressions for primary shear angle (section 2.9.2) also refer to the frictional coefficient in the secondary deformation zone.

2.4.1 Force Distribution.

In both the primary and secondary shear zones, a shear force, Fs, acts on the material in the presence of a considerable normal hydrostatic force. In the orthogonal case plane strain in the material leads to the propagation of a shear plane if

the critical shear stress of the material is reached. In a ductile material, the flow stress and shear flow stress may be assumed independent of hydrostatic force [48].

Primary shear angle is reduced by the effect of frictional force acting to inhibit chip flow across the rake face of the tool.

A method for the estimation of primary shear force from force and primary shear angle measurements was developed during this study and is set out below. Two assumptions have been made: that the force required to overcome flank face friction is negligible, and that primary shear angle is constant across the cut.

This second assumption has a particular importance for turning operations using a tool with a nose radius, around which some variation in underformed chip thickness occurs.

Consider a simple orthogonal metal cutting operation using a tool with zero side and end rake angles. The applied force, Ft, contains two components.
The first, Fts, overcomes primary shear stress.
In order to determine this component, an imaginary case is considered in which the frictional coefficient between the chip and tool is zero.

From figure 2.2,

$$\frac{vb}{vs} = \cos\phi$$

From conservation of work done (per second)

$$Fts.vb = Fs.vs$$

Then

$$Fts = \frac{Fs.vs}{vb} = \frac{Fs}{\cos\phi}$$

The second component of normal force, Ftf, overcomes secondary shear stress i.e. the frictional force between the tool and chip. In order to evaluate this component, a case is considered in which the primary shear force is zero.

From figure 2.3,

$$\frac{va}{vb} = \tan\phi$$

From conservation of work done per second,

$$Ftf.vb = Ff.va$$

Then

$$Ftf = \frac{Ff.va}{vb} = Ff.\tan\phi$$

For a perfectly sharp tool with adequate clearance, the measured normal force is the sum of these two components.

$$Ft = Fts + Ftf$$

$$Ft = \frac{Fs}{\cos\phi} + Ff.\tan\phi$$

Thus $Fs = Ft.\cos\phi - Ff.\sin\phi$

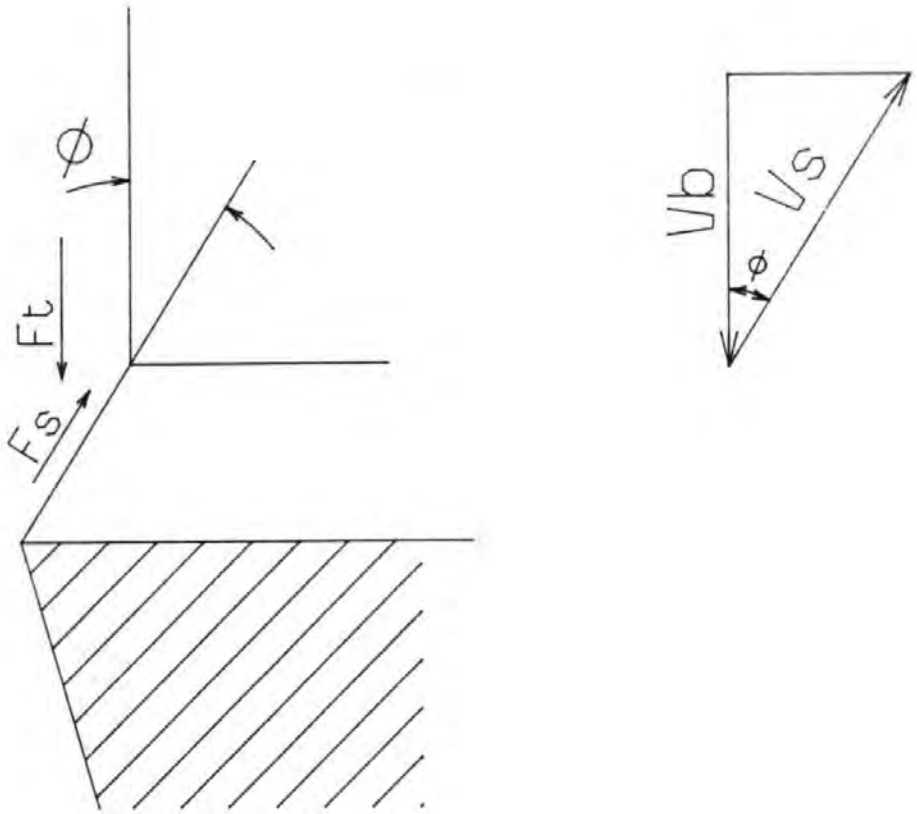

Figure 2.2 Shear Force and Primary Shear Velocity.

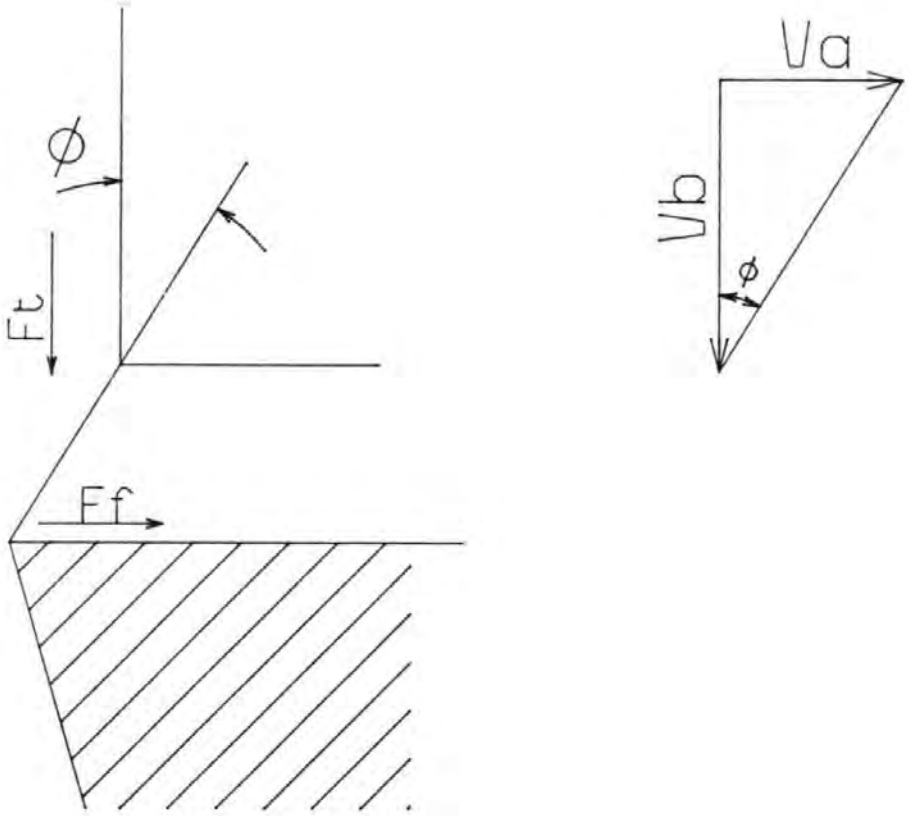

Figure 2.3 Frictional Force and Chip Velocity.

The non zero rake angle case is considered in appendix (1).

2.5 Stress Distribution.

When the average frictional stress in the chip tool contact zone, τ_s , is greater than the shear flow stress, k, of the work material, the energy required to cause shear in the chip is less than that required to overcome the frictional force at the tool/chip interface. Under such conditions sticking friction is said to occur, and although the relative motion of the tool and chip at their interface is arrested, there is not necessarily any sticking at this junction.

The model of stress distribution attributed to Zorev [49], (figure 2.4) describes chip / tool interaction in terms of a critical normal stress acting on the tool rake face. As this value is exceeded, sliding friction is superseded by localised seizure at the chip / tool interface and shear in the overlying layers of work material. The zone of sliding friction may extend to most of the contact zone for materials with low adhesion, for example lead tin alloy. However, with materials of higher adhesion such as copper and aluminium, the shear stress is no longer able to rise once the shear flow stress of the material in the sticking zone has been exceeded.

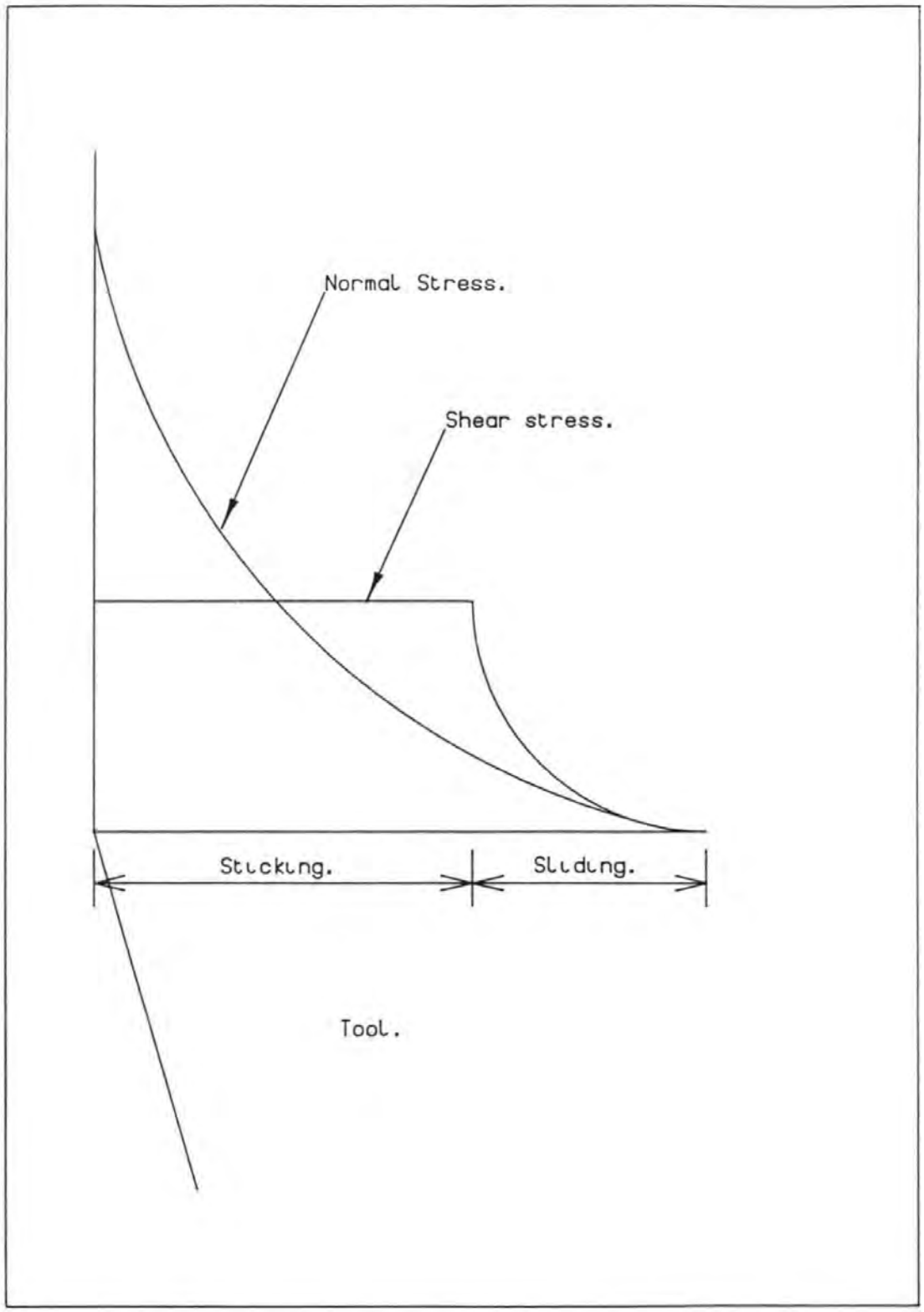

Figure 2.4 Stress Distribution In Orthogonal Metal Cutting.

Normal stress on the tool rake face varies as a function of shear plane length and chip tool contact area. The trend towards lower normal stress at higher feedrates reported by other workers (section 2.9.4) was also a feature of experimental results from this study.

Less is known about the stress distribution in the shear zone. It has been proposed [52] that shear stress should reach a limiting value, equal to the shear flow stress of the undeformed material, at some distance from the surface.

The stress distribution on the rake face has been studied experimentally, but photoelastic studies of metal cutting are limited as photoelastic polymer deforms in a nonrepresentative manner.

Stress distributions have been studied using tools with a split rake face, over part of which stress is measured using a dynamometer. Although the rake face of a segmented tool is discontinuous the cutting conditions during its use remain relatively realistic. The stress distribution proposed by Zorev has been widely supported by such experimental work. Normal stress has been found to rise from zero at the point of tool/chip separation reaching a maximum at the tool edge. Shear stress rises similarly, although more recent studies [50,51] indicate a plateau near to the cutting edge, and a

decline before this point in the presence of a built up edge.

Two factors complicate the use of this data to describe the variation in normal stress with undeformed chip thickness around the toolnose radius. The first is the uncertainty in predicting the extent of reduction in normal stress due to edge effects (see section 2.6.2). The second is that little information describing the variation in chip behaviour (chip curl etc) around the toolnose is available.

In cutting using a tool with a large nose radius the stress distribution must be measured both along the length of the chip tool contact and around the toolnose. For these reasons a detailed study of the normal stress distribution was found to be outside the scope of the present work.

2.6 Material Flow.

It is important to observe material flow at realistic cutting speeds. Flow at the chip edge is not representative of mid-chip flow,and so studies have been carried out using high speed photography through a glass plate ensuring plane strain up to the chip edge [53]. More frequently quick stop techniques have been used to examine chip flow.A gridded parting plane [54,55] has revealed further information. The structural features of the chip have been investigated,

although mechanical shock associated with deceleration may effect the final phase of chip formation.

Clearly the flow of material during metal cutting is chiefly governed by

(i) frictional conditions

(ii) materials properties.

(iii) tool geometry.

The strain distribution in the work material is a function of local changes in flow stress and friction, and is affected by

(i) Strain hardening

(ii) Strain rate sensitivity

(iii) Temperature distribution

(iv) Adhesion between tool and chip

A method for determining chip flow angle from tool geometry is outlined in section 2.10

In order to understand chip formation fully, bulk chip flow and edge effects are best considered separately.

2.6.1 Bulk Chip Flow.

The angle included between the radial direction and the direction of bulk chip flow in the rake face plane is known as the chip flow angle, δ. It may be determined experimentally by photography of the tool rake face or from measured components

of frictional force (see section 3.6).

Normal force on the rake face is a function of the shear plane length, and has higher values for greater local undeformed chip thickness. For a tool with a nose radius, undeformed chip thickness varies around the engaged cutting edge. However, normal stress on the chip / tool contact is relatively uniform around the toolnose, as chip / tool contact area increases with undeformed chip thickness and normal force (see section 2.4).

Prediction of the chip flow angle is discussed in section 2.10.

2.6.2 Edge Effects.

In order to understand cutting forces measured experimentally, it is necessary to consider realistic cutting, in which primary shear may not occur uniformly over the whole engaged cutting edge. In addition to variation in shear plane length around the nose of a tool, the shear mechanism is further complicated by conditions prevailing towards the outside edge of the work material.

For ideal orthogonal cutting, during which no edge effect shear occurs, a single primary shear plane extends over the full width of the cut. In practice, there is a zone towards the outside edge of the cut in which the compressive stress acting

on the chip is more easily relieved by deformation towards the outside edge of the cut. Material from this outside edge forms the segmented features present on the outside edge of the chip (see section 2.10.2.1).

2.7 Deformation Zones.

Two regions of intense shear are commonly identified in the work material around the tool nose. Primary shear occurs in the region marked (1) in figure 2.5. The thickness of this zone is reduced to a few micrometers by shear heating, and it is often thought of as a plane. Frictional force in the secondary zone, marked (2), is typically sufficient to cause plastic deformation across the thickness of the chip. Some deformation occurs in zone (3), as relaxation from elastic deformation in the work material brings it into contact with the tool flank face. The extent of plastic deformation in zone (4) is a function of the mechanical properties of the workpiece. Material in zone (5) may experience some strain hardening.

2.8 Chip Tool Interaction.

The chip tool contact is divided into a sticking and a sliding zone. Transition from sticking to sliding is thought to occur at the point at which the resultant of the frictional and

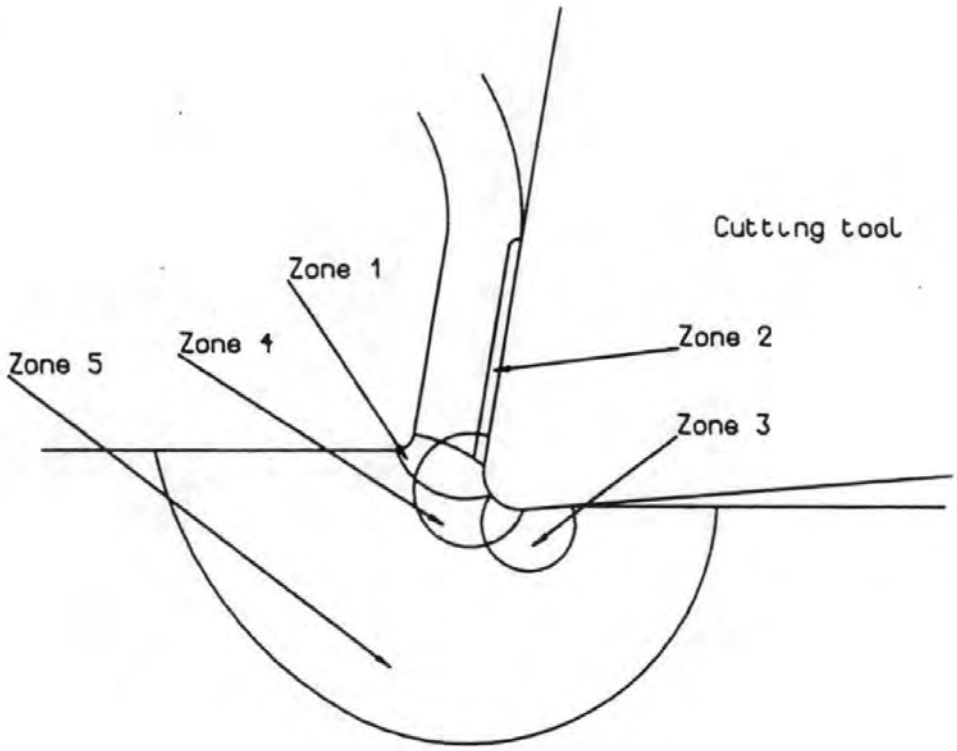

Figure 2.5 Work Material Deformation Zones.

normal force vectors, projected from the free end of the primary shear plane, intersects the tool rake face [56]. See figure 2.6.

2.8.1 Sliding Friction.

Sliding friction is found when $\mu p < k$ [48]. The value of p is usually greater than the value of k and so the coefficient of friction must be reduced if sliding is to occur. However, the introduction of lubricants between the chip and rake face is very difficult to achieve. Sliding may be maintained on precoated surface films for a limited time only. Furthermore, adhesion and lubricant breakdown are accelerated at elevated temperature so cutting speeds must be low.

However, the range of cutting conditions under which sliding occurs may be extended by the correct choice of tool coating, work material and the use of modified tool geometry. Sliding friction is more easily maintained with a large positive rake angle which reduces the length of the shear plane and normal force [48].

2.8.2 Sticking Friction.

In practice most metal cutting occurs under conditions of sticking friction.Sliding friction cannot be maintained for a

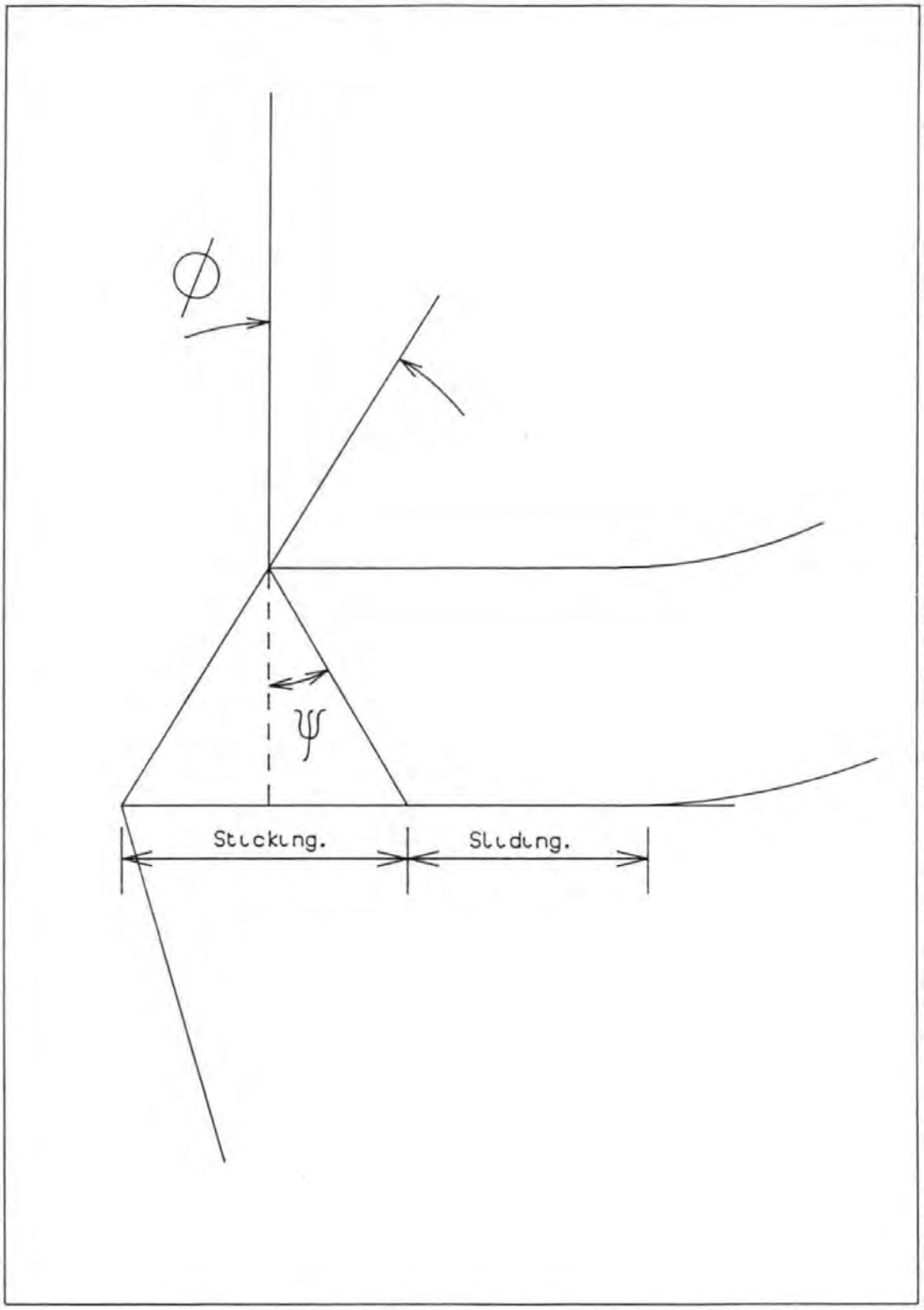

Figure 2.6 Transition From Sticking To Sliding In The Chip Tool Contact Zone.

number of reasons.

(i) Sustained contact leads to poor lubricant access and innert surface films are quickly worn off.

(ii) The continuous generation of a new surface represents ideal conditions for adhesion.

(iii) Large positive rake angles produce fragile tools. For high speed steel a positive rake angle of 5 - 10 degrees may be acceptable. However cemented carbides require zero or negative rake.

2.9 Effects Of Process Geometry.

2.9.1 Rake Angle.

In order to reduce cutting forces, a positive rake angle may be used. Large positive rake angles are prohibited by poor mechanical strength and heat transfer. Since the normal force acting on the rake face varies as a function of rake angle the effect of diffusion wear processes is less pronounced under such conditions. Positive rake angle causes the chip to thin by increasing the primary shear angle. A corresponding reduction in normal pressure in observed, which may lead to a reduction in observed frictional coefficient [48].

Small negative rake angles confer stability to the built up edge, and for cutting tool materials such as carbides, the

effect of increased cutting forces is offset by the separation of secondary shear from the tool surface. At larger negative rake angles cutting gives way to bulge formation and the direction of chip flow and frictional force are reversed.

2.9.1.1 Effective Rake Angle.

The effective rake angle, α', must be determined. For an orthogonal tool, rake angle is thought of as that angle included between a normal to the cutting edge lying in the rake face plane and the x - y plane (figure 2.7). When considering cutting around a nose radius, this method for determining effective rake angle implies some variation around the toolnose (figure 2.8) however, during metal cutting, the entire chip flows at one angle, the chip flow angle, γ, rather than perpendicular to the local cutting edge. The effective rake angle is constant around the entire toolnose, with a value given by

$$\sin\alpha' = \sin\alpha . \sin\gamma' \qquad \text{eq. 2.3}$$

Where γ' is the chip flow angle determined in the rake plane (figure 2.9).

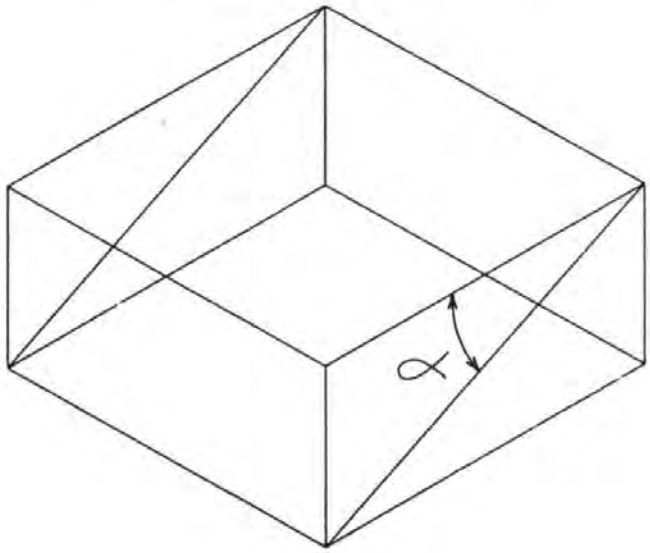

Figure 2.7

Definition Of Rake Angle In Orthogonal Cutting.

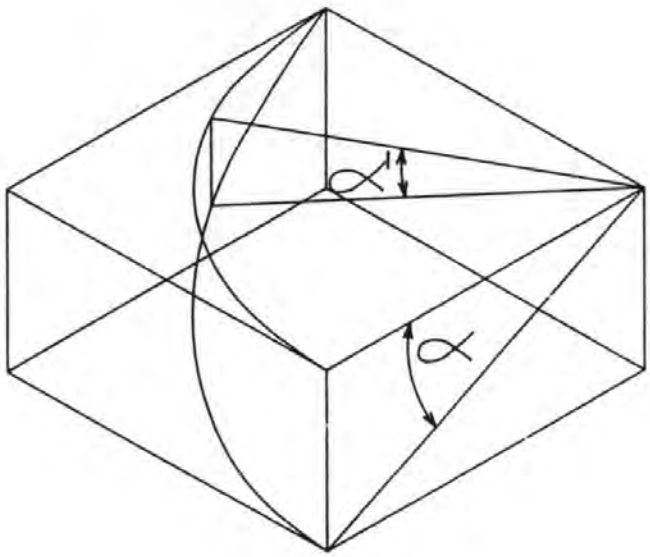

Figure 2.8

Variation In Rake Angle Around The Toolnose.

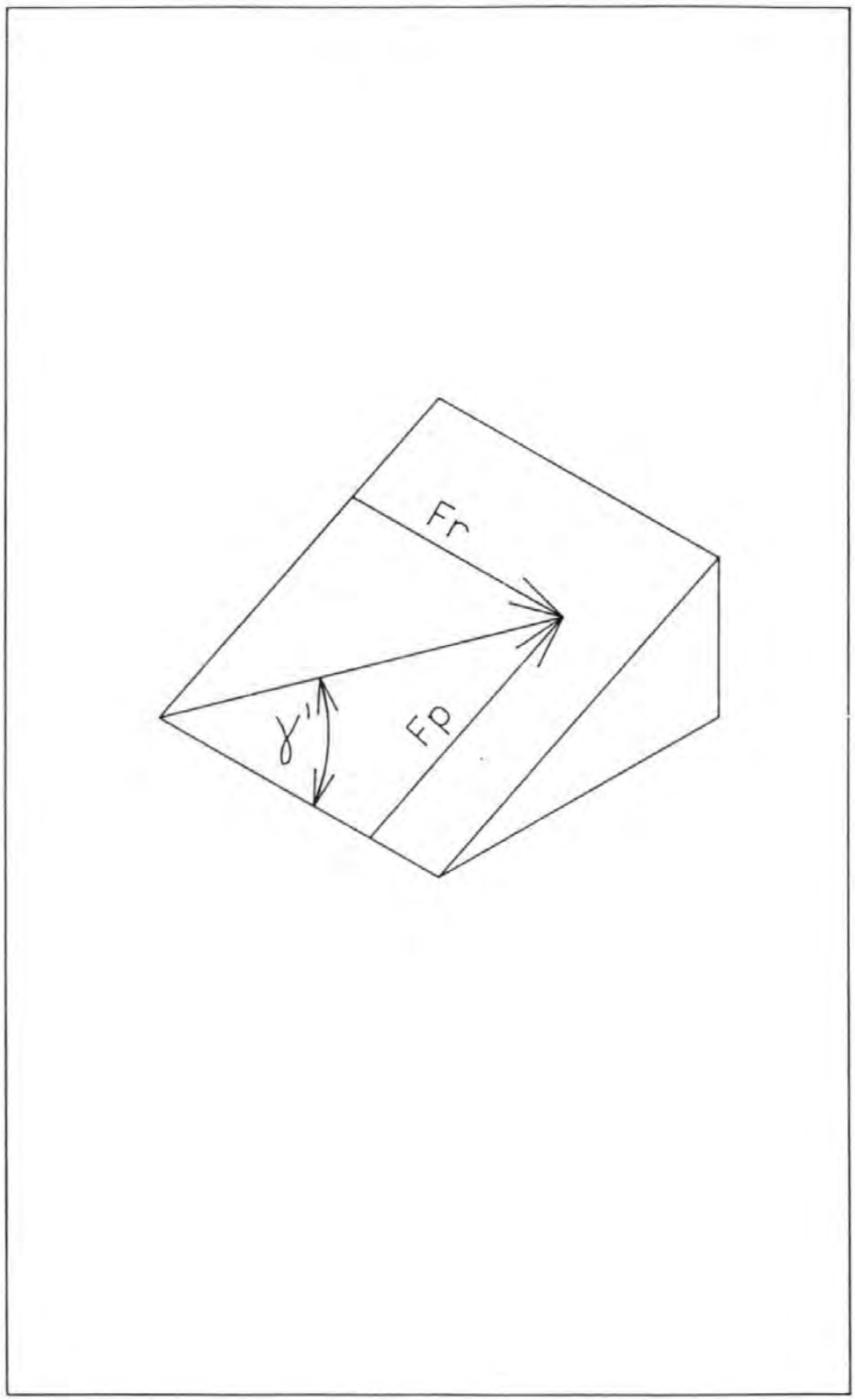

Figure 2.9 Determination Of γ', The Chip Flow Angle In The Rake Face Plane.

2.9.2 Shear Angle.

A number of expressions have been proposed by which shear angle during metal cutting may be predicted.

Metal deformation is often assumed to occur by the least energetic flow pattern. Theories based on maximum shear stress [59] or minimum shear energy [60] lead to relationships of the form

$$\phi = \frac{\pi}{4} - \frac{1}{2}(\psi - \alpha)$$

For frictionless cutting the shear angle should be half the angle between the rake face and the cutting direction. In practice it is found that $\pi/4$ is too large a constant. Models based on an analysis of a single cutting parameter generally fail to satisfy experimental data fully. In surveying attempts to predict shear angle, Shaw [61] suggests that an equation of the form

$$\phi = \frac{\pi}{4} - \beta + \alpha + C(1) + C(2) + C(3) + \text{etc}$$

should be used, where:-

β = friction angle

C(1) = rake angle compensation to account for the presence of a built up edge.

C(2) = rake angle compensation for the size of the secondary shear zone.

C(3) = compensation for chip / tool contact length.

C(4) = compensation for rounding of the cutting edge due to wear.

C(5) = compensation for interaction between the primary shear zone and the tool rake face.

C(6) = compensation for strain hardening during chip formation.

It is his assertion that such an expression is of little general use in determining shear angle because it contains so many variable quantities, and only serves to demonstrate that a simple expression for shear angle is unlikely to be found. In addition, the conditions prevailing across the engaged cutting edge of a tool with a large nose radius may not be uniform. For a tool with a nose radius, changes in stick / slip character of the chip tool interface will accompany the variation in undeformed chip thickness across the engaged cutting edge. This will lead to some variation in primary shear angle across the primary shear zone.

2.9.2.1 An Expression For Primary Shear Angle.

A method for evaluating primary shear angle from experimentally determined cutting forces was developed by the author as an estension of two other topics. In section (2.4.1) an expression for primary shear force was derived. For the zero rake angle case,

$$Fs = Ft.\cos\phi - Ff.\sin\phi$$

The derivation of primary shear plane areas in appendix (2) from the minimum global pathlength model developed in section (2.10) yields useful data for the evaluation of primary shear force as the product of critical shear stress and primary shear plane area.

$$Fs = \frac{\tau s.I}{\sin\phi}$$

Where I is the integral of local undeformed chip thickness over engaged cutting edge length and $I/\sin\phi$ gives an approximate value for primary shear plane area (see appendix 2).

Although the minimum global pathlength method yields only approximate values for primary shear plane area, the errors introduced are found to be acceptably small (see appendix 2).

(For the orthogonal case, if edge effects (section 2.6.2) are ignored, the undeformed chip cross section may be substituted for I).

Both of these expressions contain primary shear angle as the only unknown, and this may be determined as the value yielding equivalent solutions for primary shear force in the two equations.

Substituting $1 - \sin^2 \phi$ for $\cos^2 \phi$, squaring and re-arranging leads to the expression

$$(Ft^2 + Ff^2).\sin^4 \phi + (2\tau s.I.Ff - Ft^2).\sin^2 \phi + \tau s.I^2 = 0$$

The quadratic has two solutions for $\sin\phi$, each of which yields one acute and one obtuse value for primary shear angle. The obtuse angles are rejected, leaving two possible values, typically around 20 and 40 degrees. From studies of chip microstructure it is clear that the lower value is adopted. However, it is the higher value that minimises primary shear plane area, and it seems likely that the lower value is preferred due to the associated reduction in chip velocity and work done in secondary shear.

2.9.3 Flank Face Contact.

Contact during cutting a rigid plastic material with a perfectly sharp tool is limited to the rake face. In reality the workpiece deforms elastically and springs back to create a small wear land on the flank face. Flank face wear has been studied using tools with artificial wear lands [62]. The presence of a built up edge reduces flank face contact, but it's inherent instability leads to poor dimensional tolerance of the machined component. Having a positive clearance, the flank face is more easily lubricated than the rake. The importance of positive clearance has been demonstrated. Negative clearance as low as 1 degree leads to loss of relief and extrusion of the work material [63].

2.9.4 Size Effects.

The fact that thinner cuts require proportionately more energy has been studied by a number of authors [64,65,66]. Experimental data may be expressed in an empirical form:

$$E = E\ (t/t\ ref)^{-c}$$

where E = energy consumed per unit volume of work material removed

t ref = some convenient value (eg 1mm)

c = a value between 0.1 and 0.5 [67]

The effect of size may also be considered in terms of the transition from rubbing to cutting.

(i) Contact with asperities represents sliding contact between two rough surfaces.

(ii) Superficial ironing by a tool with a large positive rake angle.

(iii) Bulge formation without metal removal.

(iv) When undeformed chip thickness becomes greater than the cutting edge radius the effective rake angle becomes zero at the surface and normal cutting is established.

Where very little or no metal is removed flank face contact accounts for proportionately more of the energy consumed.

2.9.5 Effect Of Edge Radius.

The best sharp tool has a corner radius of around 0.3 μm and this is quickly blunted, leading to an increased cutting edge

radius with increased frictional contact and altered cutting performance. At the edge of a tool with a large cutting edge radius the effective rake and clearance are negative, and only away from the cutting edge does clearance become positive. This promotes the occurrence of a built up edge (BUE), although with a relatively sharp tool the built up edge may be stable and improve the surface finish [66,68]. In nitrided tools through hardening along the cutting edge may exaggerate this effect. A stable built up edge may occur with hard (tungsten carbide or harder) tool materials.

A study of the stability of the BUE was performed by Hoshi [69], and lead to the development of the silver white chip (SWC) tool geometry. A chamferred cutting edge stabilised the BUE and caused it to flow out continuously along the principal cutting edge as a secondary chip. The result of the lower cutting forces recorded using this technique and the removal of the heat by the secondary chip was an increase in tool life of around twenty per cent.

2.10 Effect of Nose Radius.

2.10.1 Introduction.

The modification of cutting tool geometry by wear is reduced when using tools with a large nose radius. Flank wear which would blunt the point nose of a tool causes less damage to the

profile of a large nose radius across which the wear is distributed. The use of such tools has been popularised by the availability of powder formed inserts with a range of standard tool nose geometries. The development of a model of the shear occurring during cutting is of considerable interest, representing the first stage in the development of a method for predicting wear.

The models set out below were developed to predict chip flow angle from cutting geometry, described in terms of :

Nose radius.

Depth of cut.

Feedrate.

Single values of depth of cut (= 1.0 mm) and nose radius (= 0.8 mm) and a range of feedrates (= 0.2, 0.4, 0.6, 0.8, 1.0, 1.2 mm/rev.) were modelled. The effect of rake angle was not considered. The output from the models is a predicted value for chip flow angle for a particular cutting geometry.

Two models, based on minimum local and minimum global pathlengths, have been developed by the author. The minimum local pathlength (MLP) model was found to be unreliable, being based on an inaccurate description of the physical system. The minimum global pathlength (MGP) model was found to be better, although a number of refinements must yet be made in order to extend the range of cutting conditions over which it may be

applied.

A rudimentary description of the basic operation of the models is presented below as an introduction to the more detailed description presented in the following sections.

In the minimum local pathlength (MLP) model, local chip flow angle at any position along the nose radius must first be established. Stabler [70] proposed that, for a tool with zero rake angle, chip flow should occur perpendicular to the local cutting edge. However, in the MLP model, local chip flow was assumed to occur at an angle such that the local pathlength was minimised.

The toolnose is then divided into elements, dS, figure 2.10, within which the flow angle is determined using which ever local chip flow criterion was adopted. Young et al [71] proposed that, for zero rake angles, the frictional force per unit undeformed chip thickness along a unit length of cutting edge is constant. From this constant, denoted frictional force intensity, a value for the friction force acting on the chip element is derived. The resultant frictional force and flow angle for the entire chip are determined by summing elemental frictional forces and cartesian frictional force components.

The second model, developed by the author, is the minimum

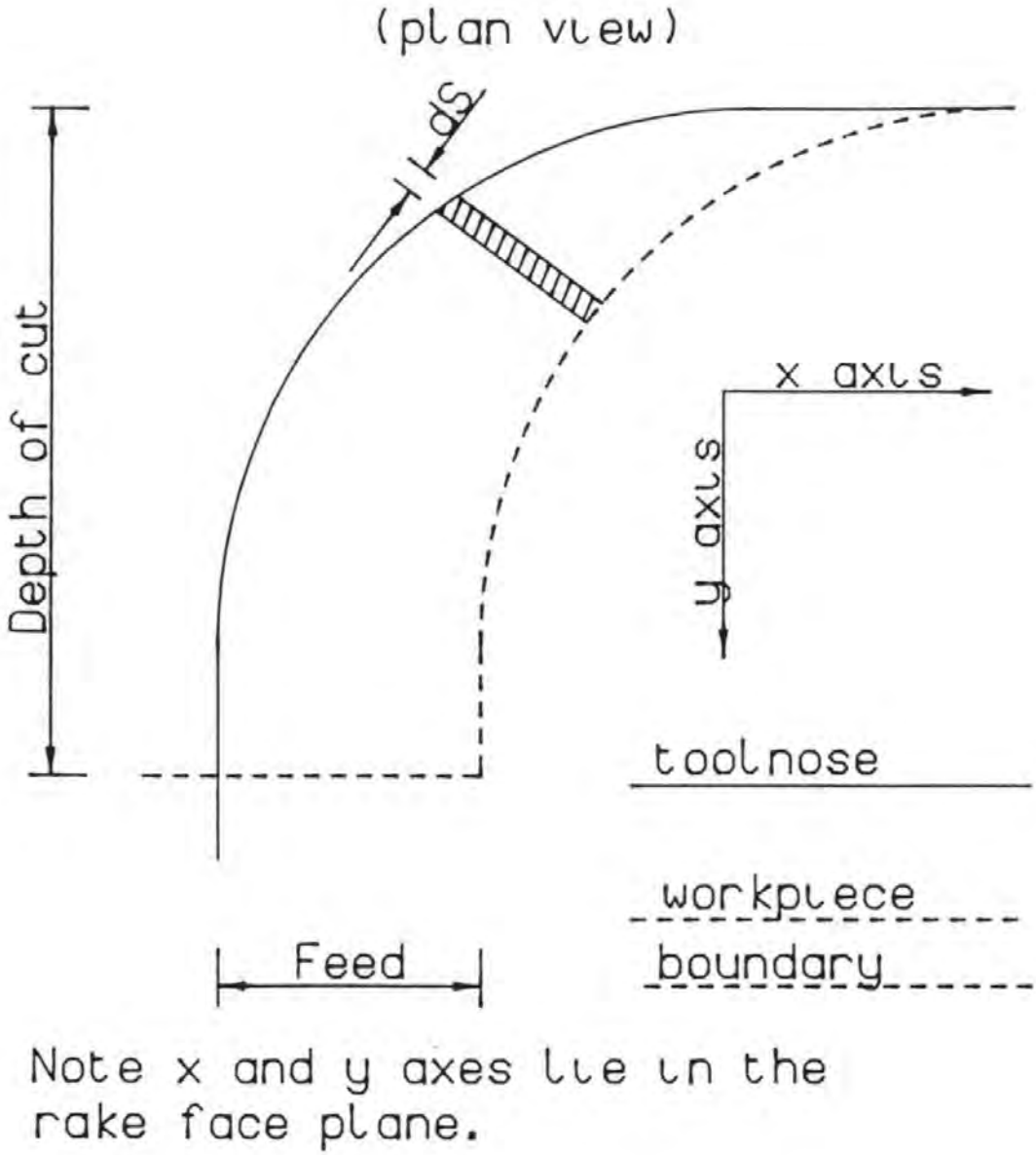

Figure 2.10 The Geometry of The Minimum

Local Pathlength Model.

global pathlength (MGP) model. In this case all friction force vectors have the same direction, i.e. all of the chip flows at an angle, γ. The total resultant frictional force is taken to be proportional to the primary shear plane area, which is found to vary with chip flow angle. The chip is assumed to flow at an angle such that the primary shear plane area and resultant frictional force are minimised.

2.10.2 The Minimum Local Pathlength Model.

The following assumptions were made in developing the minimum local pathlength model. In order to simplify the geometry of the problem, both side cutting edge angle and end cutting angle (figure 2.11) were assumed to be zero, a close approximation to the experimental values of two degrees. Local chip flow angle was assumed to be such that material at A in figure 2.12 traversed the minimum pathlength (AB) between the cutting edge and the workpiece boundary. This is somewhat contrary to Stabler [70], who asserted that, for zero rake angles, chip flow should be perpendicular to the local cutting edge.

2.10.2.1 Minor Chip Formation.

The behaviour of material close to the outside edge of the cut was considered. There exists a region of material, hatched in figure 2.13, within which the compressive stress is more easily

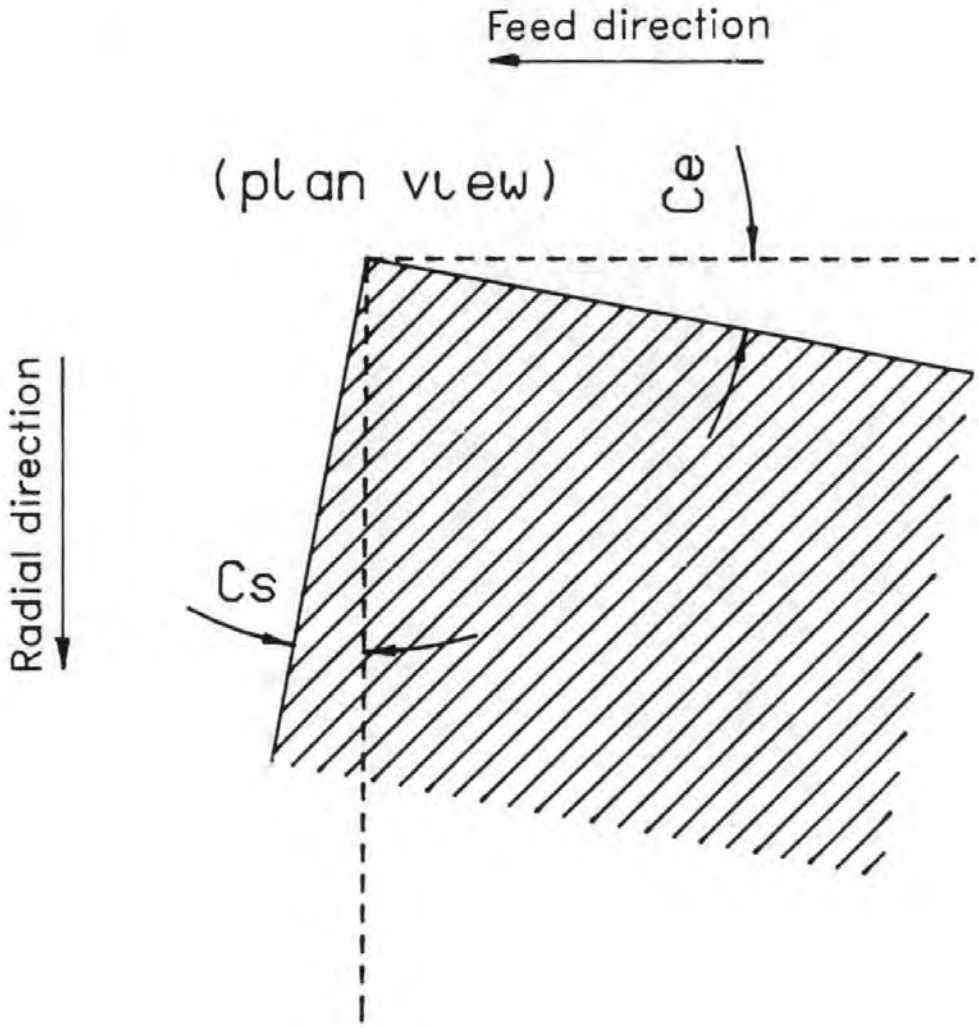

Figure 2.11 Cutting Edge Angles.

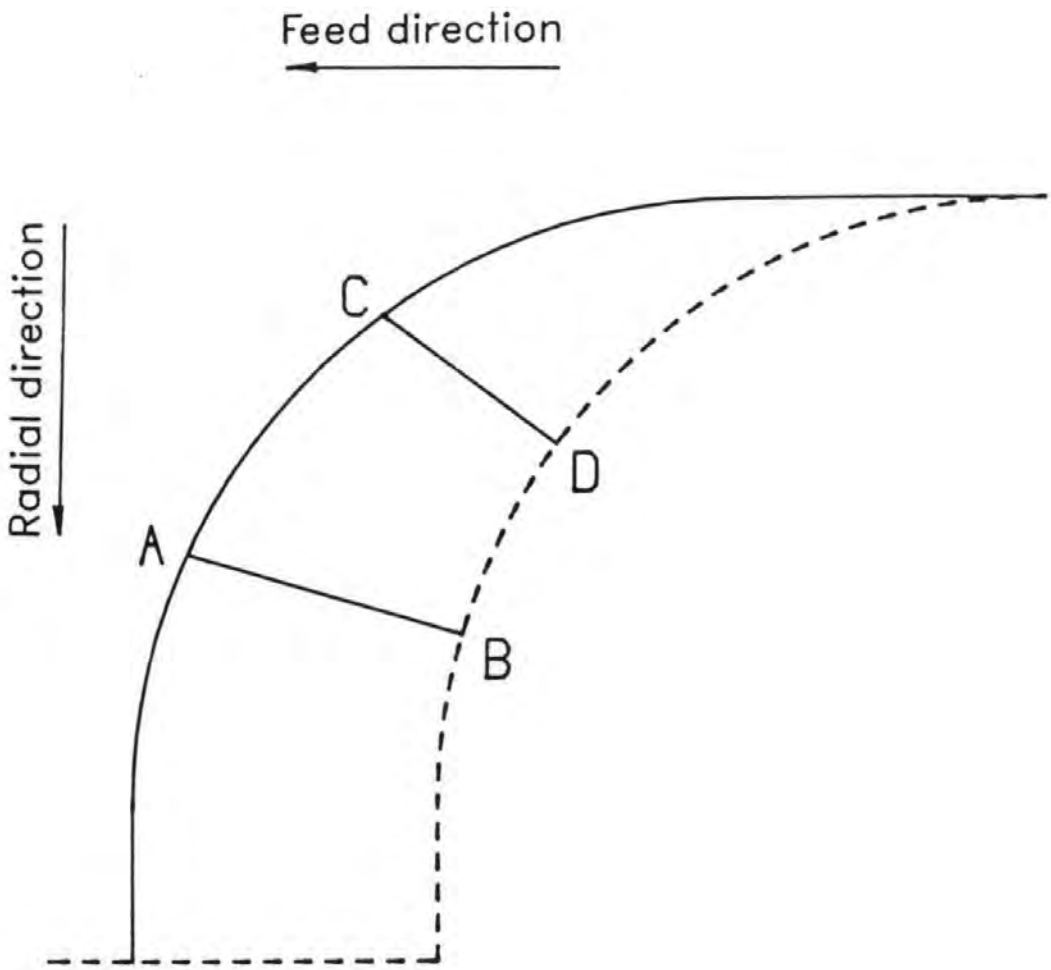

Figure 2.12 Minimum Local Pathlengths.

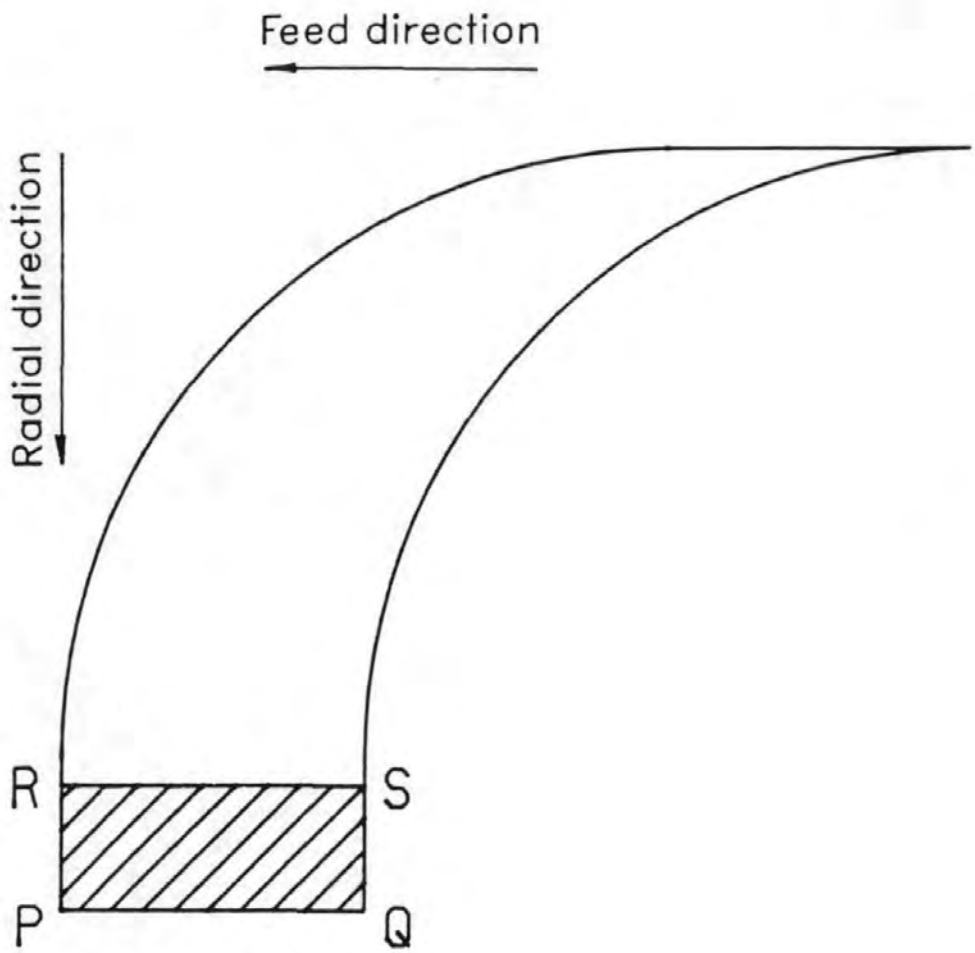

Figure 2.13 Edge Effect Shear.

relieved by deformation towards the nearest outside edge of the work material, PQ, rather than by conventional primary shear. Material from this region forms the minor chip which may be observed as segmented features along the major chip under certain cutting conditions.

Figure 2.14 shows minor chip formation where the spindle has been stopped with the tool remaining in the cut. (The tool has been removed from the field of view). Although minor chip flow in the last segment formed is modified by the falling surface speed, the origin of the minor chip is clearly demonstrated. Material in this hatched region (figure 2.13) is assumed to flow in the radial direction, although it can be seen (figure 2.14) that flow tends to occur in a direction perpendicular to the major chip flow.

The distance, PR (figure 2.13) over which the minor chip mechanism operates is less than the length PQ because the material involved must shear from both the bulk of the work material (i.e. along PR) and the major chip (i.e. along RS). A range of values of RS/PR was tested in the MLP model. A value of RS/PR = 0 simulates the case in which no minor chip is formed and all material undergoes conventional primary shear. A value of RS/PR = 1.5 was found to produce variations in x and y components of frictional force with feed similar to those recorded experimentally. See section 4.3.1.

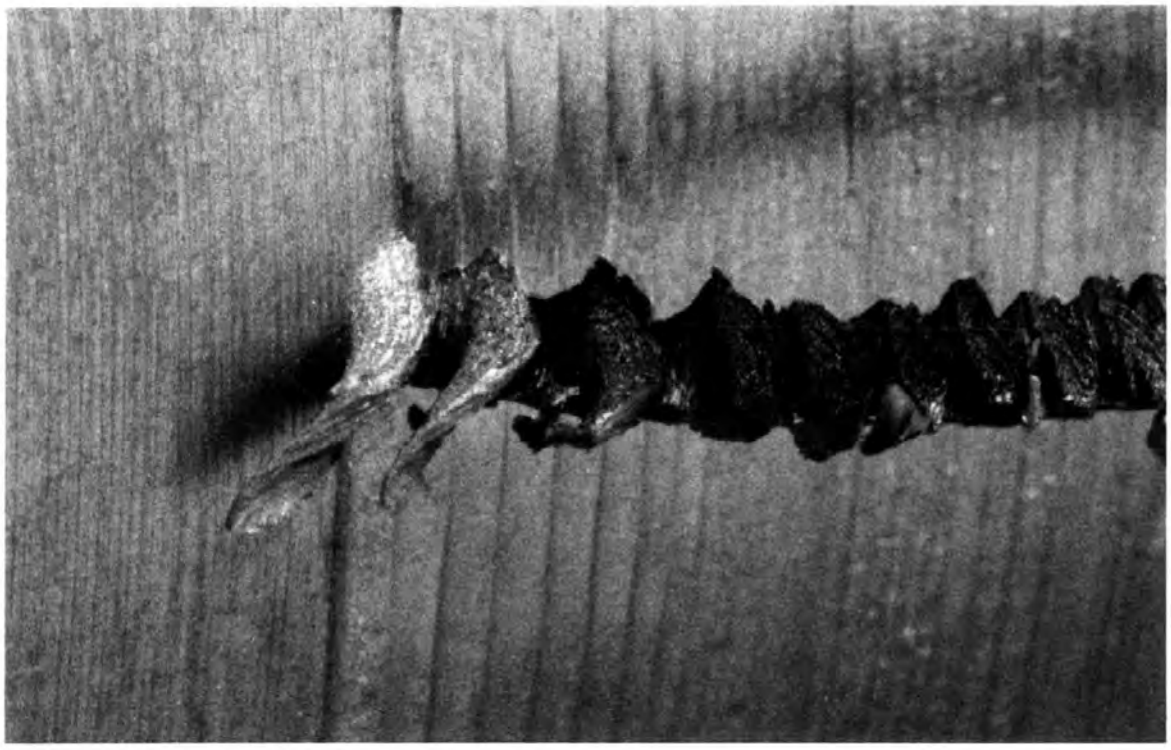

Figure 2.14 Minor Chip Formation By Edge Effect Shear.

2.10.2.2 Shear Angle Invariance.

The primary shear angle, ϕ, was assumed independent of the undeformed chip thickness, AB, CD, etc. (figure 2.12) The magnitude of elemental frictional force was assumed to increase linearly with local undeformed chip thickness [71].

Details of experimental cutting conditions are set out in table 2.1.

Table 2.1. Experimental Cutting Conditions.

Feedrate	= 0.2, 0.4, 0.6, 0.8, 1.0, 1.2 mm/rev.
Surface speed	= 40 m/min.
Depth of cut	= 1.0 mm.
Side rake angle	= 0 degrees.
End rake angle	= 0 degrees.
Side cutting edge angle	= 2 degrees.
End cutting edge angle	= 2 degrees.

2.10.3 The Minimum Global Path Length Model.

In the MLP model it was assumed that the bulk chip flow angle could be determined as the integral of all elemental chip flow angles. This is not the case, since the behaviour of each element is modified by the constraint that all chip flow will

assume one direction. In figures 2.15 and 2.16, point A lies on the cutting edge and point B on the projected outside surface of the work material formed during the previous workpiece revolution.

For a tool with a nose radius, a feature of the geometry of the primary shear plane is that the primary shear plane area varies with chip flow angle, and there exists a chip flow angle which minimises primary shear plane area. The evaluation of primary shear plane area involves lengthy calculations, since the simple trigonometric relationship

$$\text{Primary shear plane area} = \frac{F.DOC}{\sin\phi}$$

describes the projection of the undeformed chip cross section onto a two dimensional plane surface. In the case of a tool with a nose radius this surface is curved.

However, the variation of the primary shear plane area with chip flow angle may be studied indirectly using a simpler system exhibiting sufficiently similar properties. The integral of flow paths over engaged cutting edge length is such a system (see appendix 10).

For constant shear angle, ϕ, the length AB is directly proportional to both the primary shearplane length, AE, and length of sticking contact between the chip and tool. The chip

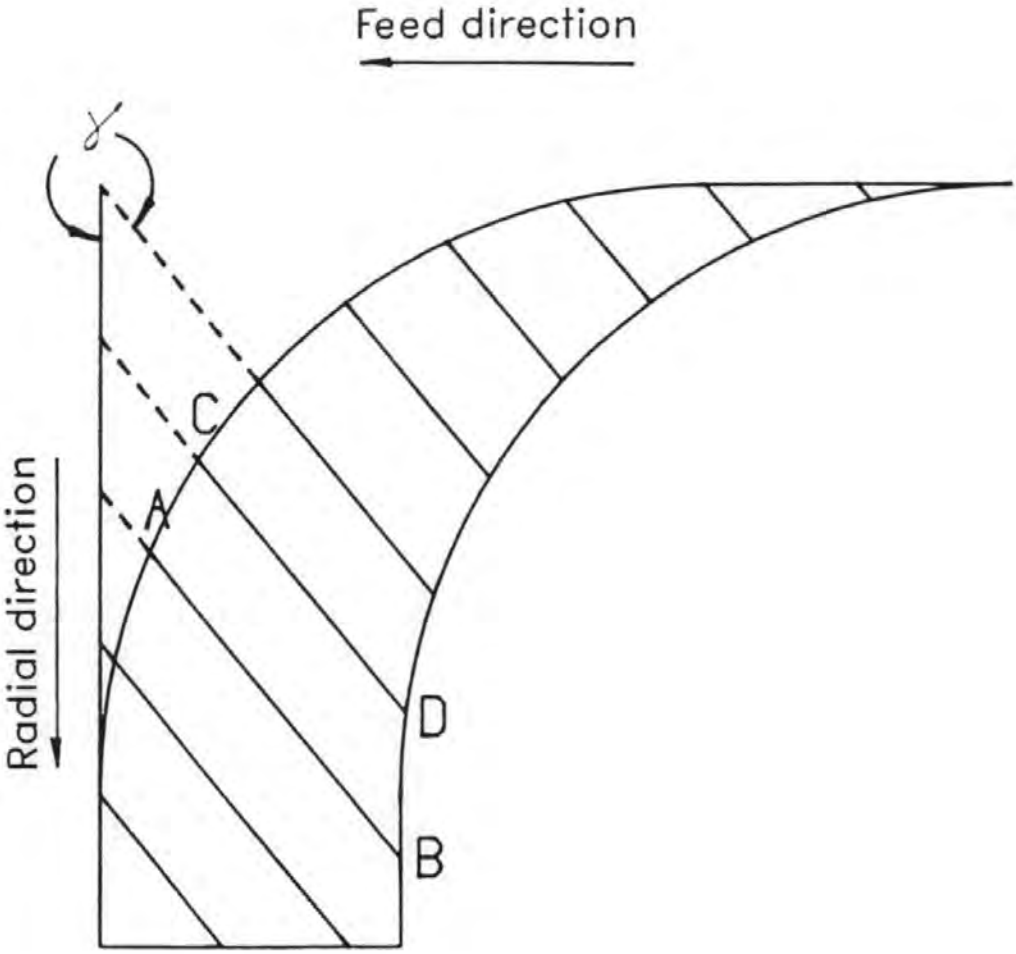

Figure 2.15 Chip Flow. (Minimum Global Pathlength Model).

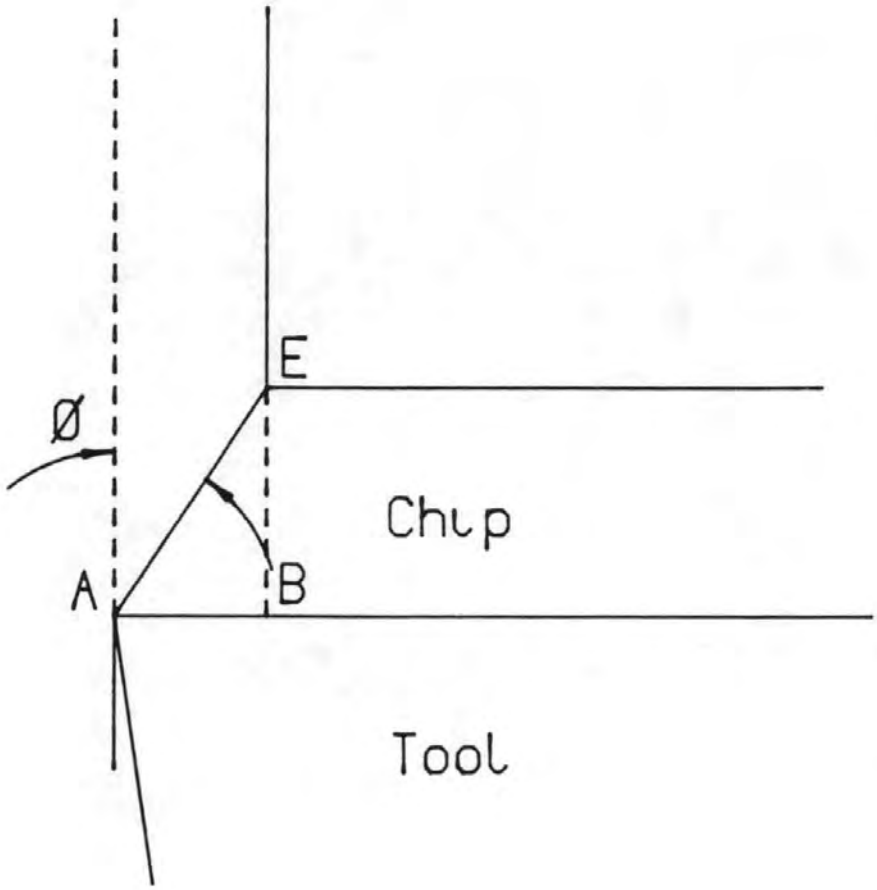

Figure 2.16 Geometry of The Minimum Global Pathlength Model.

flow angle minimising the integral of all flow line path lengths (AB, CD etc. figure 2.15) over engaged cutting edge length will minimise the primary and secondary shear force. This forms the basis of the minimum global pathlength (MGP) model. The implications of integrating over the engaged cutting edge length, rather than dS, are discussed in appendix (2).

Pathlengths were measured from a diagram similar to figure 2.15, drawn using a CAD package. The global pathlength integral is obtained by integrating these pathlengths (AB, CD etc. in figure 2.15) over the engaged cutting edge length (figure 2.17). This procedure was repeated for a range of chip flow angles. A graphical method of integration was favoured by a number of factors:

(i) The derivation of an explicit expression for the integral is extremely involved. The tool profile must be described mathematically. For tools with a nose radius this is comparitively simple, although a number of domains must be constructed to describe the curved and straight sections of the engaged cutting edge. The description of form tool profiles would be more involved.

(ii) An explicit expression for the integral must be derived for every cutting geometry. i.e. for every

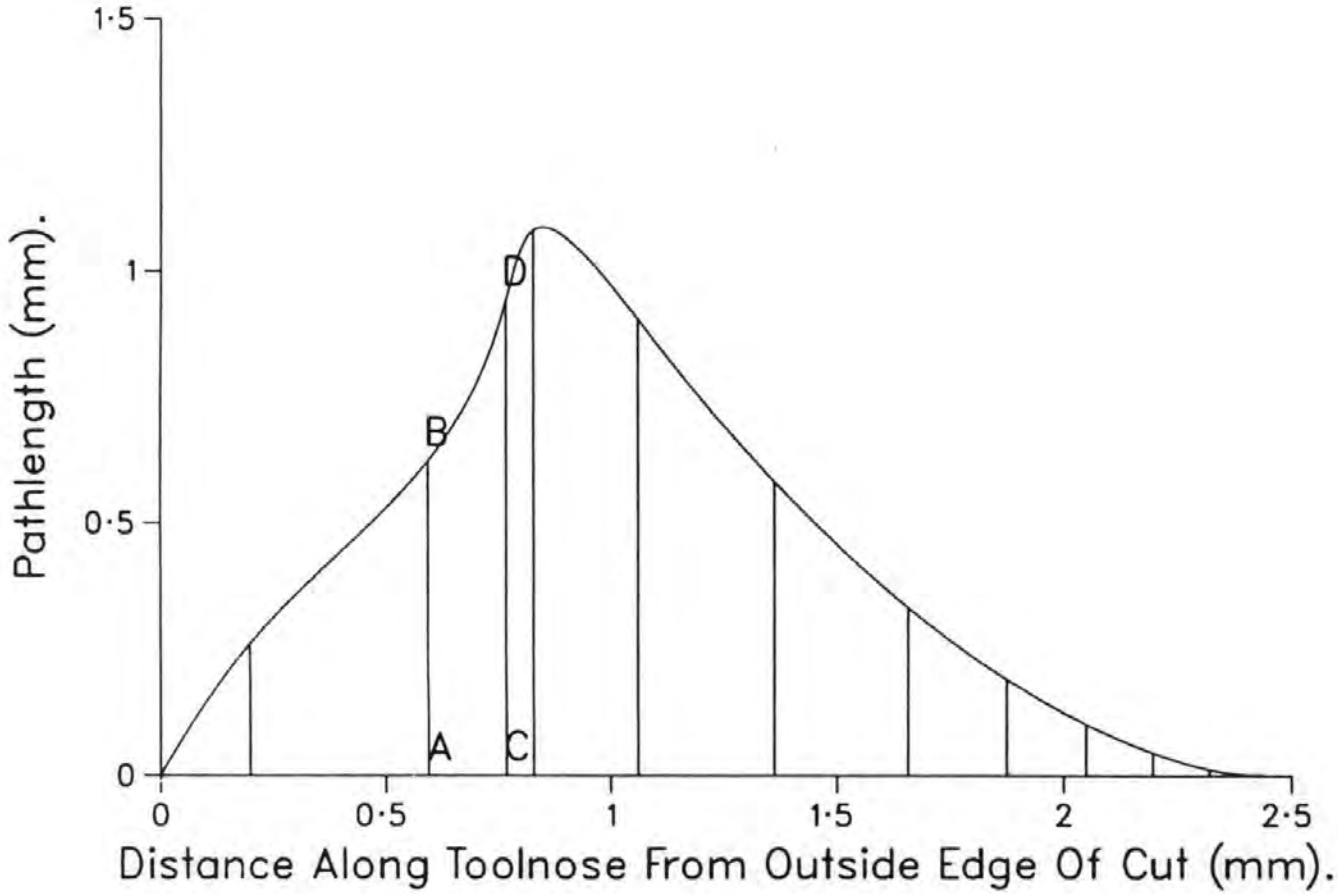

Figure 2.17 Graphical Integration Of Flow Pathlengths.

feedrate and depth of cut.

(iii) If the pathlengths are derived graphically using a CAD package, graphical integration may be carried out on the screen.

(iv) Conceptual simplicity is an another attractive feature of the graphical method.

The measurements of pathlengths from drawings provided sufficient information for this limited study. However, a mathematical description of the toolnose and workpiece boundary positions would form the basis of a model more easily adapted to study a variety of similar tool nose profiles.

2.10.3.1. Future Adaptions And Modifications.

The MGP model presents a sound theoretical basis for predicting chip flow angle. A number of areas for refinement are suggested by the author :-

(i) Modelling edge effect shear.

(ii) Modelling the variation of primary shear angle around the engaged cutting edge.

(iii) Modelling the effect of rake angle.

Variation In Primary Shear Angle.

Some variation in primary shear angle will accompany the variation in undeformed chip thickness around the toolnose. This leads to local variation in chip velocity which will both effect the chip flow angle and cause the chip to curl. Modelling the variation in primary shear angle will increase the accuracy with which chip flow angles may be predicted. Modelling the variation in chip velocity may make possible some contribution to chip control.

Rake Angle.

Modelling the effect of rake angle introduces the effect of chip flow angle on effective rake angle (section 2.9.1). In addition to compensating for variation of primary shear plane area (and thus chip tool contact pressure) with effective rake angle in establishing the minimum energy condition, the influence of effective rake angle on built up edge stability must also be taken into account. Variation in built up edge stability with undeformed chip thickness also complicates this issue.

2.11 Temperature.

The effect of temperature on wear modes is demonstrated by the disproportionately accelerated growth of crater wear scars in H.S.S. tools at higher cutting speeds. From dimensional analysis a rough estimate of the temperature rise can be made, assuming that all energy is converted into heat. Initial work by Kronenberg [72] was refined by Shaw [73] to yield an expression for surface temperature.

$$T = E\left(\frac{vt}{k\rho c}\right)^{1/2}$$

Where E = specific cutting energy

v = cutting (surface) speed

t = undeformed chip thickness

k = thermal conductivity

ρ = density

c = specific heat of work material

Because the cutting zone is continually moving into the workpiece, little heating ahead of the tool is expected and in cutting at higher speeds most heat (over 80 %) [43] is carried away by the chip.

The maximum tool temperature occurs on the rake face some

distance from the tool nose and results from rubbing and shear in the secondary zone. Softening of the tool and reduction of the contact length decreases the apparent mean coefficient of friction, but the elevated temperature reduces the useful working life of the tool. Thus wear may increase as the mean apparent coefficient of friction decreases.

Work material properties should be considered when interpreting experimentally determined tool temperatures. Nickel alloys tend to loose shear energy to the tool, rather than gaining frictional energy during sliding. The resulting tool temperature distribution will differ from that produced when cutting steel under similar conditions [48].

Work material properties also vary with temperature. The critical shear stress of steels generally decreases with increasing temperature and this effect becomes significant below the temperatures encountered during metal cutting operations.

Measurement of tool temperature is discussed in Chapter 3.

Chapter 3. Experimental Techniques.

3.1 Tool Geometry.

A wide range of tool geometries is used in industrial metal removal. For this series of studies, a geometry was selected which demonstrated industrial relevance whilst retaining some geometric simplicity. Bar turning and a large nose radius were chosen to simulate industrial practice. Zero end rake angle was a feature common to all tests in order to simplify the resolution of cutting forces into components relative to the rake face. For the same reason, zero side rake angle was maintained in the surface speed and feedrate tests. Side and end cutting edge angles were set to 2 degrees to provide adequate end clearance while maintaining a negligible approach angle.

By the use of such tools with such geometry individual trends in the data were more easily recognised and isolated.

3.1.1 Rake Angle.

In order to study cutting forces over a range of side rake angles a tool holder with a variable geometry was manufactured (figure 3.1). The side rake angle of the tool was adjusted by rotating a cylinder, on which the insert tool was mounted, within a sleeve, to align two pairs of tapped holes in the

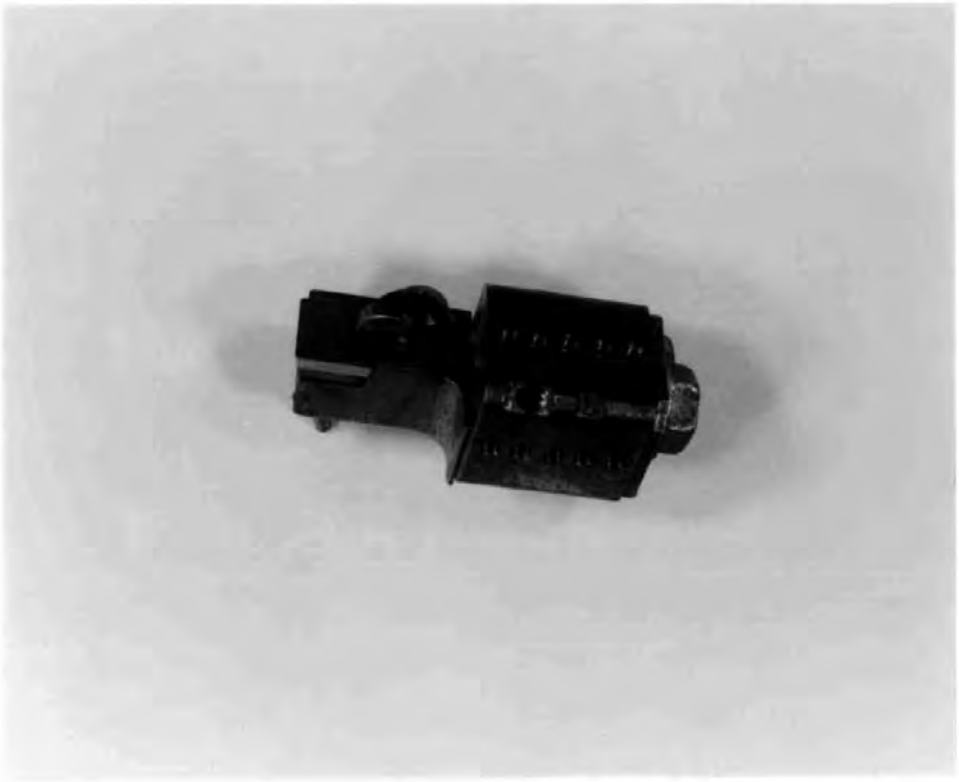

Figure 3.1 The Variable Rake Angle Tool Holder.

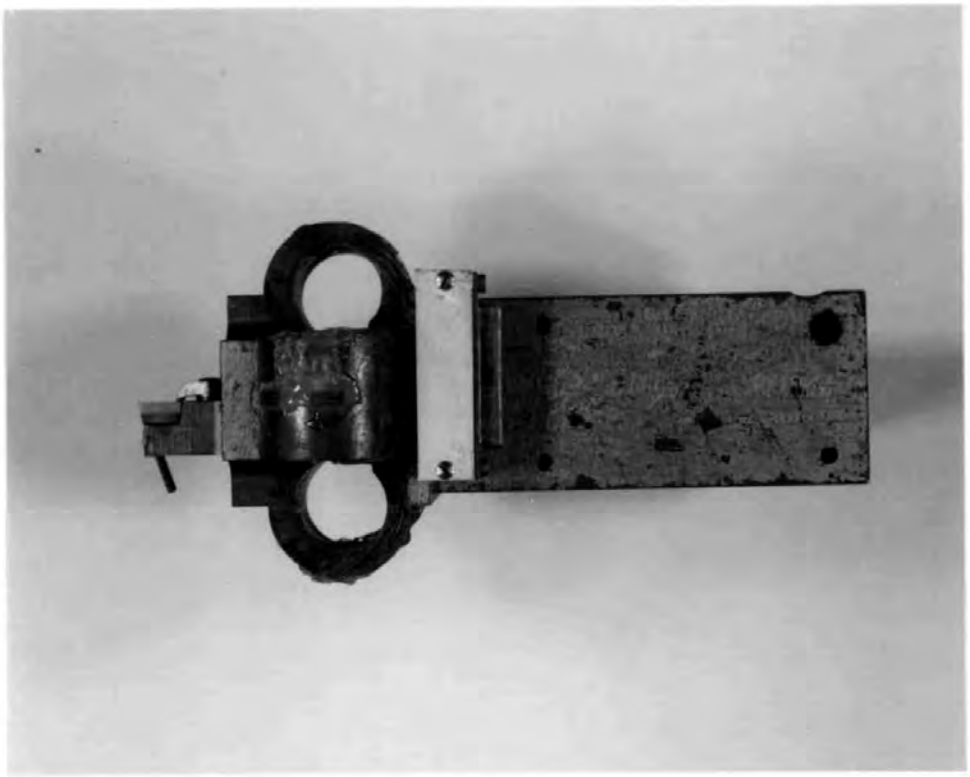

Figure 3.2 The Dynamometer.

sleeve and cylinder. Grub screws were inserted to fix the position of the cylinder in the sleeve, and the entire assembly was mounted in the dynamometer.

After manufacture, the side rake angles were measured using a vernier protractor. These are given in table 3.1.

Table 3.1. Side Rake Angles Used In Cutting Tests.

Nominal angle. (degrees)	Measured angle. (degrees)
7.5	8.0
6.0	6.1
4.5	4.6
3.0	3.0
1.5	1.2
0.0	0.0
-1.5	-1.6
-3.0	-3.0
-4.5	-4.0
-6.0	-5.7
-7.5	-7.3

3.2 Measurement of Cutting Forces.

Cutting forces were measured using a three axis dynamometer (figure 3.2) manufactured following a design by Boothroyd and Childs. The forces experienced by the tool during turning were transmitted to four equally stiff semi circular arms. Strain gauges were mounted on these arms in pairs, one pair covering a node for stress imposed by loading along the dynamometer axis (radial force), and the other pair covering a position sensitive to both axial (radial) and trans-axial (tangential and longitudinal force) loading.

Four full Wheatstone bridges were constructed. Those bridges containing gauges sensitive to stresses imposed by both axial and trans-axial loads were constructed such that trans-axial loads unbalanced both sides of the bridge equally. The initial differential signal amplification rejected such common mode signals. Thus only axial loading caused asymmetric imbalances in these bridges which were amplified and recorded. In this way the cutting force was resolved into three axial components.

3.2.1 Signal Production.

The strain gauges measuring each component of force were arranged in full Wheatstone Bridges. Insulating the strain gauges and conductors from electrical noise was not practically possible, and so the length of conductor between gauges was

adjusted so as to maintain symmetry about the input to each circuit. Thus the spurious signals picked up by either side of the circuit would be largely equivalent and in phase.

3.2.2 Signal Conditioning.

Electrical noise, predominantly at a frequency of around 50 Hz remained a problem despite these precautions. A passive low pass R-C filter was installed on each channel of the dynamometer, which reduced the noise level to around the limit of resolution of the recording system. The attenuation of transients and retention of steady state signal amplitude is illustrated by the reponse charactaristic (figure 3.3). The strain gauges were sealed to prevent corrosion of the contacts and damage by small metal particles. A sheet metal cover was fitted to the measuring assembly in order to prevent contact with metal chips.

3.2.3 Signal Amplification.

Each bridge circuit was amplified in two stages with a nominal overall gain of around 30,000. The first stage amplified the difference between the potential of the two output terminals. Any noise signal tended to be lost. In order to minimise noise the amplifiers were positioned on the side of the dynamometer itself, thus reducing the length of lead carrying signals prior to amplification. The signal leads were connected to the

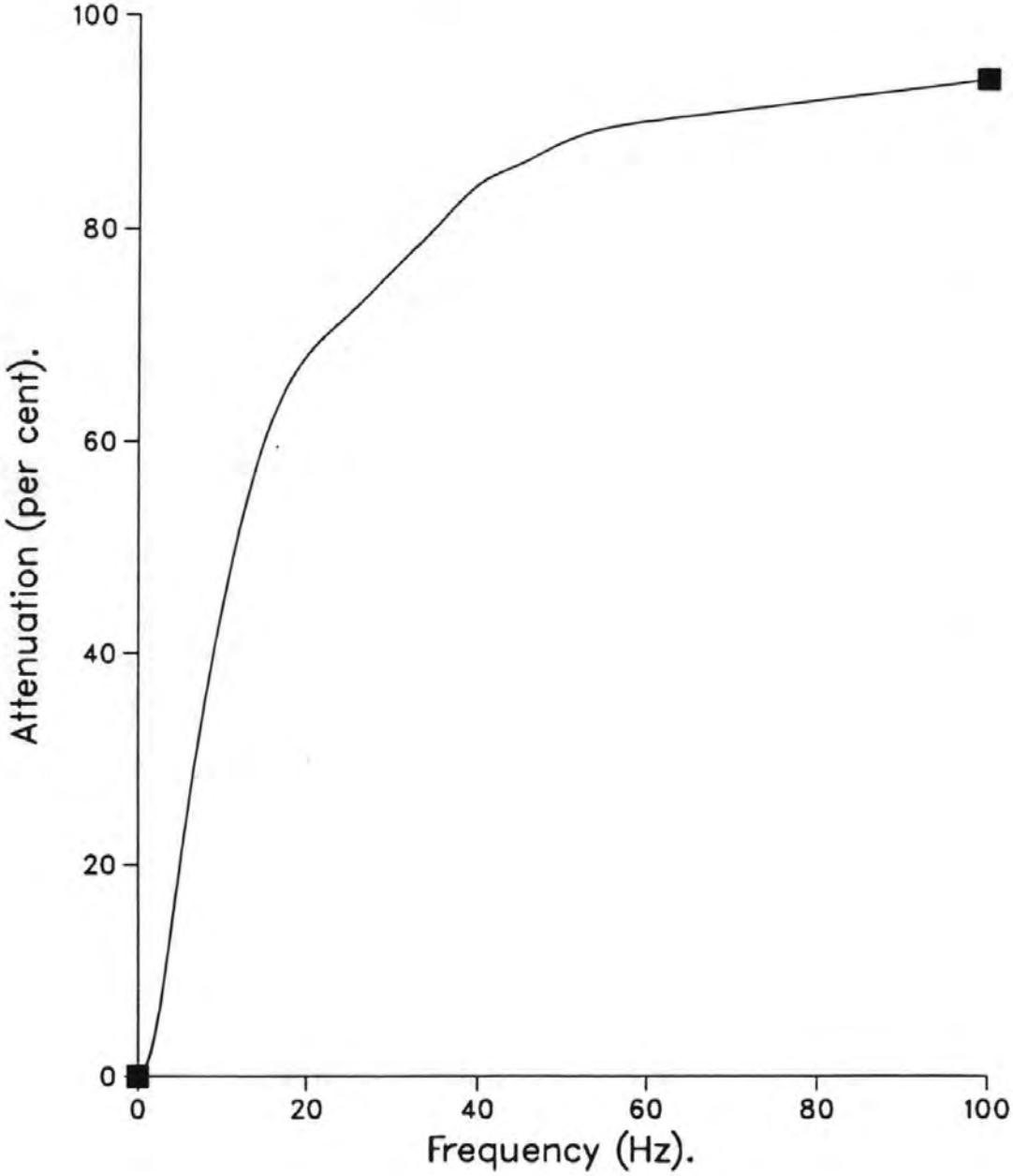

Figure 3.3 Filter Response Characteristic.

amplifiers by a 25 pin D plug for ease of assembly and fault finding (figure 3.4).

3.2.4 Data Acquisition.

The amplified signals were digitised using 4 channels of a multichannel 12 bit analogue to digital converter and stored using an Apple microcomputer. Although the signal from each channel could be adjusted using a variable resistor in the first stage amplifier, the reading was zeroed by recording the unloaded signal shortly before each cut and subtracting this from subsequent readings before storing them on disc. Using a program written in BASIC the four channels used to record force data and a fifth used to record temperature data could each be sampled at 3.3 Hz.

3.2.5 Data Processing.

Initial calibration was performed using an Instron testing machine. However, the instability of the loading over even the short time required to obtain a set of readings was an unacceptable source of error. Further calibration was performed using dead weights on a cantilever to provide loads from 219.0 Newtons to 1970.6 Newtons at increments of 87.6 Newtons. The calibration coefficients in table 3.2 were obtained.

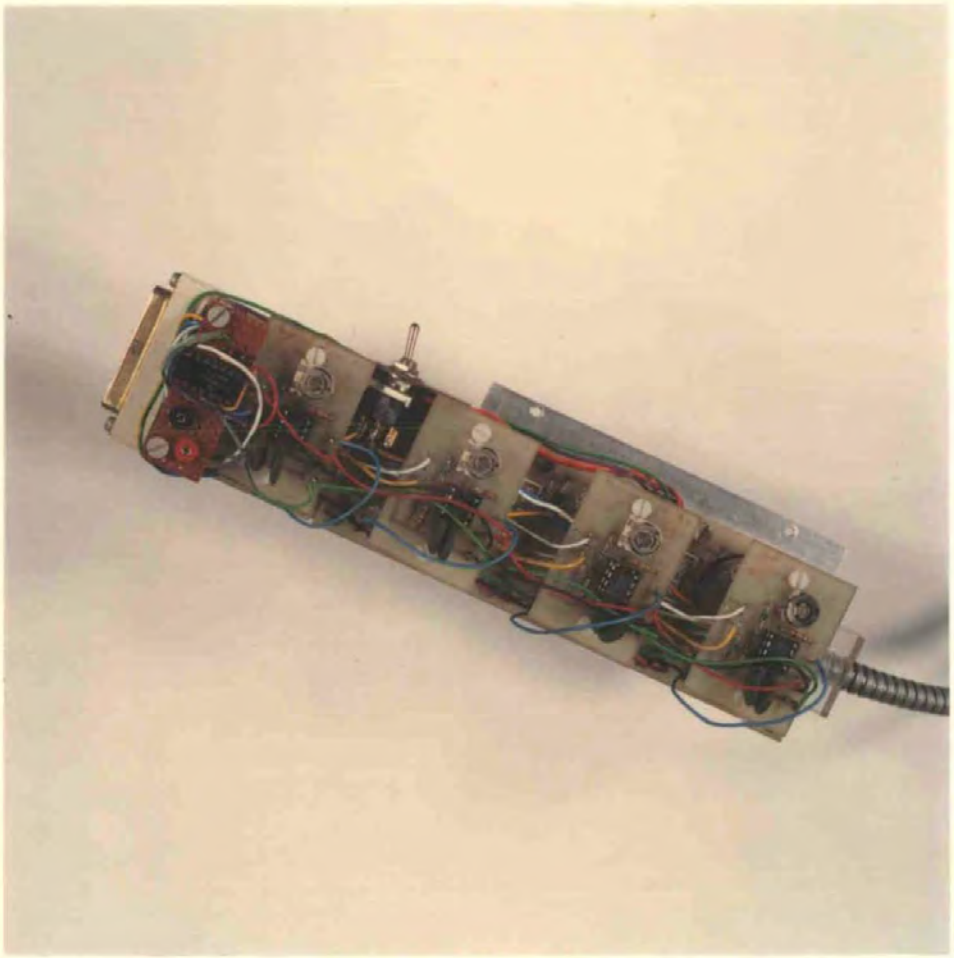

Figure 3.4 Strain Gauge Amplifier Circuits.

Table 3.2. Dynamometer Calibration Coefficients.

t1 = -1.02325 divisions per Newton.

t2 = -0.01125 divisions per Newton.

t3 = -0.0065 divisions per Newton.

l1 = -0.02825 divisions per Newton.

l2 = -1.148 divisions per Newton.

l3 = -0.1315 divisions per Newton.

r1 = -0.0225 divisions per Newton.

r2 = -0.01575 divisions per Newton.

r3 = 1.3235 divisions per Newton.

Where tn, ln and rn represent the sensitivity of bridge n to tangential, longitudinal and radial loading respectively. The following calibration equations were then constructed.

Reading(1) = Ft(t1) + Fl(l1) + Fr(r1)

Reading(2) = Ft(t2) + Fl(l2) + Fr(r2)

Reading(3) = Ft(t3) + Fl(l3) + Fr(r3)

Where the readings 1 to 3 are the recorded amplified bridge imbalances and the bracketed coefficients are calibration constants.

To a first approximation, coefficients other than t1, l2 and r3

may be regarded as zero, and forces derived directly from the amplified bridge imbalances, readings 1, 2 and 3. However in order to account for the cross sensitivities, the calibration equations were solved simultaneously for the three force components, using Gauss Siedel iteration. This method is described in appendix 3.

3.2.6 Accuracy and Precision.

The major calibration coefficients,t1, l2, and r3 have units divisions per force and appear to indicate a resolution of 0.977, 0.871 and 0.811 Newtons for Ft, Fl and Fr respectively. However, accurate transfer functions (table 3.4) were derived from dummy data (table 3.3) using the Gauss Seidel program.

Table 3.3. Data Used To Derive Dynamometer Transfer Functions.

Reading (1)	Reading (2)	Reading (3)	Tangential Force (Newtons)	Longitudinal Force (Newtons)	Radial Force (Newtons)
-100	-100	100	93.52	85.03	84.46
-101	-100	100	94.50	85.02	84.46
-100	-101	100	93.49	85.90	84.55
-100	-100	101	93.50	85.02	85.21

Table 3.4. Dynamometer Transfer Functions.

	Tangential force per reading. (Newtons)	Longitudinal force per reading. (Newtons)	Radial force per reading. (Newtons)
Channel(1)	0.98	0.01	<0.01
Channel(2)	0.03	0.87	0.09
Channel(3)	0.02	0.01	0.75

3.3 Temperature Measurement.

Due to the hostile nature of the environment surrounding a machine tool cutting edge, there are limits to the choice of technique which may be used to measure temperature. In addition, the velocity of material passing the tool surface is high, prohibiting the use of methods involving heat transfer through physical contacts.

In the context of this study the following factors were considered :-

(i) The variation in tool temperature due to nitriding.

(ii) The variation in tool temperature with cutting forces.

(iii) The distribution of heat generated during cutting.

3.3.1 Appraisal Of Techniques.

Temperatures were measured using three techniques:-

(i) Temperature sensitive paints.

(ii) Infra red photography.

(iii) Implanted thermocouples.

Although work with implanted thermocouples provided the most manageable data, some useful qualitative information was produced using the other two techniques.

3.3.2 Temperature Sensitive Pigments.

The initial tests using temperature sensitive pigments involved sandwiching the pigment solution between two halves of a high speed steel insert. This was achieved using a pair of T42 inserts in each test, removing material from the top of one and the base of the other. This produced, in effect, a tool split across at a distance (0.5 mm) from the cutting surface.

The lower surface of the upper half was then painted with a uniform layer of the pigment in order to ensure a high heat transfer coefficient between the tool and paint. Excess solvent was driven off in an oven at a temperature significantly below the critical temperature of the paint. The two halves of the tool were then clamped together in the tool

holder and this was used to cut metal on a lathe.

A problem with this technique was that at the elevated temperature and high normal pressure encountered in metal cutting, solvent formerly stable in the pigment layer was liberated, allowing the painted layer to be distorted under the high load. This caused the paint to thin at the cutting edge and reacted pigment particles to be transported into regions which had not risen above the critical temperature. These factors adversely effected the accuracy with which the critical temperature contour could be determined.

In order to overcome these problems the lower half of the insert was further modified. A depression was electrochemically machined in this section to accommodate the pigment layer, leaving a narrow step around the perimeter of the depression to maintain a clearance. The top part of the tip was painted in the region corresponding to this depression and oven dried before being assembled with the lower section in the tool holder. A series of tests were performed to assess the accuracy of the method. Figure 3.5 shows an example of a temperature contour determined using this technique.

Each critical temperature quoted in the results section corresponds to a different pigment system. Because a dynamic proportion of pigment molecules attain critical energy, critical temperature varies as a function of time. Critical

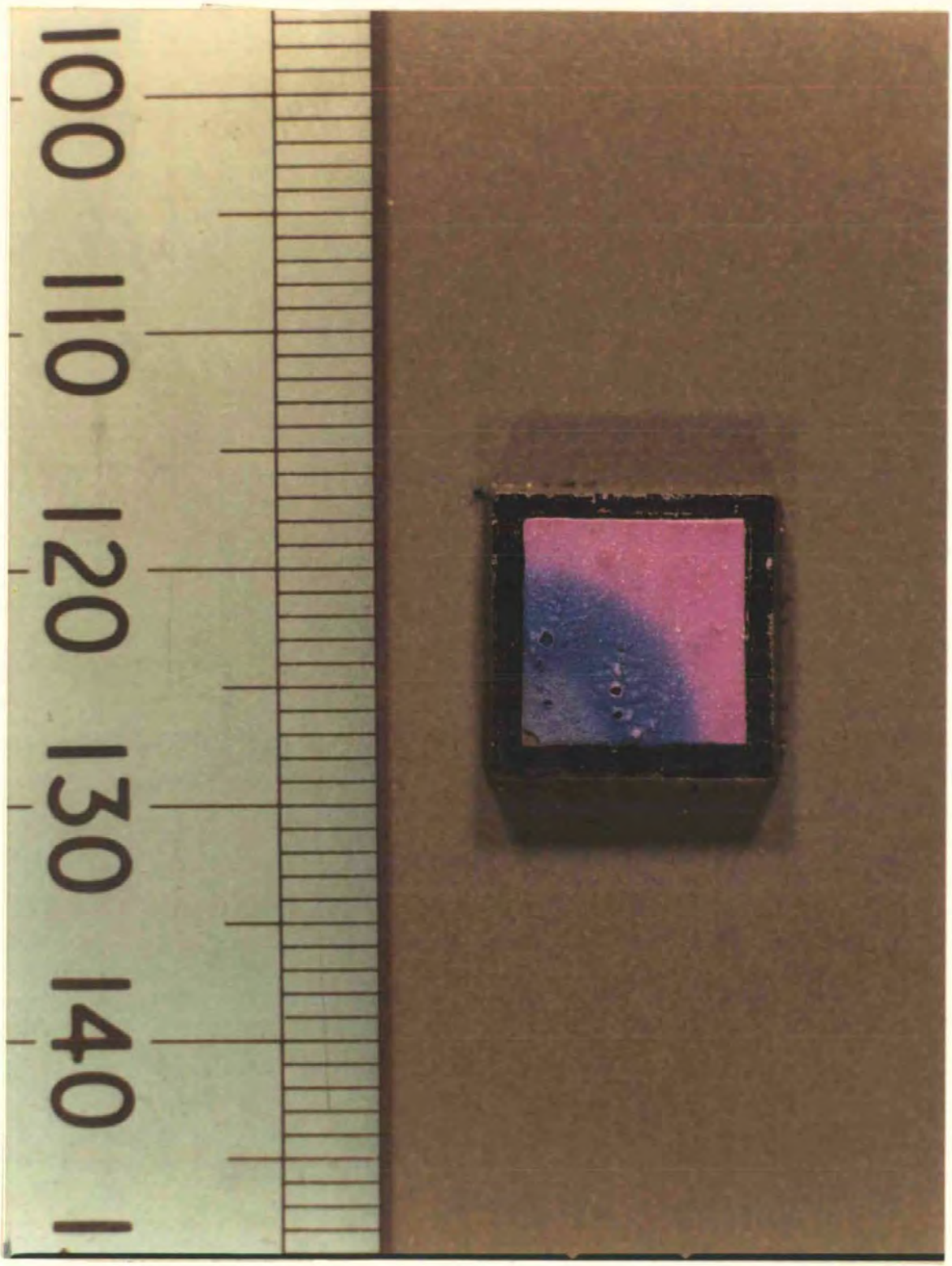

Figure 3.5

An Example Of A Temperature Contour Recorded Using Temperature Sensitive Paints.

temperature values were extrapolated from the manufacturers calibration data to fit the test duration. A comparison of nominal and calculated critical temperatures is given in table 3.5

Table 3.5.

Critical Temperatures Of Temperature Sensitive Pigments.

Nominal Value (°C)	Actual Value (°C)
120	156
165	162
235	252
250	317
350	387

Mean distances between critical temperature boundaries and the cutting edge were measured using an optical microscope. Cutting conditions are given in table 3.6.

Table 3.6. Cutting Conditions Employed During Studies Using Temperature Sensitive Paints.

Test duration	= 2 minutes.
Depth of cut	= 1.0 mm
Feedrate	= 0.5 mm
Surface speed	= 35 m/min.
Rake angle	= 0 degrees.

A finite element model of the insert tool was developed in order to assess the effect of the paint layer on heat flow in the tool. This is described in appendix 4.

3.3.3 Infra Red Thermography.

The time available for the study of tool temperature distribution using infra red thermography was restricted, since the equipment available was on loan from the S.E.R.C. to another project. The Agema infra red thermography equipment was supplied with a BMC microcomputer and Thermotechnix image analysis software. The microcomputer and associated software enabled the monochrome scanner image to be digitised. The grey level of each pixel was then converted from a thermal level into an absolute temperature, taking into account emmission, reflection and transmission parameters.

In order to view the rake face of the tool it was necessary to measure temperatures immediately after cutting stopped. The

following factors also hindered the use of infra red thermography.

3.3.3.1 Camera Proximity.

Infra red transparent optics are costly and easily damaged. A lens suitable for enlarging close up work was not amongst those available. The arrangement in figure 3.6 involved reflecting the image on a front - silvered mirror, but left the tool occupying a small part of the field of view even at the close limit of focus.

3.3.3.2 Image Processing.

The software supporting the image processing required values of thermal emissivity for accurate calibration. Minimal wear created regions with modified thermal emissivity. This was a particular problem with nitrided tools, for which the emissivity of the black surface varies from that of adhering work material and the underlying steel substrate.

The software was not suited to processing images containing a number of objects. Sharp temperature changes demarking one body from another were broadened by the insertion of contours illustrating a steep thermal gradient. Such boundaries exist between the tool and work material fragments in the lathe bed, airborne, and lying around the tool. In order to obtain a

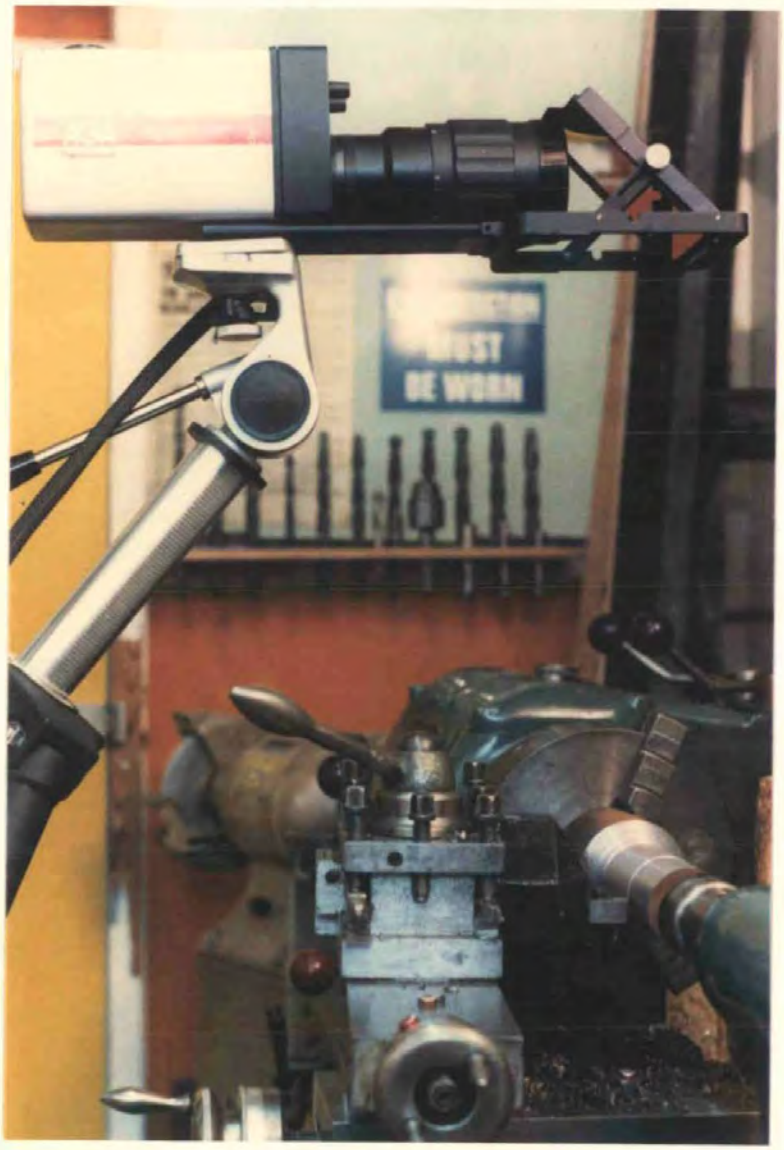

Figure 3.6 Infra – Red Thermography.

Experimental Arrangement.

clear image it was necessary to sweep away metal chips and mask the lathe bed from the camera. Although this was achieved within one second of the end of cutting, temperatures in excess of 100 °C were not recorded. However some qualitative information was obtained using this technique, and is presented in chapter 5.

3.3.4 Implanted Thermocouples.

3.3.4.1 Method

Thermocouples implanted in the tool were the main source of experimental temperature data. A type K (nickel/chromium nickel/aluminium) thermocouple was used, sheathed in a minimally thermally insulated steel sleeve with an external diameter of 0.5 mm. The thermocouple assembly was inserted in a cavity electro - chemically machined in the tool tip. A number 10 embroidery needle was used as the electrode to ensure a straight cavity, leading to good thermal contact between the tool and thermocouple sleeve, minimising changes in the thermal properties of the tool. The cutting tool tip to be machined was mounted in a jig at an angle of 21 degrees to conserve the integrity of the tool nose and prevent it's loss during cutting. The tolerance on cavity depth was 0.0254 mm (1 thousandth of an inch).

3.3.4.2 Insertion.

The position of the thermocouple in the insert is illustrated in figure 3.7. A screw mechanism (figures 3.8, 3.9) attached to the underside of the tool holder and the thermocouple sleeve was used to maintain a compressive force on the thermocouple end contact.

3.3.4.3 Signal Processing.

The signal from the thermocouple was processed using an AD595 thermocouple amplifier.In order to improve the signal to noise ratio this was mounted on the dynamometer. The amplified signal was digitised by a 12 bit analogue to digital converter and stored on an Apple microcomputer.

The nominal transfer function of the AD595 is 10mV per degree. Comparison with the analogue to digital converters resolution of 2.44 mV appears to indicate that temperatures may be measured to within a quarter of a degree.
However two sources of error are present in the system. The thermocouples were manufactured to conform to BS 4937 which indicates a tolerance value of 1.5 degrees or 0.004t. The errors due to the AD595 are in addition :-

Calibration error	± 3.0°C max
Gain error	± 1.5% max

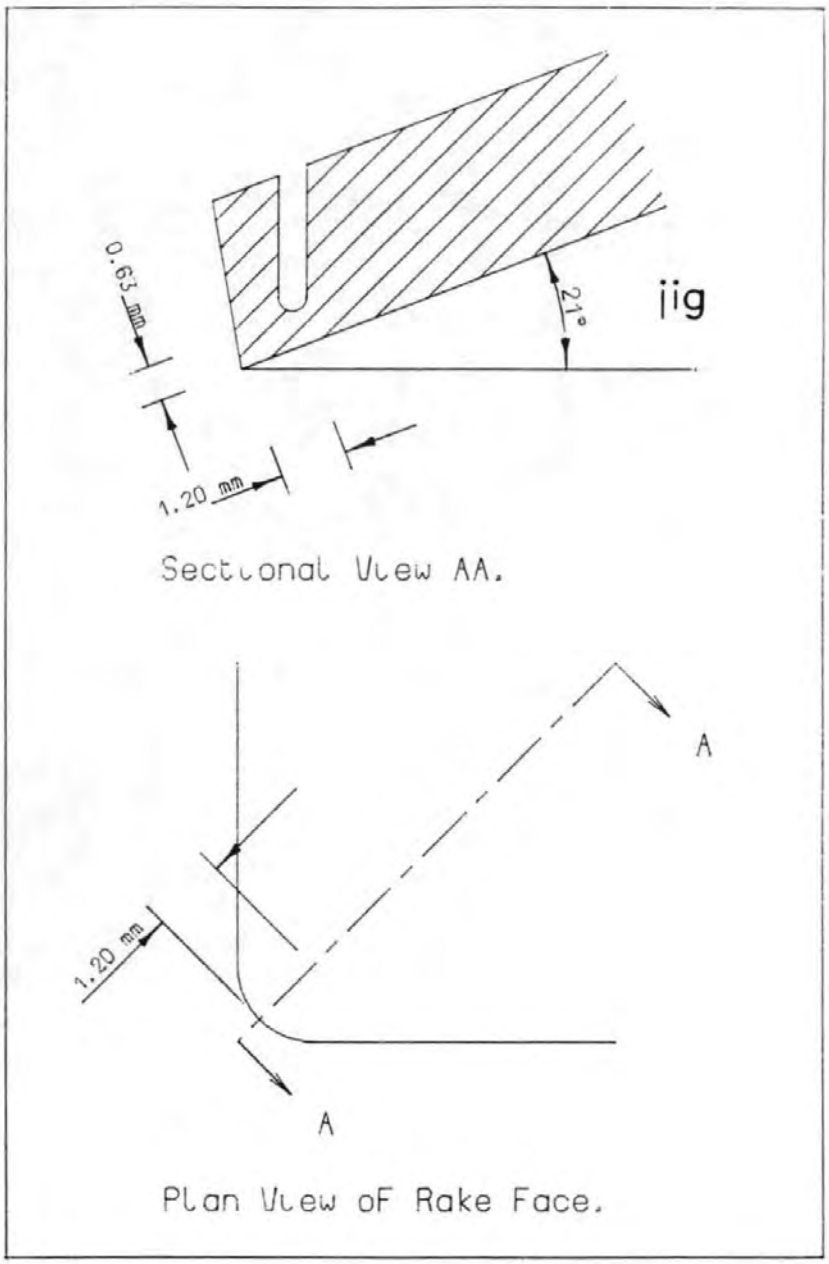

Figure 3.7 The Position Of The Thermocouple Cavity.

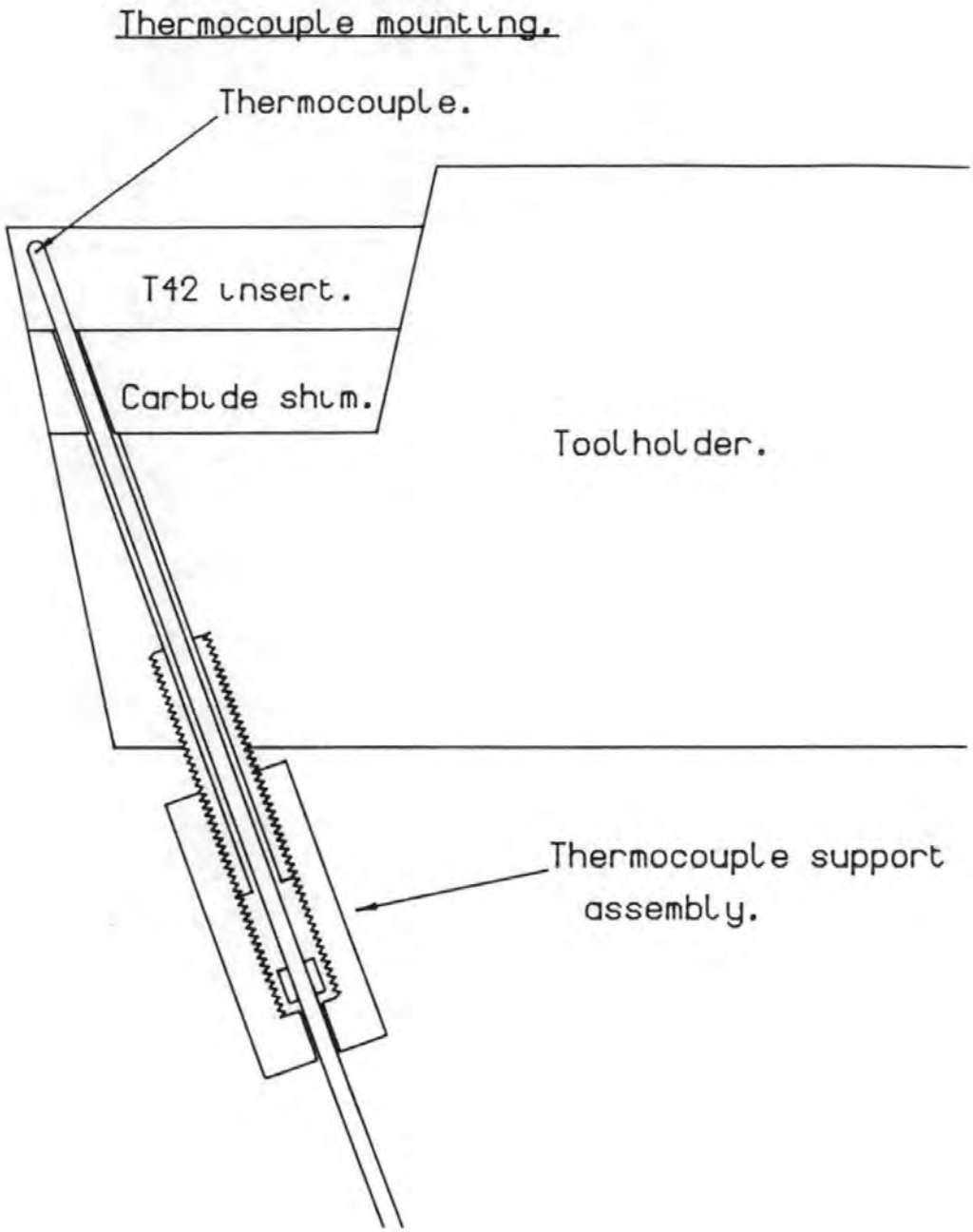

Figure 3.8 The Thermocouple Mounting Fixture.

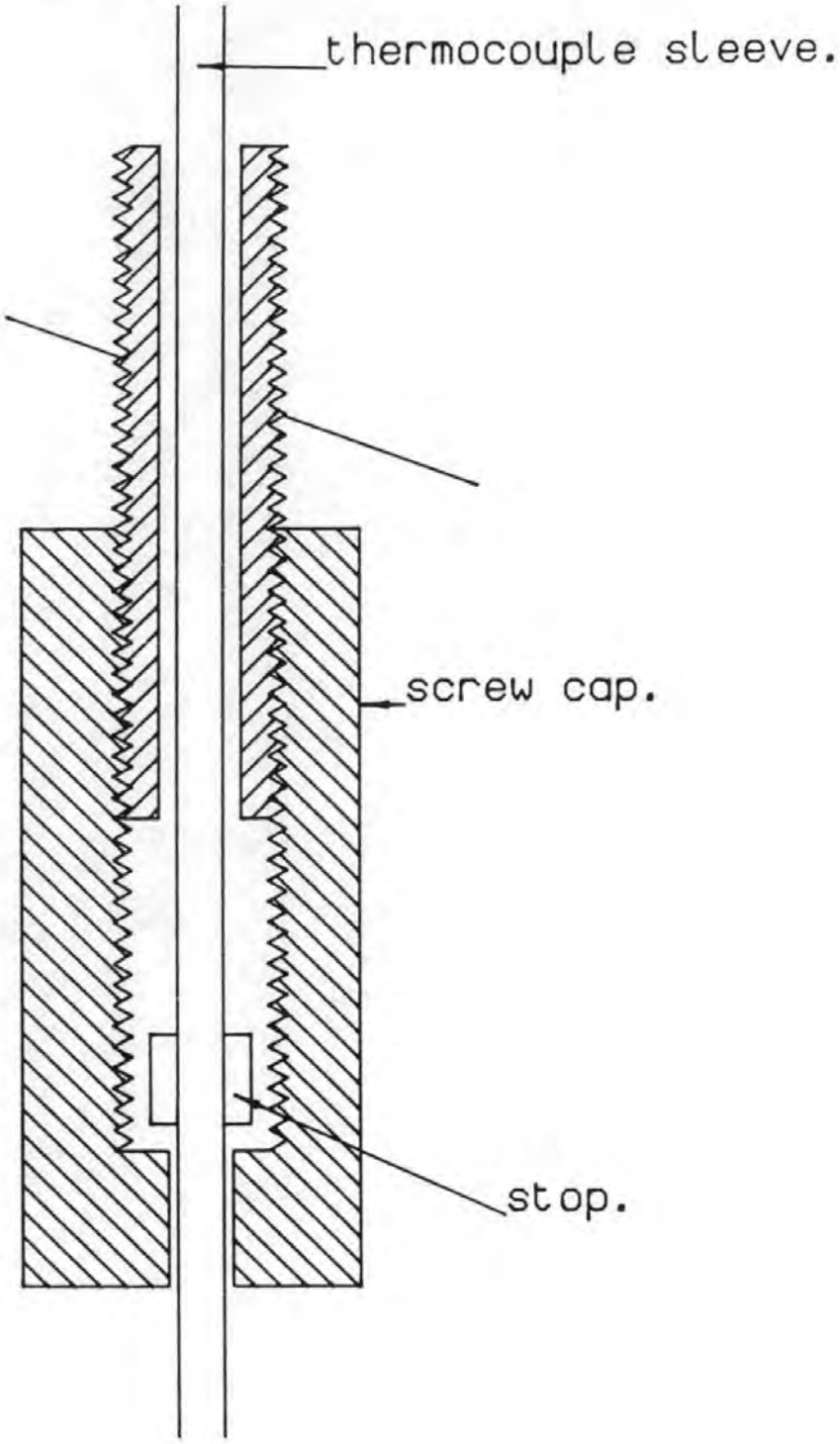

Figure 3.9 Detail Of The Thermocouple Mounting Fixture.

In the worst case this represents an error of +1.9% + 3 degrees. During the course of each study the thermocouple and amplifier were not changed. Thus although temperature measurement could not be made with an accuracy greater than that stated, the precision of the measurement remained better than 0.25 degrees. Calibration data supplied by the manufacturer indicates small variations in the transfer function of the AD595 with input voltage. In order to achieve improved accuracy mV data lying between two calibration points was converted to temperature by linear interpolation.

3.4 Cutting Tests.

Cutting tests were performed turning medium carbon steel (BS 970:1972 EN8) on a Colchester CNC500 lathe with a constant surface speed facility.

Various studies of tool life are available in the literature. For this reason the tests performed were designed to examine the parameters which determine tool life.

After extended cutting times, wear scars on the tool cause significant changes in the cutting forces and tool temperature. It was anticipated that nitriding would effect the wear rate. Tests run for 10 minutes demonstrated that very little wear occurs in the first 30 seconds of cutting. In order to obtain

force and temperature data independent of wear related phenomena cutting times of 30 seconds were employed. Thus any trends in the data would be caused by the performance of the nitrided surface.

A number of factors prevailed to restrict the data to the results of a single set of tests.

The initial design, development and manufacture of signal processing and data capture equiptment and it's subsequent modification, refinement and repair occupied a disproportionately long period in the research program. The use of a commercially manufactured dynamometer was precluded by departmental underfunding.

Intermittent faults in the delicate strain gauge and amplifier circuits required frequent investigation and repair of this prototype equiptment.

Funds for the replacement of equiptment were not available, and repairs to damaged items (particularly tool holders) within the limited technical resources made available by the department caused many long delays.

Normally data from a single set of tests would provide no information concerning the significance of trends within the data. However, forces and temperatures were digitised before being recorded, providing a pool of data from which standard deviations were derived. From these the statistical significance of variations in the data may be evaluated.

SPUN 120308 inserts, powder formed in T42 (BS 4659) were used, nitrided in a Tufftride TF1 saltbath at 587 °C. Nitriding process times are set out in table 3.7.

Table 3.7. Nitriding Process Times.

Batch 1	1210 seconds
Batch 2	610 seconds
Batch 3	310 seconds
Batch 4	140 seconds
Batch 5	70 seconds

Process times were selected to cover the range generally recomended for high speed steels in Degussa trade literature, and provide sufficient division among the range of acceptable values for an optimum process time to be established. Untreated tools were used to provide a control against which the performance of the treated tools was compared. All tests were performed without the use of lubricants, under the condition set out in table 3.8.

Table 3.8. Cutting Test Conditions.

For all of the test conditions set out below, the thermocouple was positioned 0.63 mm below the rake face of the tool (see figure 3.7).

Feedrate tests

Feedrate	0.2, 0.4, 0.6, 0.8, 1.0, 1.2 mm/rev
Surface speed	40 m/min
Depth of cut	1 mm
Side rake angle	0 degrees
End rake angle	0 degrees
Side cutting edge angle	2 degrees
End cutting edge angle	2 degrees

Rake angle tests.

Feedrate	0.5 mm/rev
Surface speed	40 m/min
Depth of cut	1 mm
Side rake angle	-7.3, -5.7, -4.0, -3.0, -1.6 degrees
	1.2, 3.0, 4.6, 6.1, 8.0 degrees
End Rake angle	0 degrees
Side cutting edge angle	2 degrees
End cutting edge angle	2 degrees

Surface speed tests.

Feedrate	0.5 mm/rev
Surface speed	20, 30, 40, 50, 60, 70 mm/min
Depth of cut	1.0 mm
Side rake angle	0 degrees
End rake angle	0 degrees
Side cutting edge angle	2 degrees
End cutting edge angle	2 degrees

3.5 Measurement Of Primary Shear Angle.

In order to determine an approximate average value for primary shear angle, the mass per unit length of the chip was measured. Chip curl prohibited the use of calipers or a ruler, and so a length of thread was held against the section of chip, such that the thread followed the entire length being measured. The thread was then removed, straitened, and measured with a ruler. The mass of the section of chip was measured, and a value for mass per unit length was calculated.

A pre - shear mass per (undeformed) chip length was calculated from feedrate, depth of cut and workpiece mass density, and the primary shear angle calculated as:

$$\phi = \tan \frac{(m/l)b}{(m/l)a}$$

where (m/l)b = undeformed chip mass per unit length.

$(m/l)a$ = post shear chip mass per unit length.

3.6 Measurement of Chip Flow Angle.

Data supplied by the dynamometer included the longitudinal and radial components of frictional force, Fl and Fr. Assuming negligible contact between the flank face of the tool and the workpiece, and the coefficient of friction between the chip and tool rake face to be isotropic, it follows that the direction of chip flow in the chip tool contact zone may be determined as

$$\gamma = \tan^{-1}(Fl/Fr)$$

where γ = chip flow angle.

Fl = longitudinal force.

Fr = radial force.

Chip curl is to be expected to introduce some error to measurements of chip flow angles obtained photographically. However, the chip flow angle determined from force measurements records the direction of chip flow within the chip tool contact zone, within which minimal chip curl will occur. For this reason chip flow angles were determined from force data.

Chapter 4. Discussion Of Experimental Results.

4.1 Introduction.

The conditions under which cutting tests were performed are described in section 3.4. The test variables were:

(i) Feedrate.

(ii) Rake angle.

(iii) Surface speed.

(iv) Nitriding process time.

The parameters measured were:

(i) Forces acting on the tool.

i.e.:- Tangential force.

Longitudinal (feed) force.

Radial force.

(ii) Temperature.

(iii) Primary shear angle.

The full tabulated experimental results are set out in appendix 5.

The results in this chapter are set out in two main parts:

(i) Results relating to predictive models of chip flow. These primarily concern non - nitrided tool tips. (sections 4.3 to 4.3.2.1).

(ii) Results comparing the performance of nitrided and non - nitrided tips. This second part is further split into the following sections:

(a) Shear mechanism related effects, including chip flow angle (sections 4.4 to 4.4.3).

(b) Stick - slip or critical frictional force. (section 4.5).

(c) Built up edge effects (section 4.6).

(d) Surface effects (sections 4.7 to 4.7.3).

(e) Tool surface performance indicated by tool temperature per frictional power. (section 4.8).

Time and cost considerations prevented a fully populated test program covering all combinations of variables from being carried out. Hence the tests were limited to varying nitriding time plus one of the three variables, feedrate, rake angle and surface speed, while keeping the other two constant.

As it was expected that the bulk of the nitrided tools would behave in a similar manner, they have been treated as a group for much of the discussion. It is clear however that the treatment time of 1210 seconds does produce results that frequently differ from the others. This is probably due to a poor surface being produced, or edge embrittlement. For some of the discussion, the variations produced by different nitriding times are examined.

4.2 Significance Of Individual Results.

Due to time constraints it was not possible to repeat experiments. However, standard deviations of all steady state forces were calculated and are set out in appendix 5. Standard deviations were all fairly similar, and much smaller than the values of the variable being measured.

Calculations of standard deviation were performed on the section of data recorded after initial transients had died away, and, due to the short duration of the tests, prior to any significant wearing of the tool. The conditions under which force measurements were obtained were the same for each test. Values of standard deviation were all less than 7%, and typically around 3% of the variable being measured, indicating that the experimental conditions in each test were fairly consistent.

4.3 Results From Chip Flow Modelling

In sections 4.3.1 and 4.3.2 results obtained using the MLP and MGP models are discussed. Those obtained from the MGP model are examined in greater detail, because this is considered to be the more valid method for estimating chip flow angle. In section 4.4 the effect of nitriding on chip flow angle is discussed in terms of the conditions prevailing in the primary

and secondary shear zones, and at the cutting edge of the tool.

4.3.1 Results Obtained Using The MLP Model.

Results set out in table 4.1 and illustrated in figure 4.1 were obtained using the MLP model. All comparative experimental results in this section were obtained using untreated tools. All values for chip flow angle are given in degrees. Experimental chip flow angles were calculated from cutting forces as:

$$\gamma = \tan^{-1} (Fl/Fr)$$

where Fl = Longitudinal component of frictional force

Fr = Radial component of frictional force

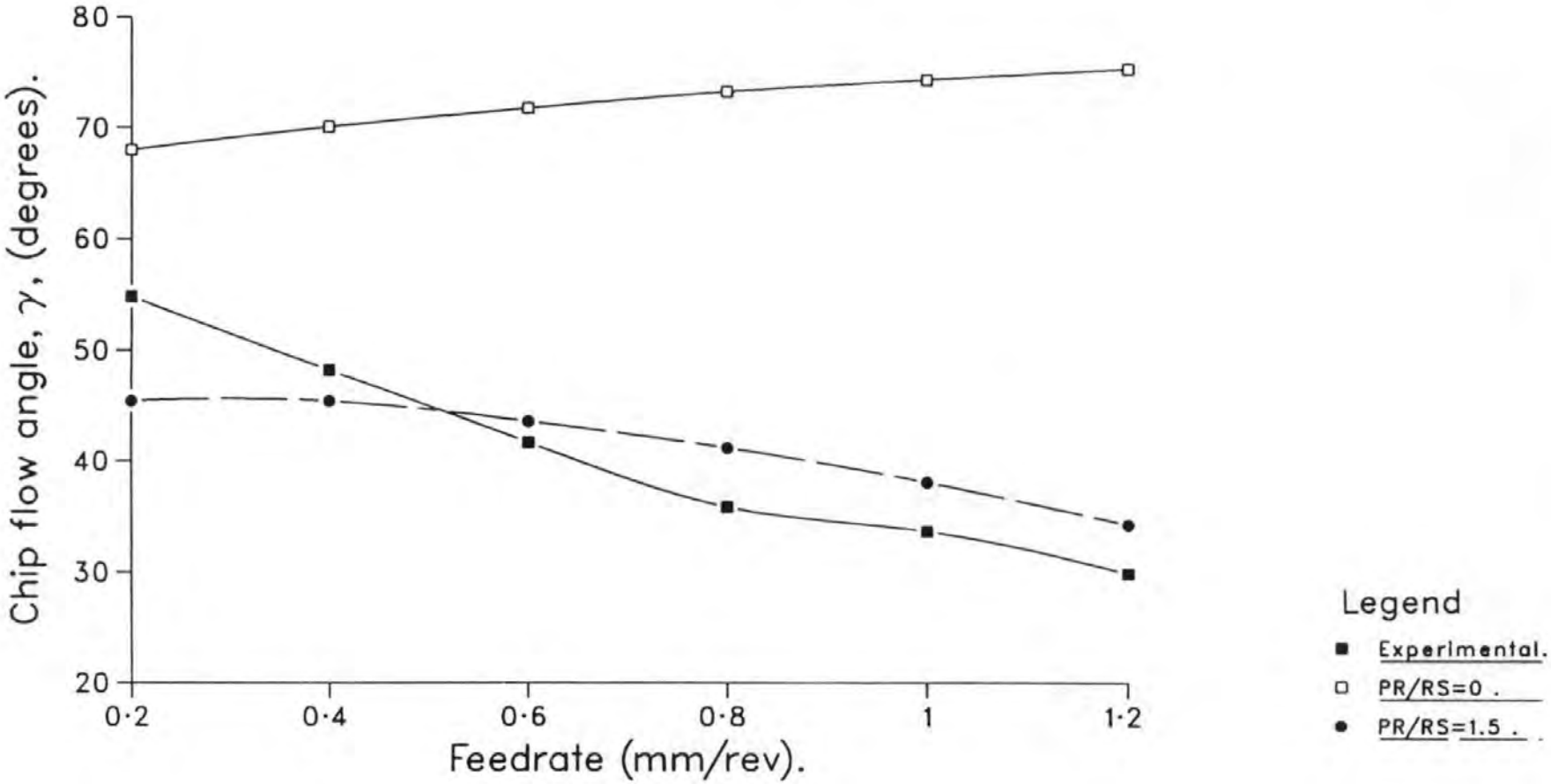

Figure 4.1 Variation In Chip Flow Angle With Feedrate.

(Minimum Local Pathlength Model).

Table 4.1.

Chip Flow Angles Predicted Using The MLP Model.

Feedrate (mm/rev)	Gamma Exp'tal	Gamma Theory (RS/PR=0)	Gamma Theory (RS/PR=1.5)
0.2	54.8	68.0	45.4
0.4	48.2	70.1	45.4
0.6	41.7	71.8	43.6
0.8	35.9	73.3	41.2
1.0	33.7	74.4	38.1
1.2	29.9	75.4	34.3

The choice of RS/PR = 1.5 reflects the increased energy required to operate the minor chip forming shear mechanism (see section 2.10.2.1). (A value of unity would be expected if the material did not also shear along PR). However, it seems likely that the choice of RS/PR = 1.5 is otherwise arbitrary, and serves only to adjust the theory to match the experimental results.

4.3.1.1 Validity Of Results.

The minimum local pathlength model predicts values for chip flow angle, and thus the direction of frictional force

experienced by the tool rake face, assumed to act parallel to the direction of chip flow. The direction of the frictional force experienced by the tool is determined from the predicted direction of the elemental frictional forces.

In predicting the elemental frictional force, the direction of chip flow is constrained theoretically only to minimise local effective undeformed chip thickness (i.e. to minimise the length of the local shear plane). However, in the real case the chip flow angle is further constrained to adopt one single value for all elements. The direction of the resultant frictional force is clearly the direction of any one (and all) of the elemental frictional force vectors. Thus the minimum local pathlength model is based on an improper description of the physical system.

The magnitude of the total frictional force, derived by integrating elemental frictional force vectors over dS, (figure 2.10), demonstrates no variation with chip flow angle, as this integral represents the cross sectional area of the undeformed chip. Such an analysis of the total frictional force may not be used to predict chip flow angle.

The shear mechanism must be re - examined in order to isolate some quantity in the system which varies with chip flow angle and exhibits some singular feature in this variation from which experimental chip flow angles may be predicted. This is achieved in the minimum global pathlength model.

4.3.2 Results Obtained Using The MGP Model.

Figure 4.2, illustrating the variation in primary shear plane area with chip flow angle, was prepared using the the trapezium segment method (see appendix 2) for the conditions set out in table 4.2.

Table 4.2.

Conditions For Calculation Of Primary Shear Plane Area.

Tool nose radius	= 0.8 mm
Feedrate	= 1 mm/rev
Depth of cut	= 1 mm
Rake angle	= 0 degrees
Side approach angle	= 0 degrees
End approach angle	= 0 degrees
Primary shear angle	= 20 degrees

(The chip flow angle minimising primary shear plane area is the same for any primary shear angle if all other conditions remain unchanged).

Although a minimum value is clearly defined, the variation in shear plane area is limited. However, this minimum represents the condition for both minimum primary shear plane area and minimum secondary shear plane energy. (For constant frictional

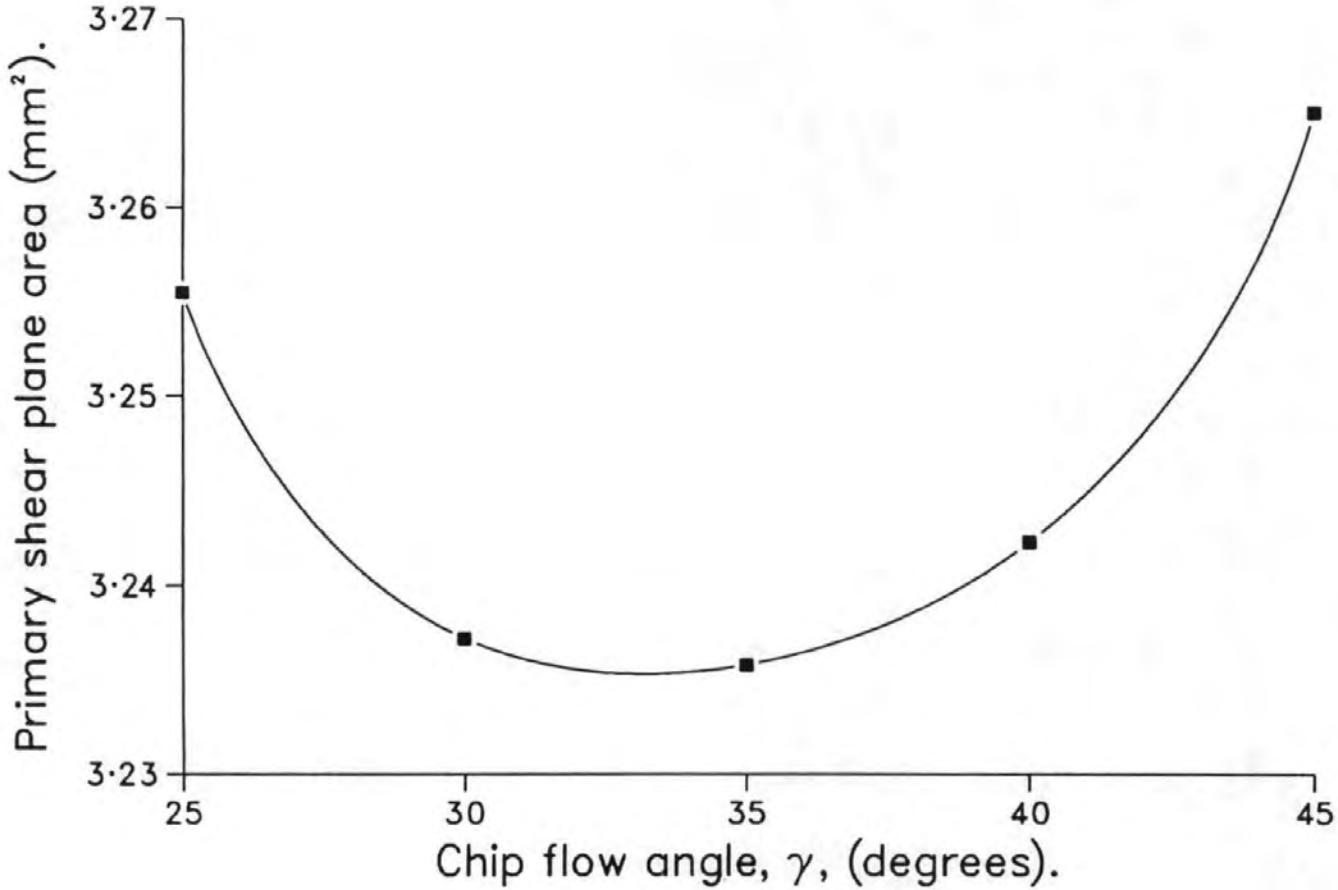

Figure 4.2 Variation Primary Shear Plane Area With Chip Flow Angle

coefficient at the chip tool contact, frictional force varies with normal force, which is proportional to primary shear plane area). For this reason the energetic benefits obtained by adopting this value for chip flow angle are considerable.

The results set out in table 4.3 and illustrated in figure 4.3 were obtained using the minimum global pathlength model. Comparative experimental results were obtained using an untreated tool. All values for chip flow angle are given in degrees.

Table 4.3.

Chip Flow Angles Predicted Using The MGP Model.

Feedrate (mm/rev)	Gamma Exp'tal	Gamma Theory
0.2	54.8	59.0
0.4	48.2	52.25
0.6	41.7	46.75
0.8	35.9	40.75
1.0	33.7	33.0
1.2	29.9	25.75

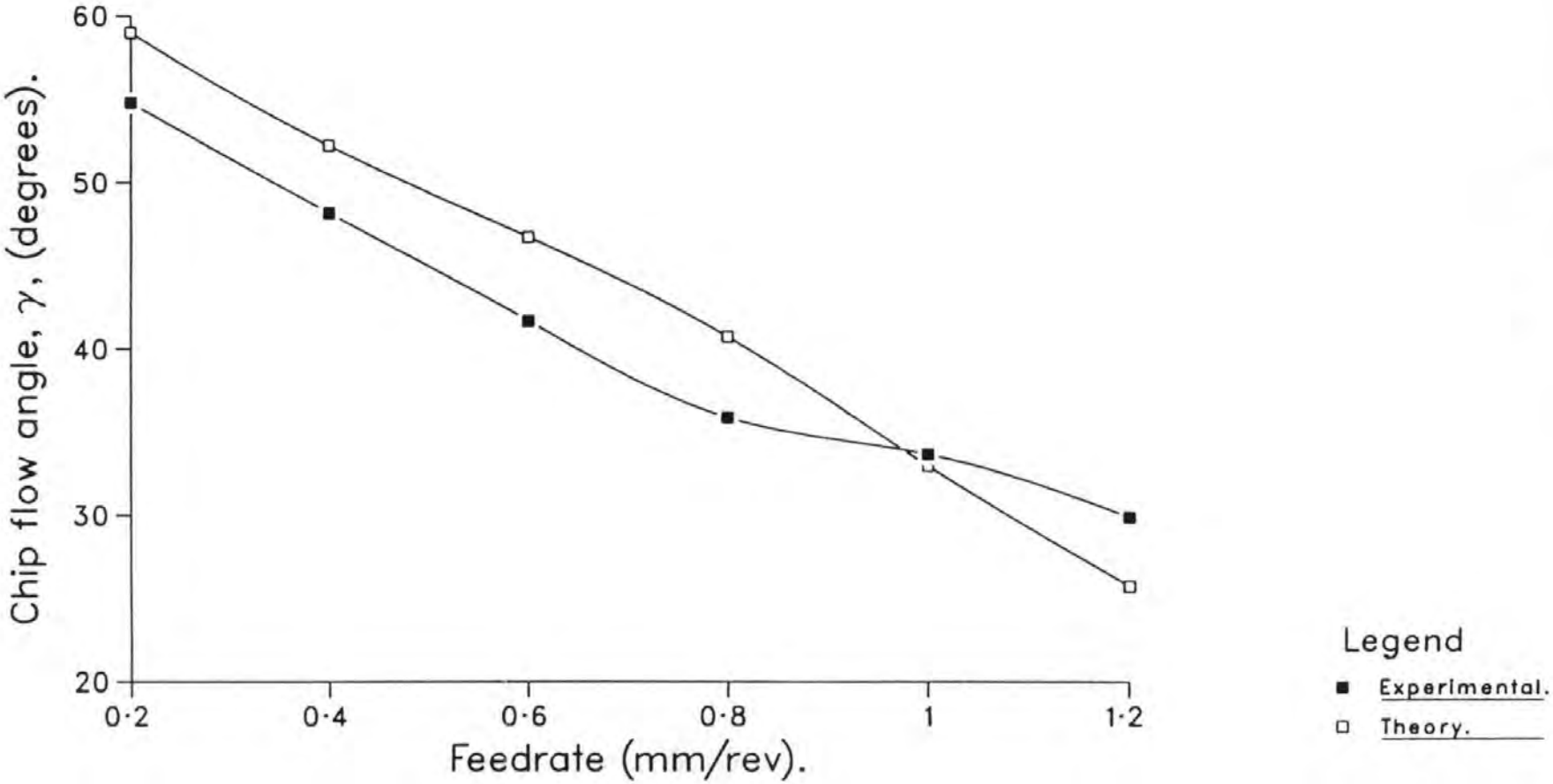

Figure 4.3 Variation In Chip Flow Angle With Feedrate.

(Minimum Global Pathlength Model).

4.3.2.1 Validity Of Results.

The minimum global pathlength model produces accurate predictions of chip flow angle for all combinations of depth of cut and feedrate modelled in this study.

The minimum global pathlength model predicts the chip flow angle satisfying a minimum energy condition. i.e. primary shear occurs in a plane of minimum area (the plane of maximum shear stress), corresponding to a particular chip flow angle. This predicted chip flow angle is found to be in good agreement with the chip flow angle determined experimentally. Predicted values for chip flow angles may be determined in this way for any toolnose geometry for which a similar analysis is performed.

It seems likely that the deviation (due to edge effect shear) of predicted values from those determined experimentally at high feedrates may not limit the use of this model. When the feedrate is greater than the depth of cut (see figure 4.3.), the bulk of primary shear will occur following the edge effect mechanism. As the feedrate becomes much greater than the depth of cut, the chip flow angle minimising the primary shear plane area will tend towards zero. It may be that a chip flow angle minimising the edge effect shear plane area may be determined using the MGP approach, and used to predict bulk chip flow angle where feedrate is greater than depth of cut.

The author suggests this as a topic for future work.

4.4 The Effect Of Nitriding On Chip Flow Angle.

Some evidence of variation in the chip flow angle with nitriding time was found in the experimental data. This is illustrated in figure 4.4. The chip flow angle is evaluated as $\gamma = \tan\ (Fl/Fr)$. The spread of values demonstrates little variation with feedrate. This suggests that the spread is not due to minor chip formation, because the proportion of material forming the minor chip varies with feedrate. (See section 2.10.2.1).

The corresponding variations in radial and longitudinal components of frictional force (figures 4.5 and 4.6) show the variation with nitriding time to be almost entirely limited to the longitudinal component. The cause of the variation in chip flow angle with nitriding time is discussed below. However, it is not clear why little variation in the radial component is observed.

Three possible causes for variation in chip flow angle with nitriding time are described in the following sections:-

(i) A modified minimum energy condition.

(ii) Variation in built up edge stability around the toolnose.

(iii) Through hardening and immediate blunting of the cutting edge.

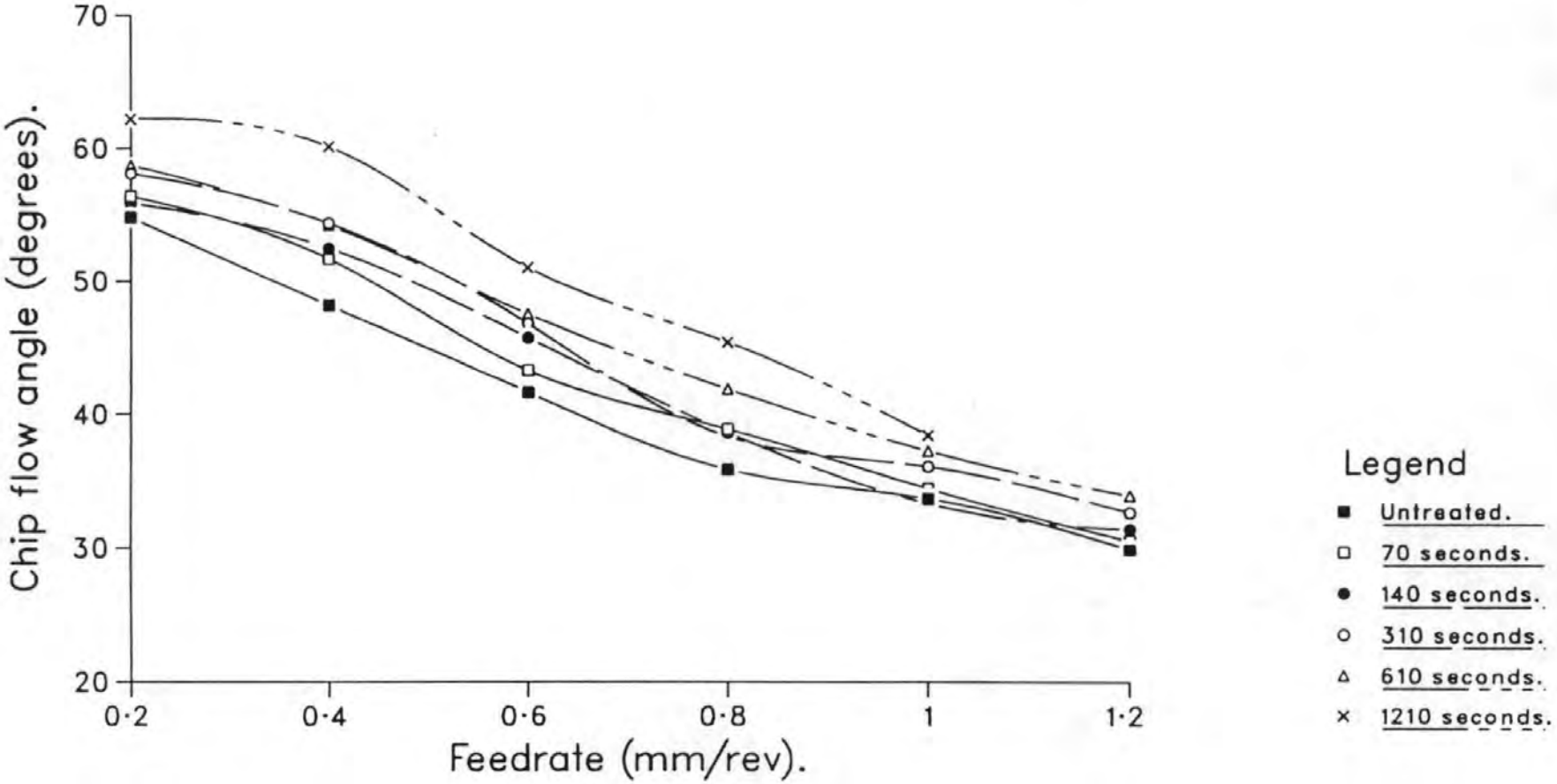

Figure 4.4 Variation In Chip Flow Angle With Feedrate.

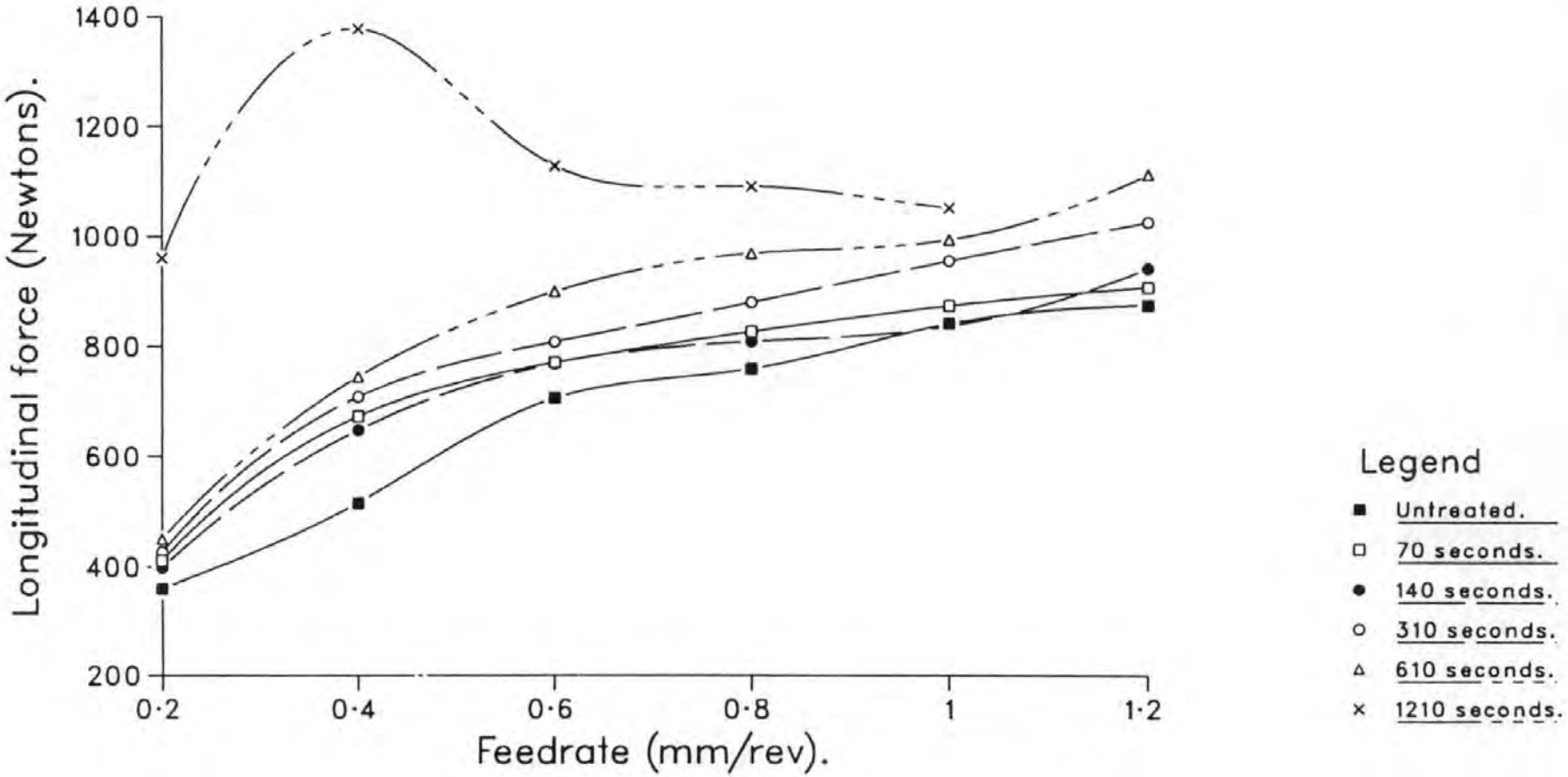

Figure 4.5 Variation In Longitudinal Force With Feedrate.

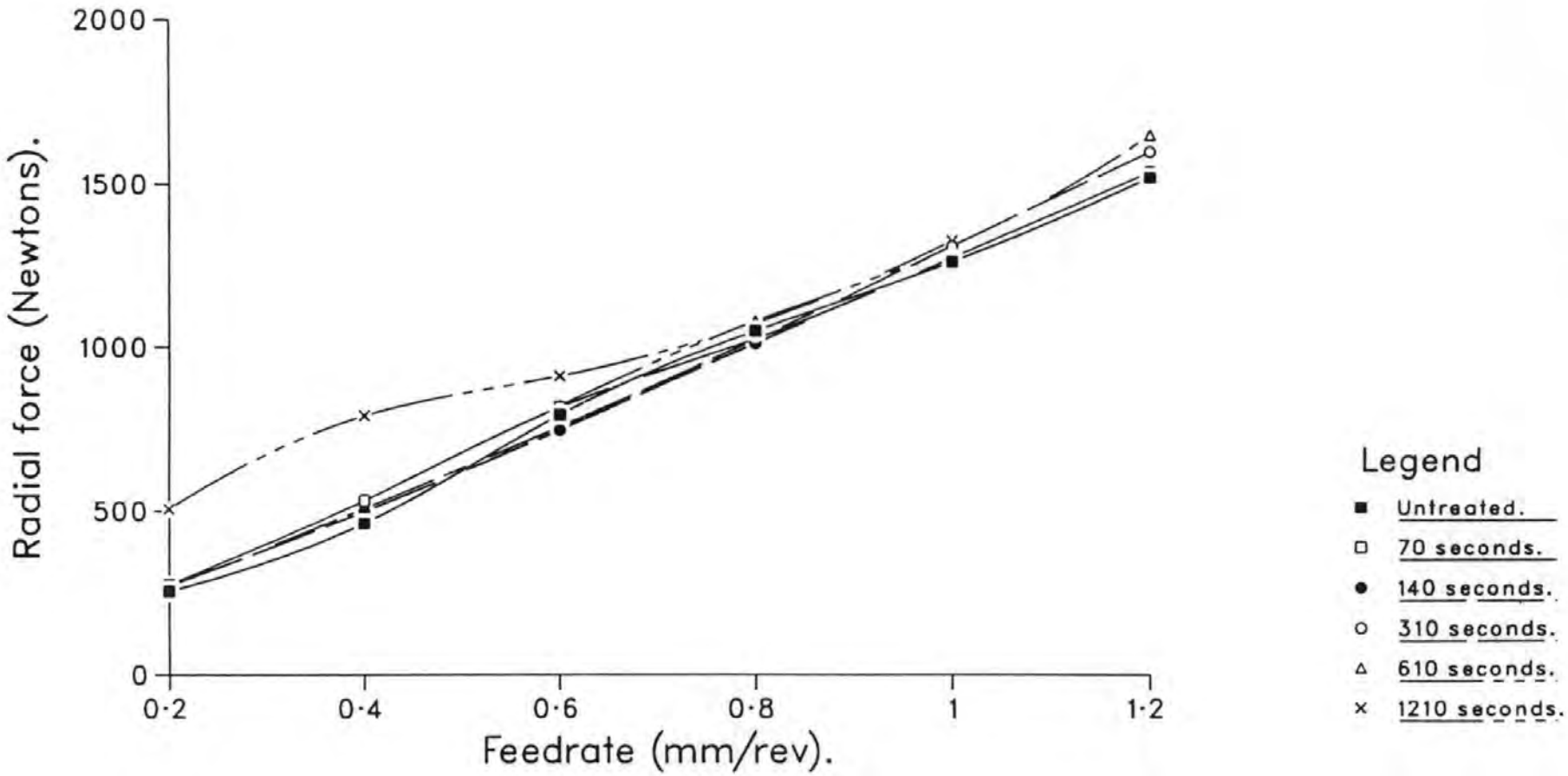

Figure 4.6 Variation In Radial Force With Feedrate.

It is not clear what contribution any one of these mechanisms makes to the overall effect observed experimentally, and for this reason all are described below.

4.4.1 Modification Of The Minimum Energy Condition.

From appendix 2 it is clear that an increase in cutting force will accompany any deviation in gamma from gamma min. Such a deviation might be caused by variation in frictional coefficient with feedrate (figure 4.7).

Lower effective feedrates are found at high theta values (figures 4.8, 4.9). At low feedrates nitrided tools exhibit a slight increase in frictional coefficient (see figure 4.7). Two factors may be responsible for the variation in frictional force with feedrate.

The first is variation in normal pressure with feedrate. To a first approximation, for constant tool geometry, it may be assumed that the area of the tool rake face over which the normal force is exerted is directly proportional to the product of feedrate and depth of cut. Relative normal pressure in the chip tool contact zone was calculated as normal force (determined experimentally) per undeformed chip cross sectional area. Figure 4.10 indicates that slightly higher normal

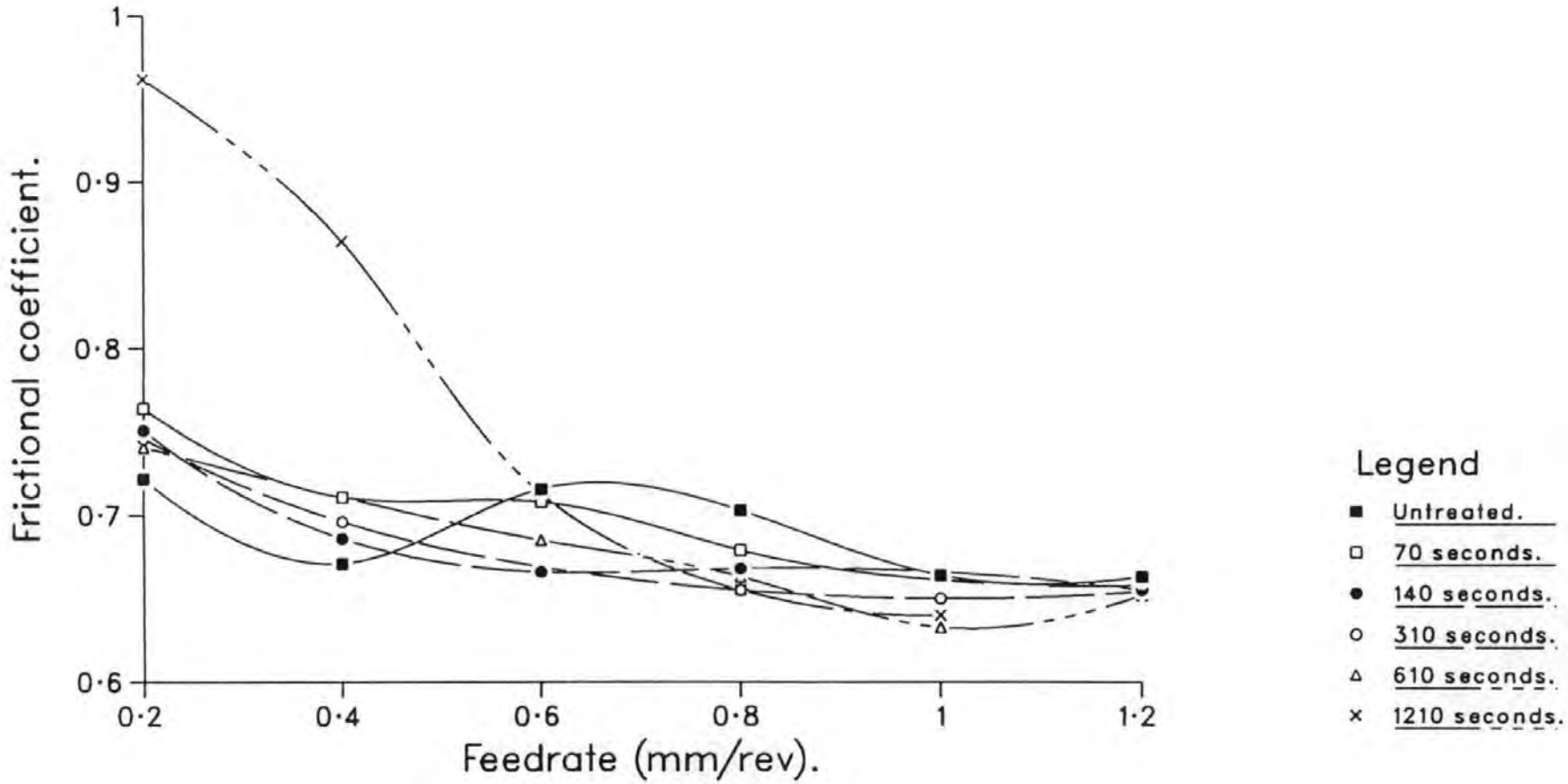

Figure 4.7 Variation In Frictional Coefficient With Feedrate.

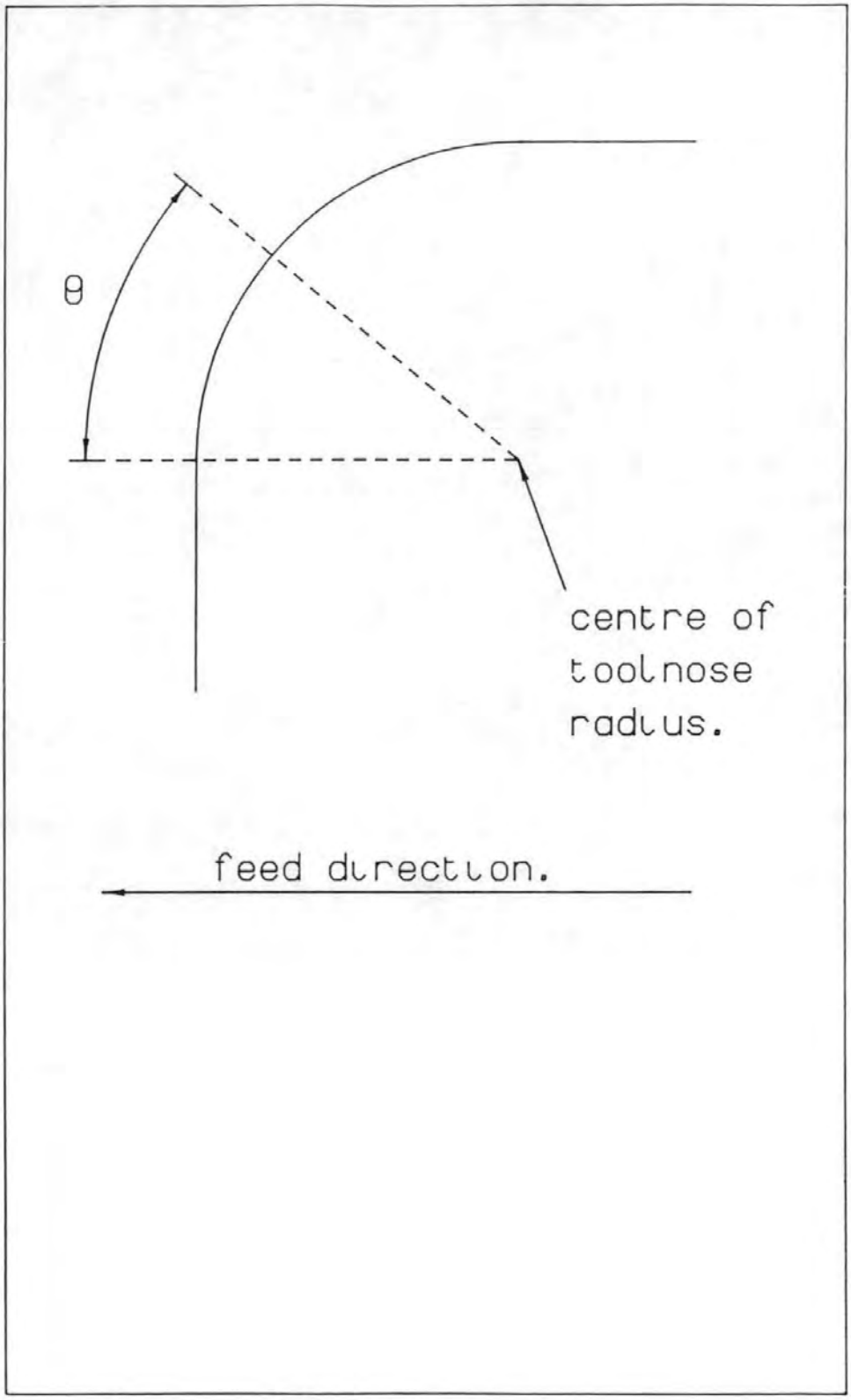

Figure 4.8 Definition Of Theta.

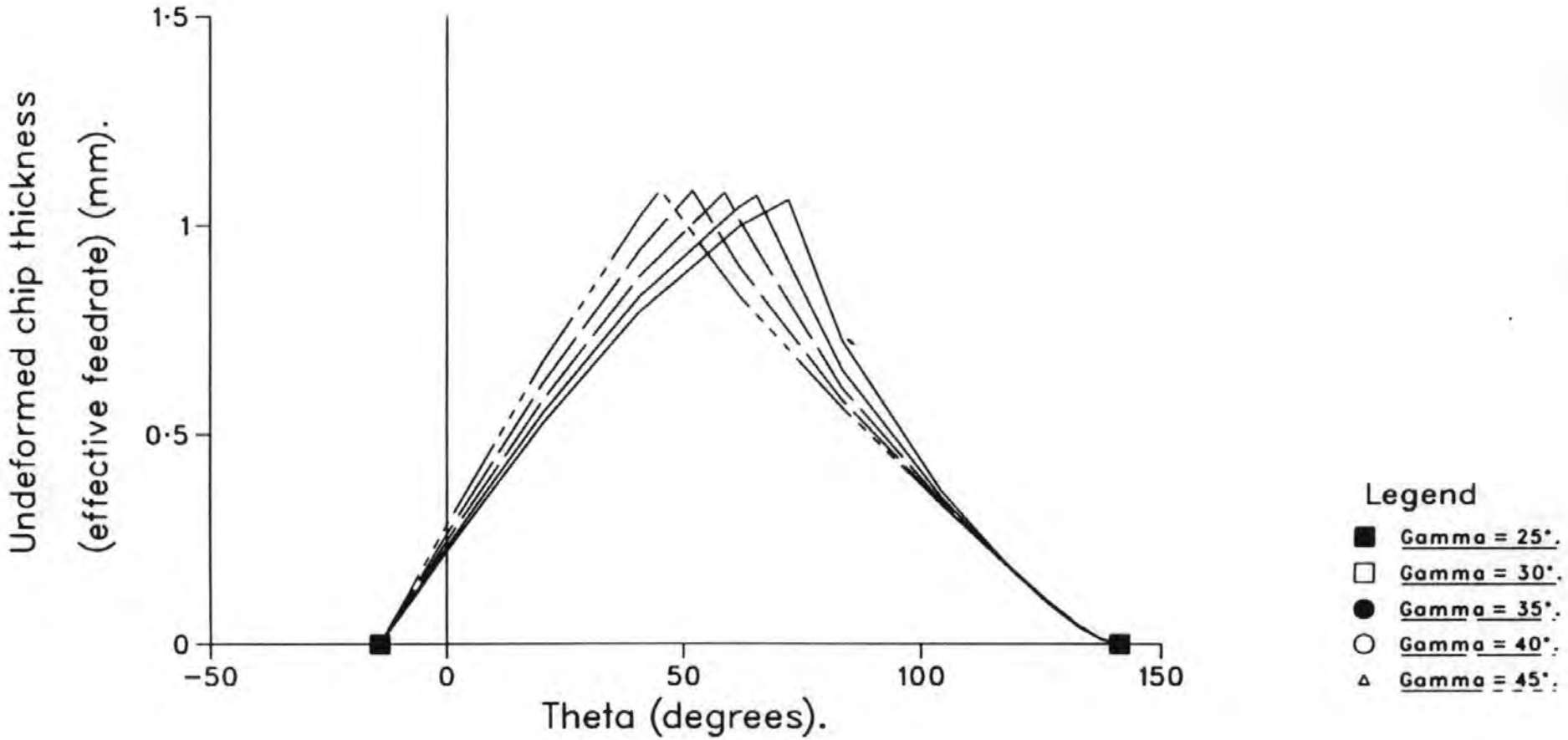

Figure 4.9 Variation In Undeformed Chip Thickness Around The Toolnose.

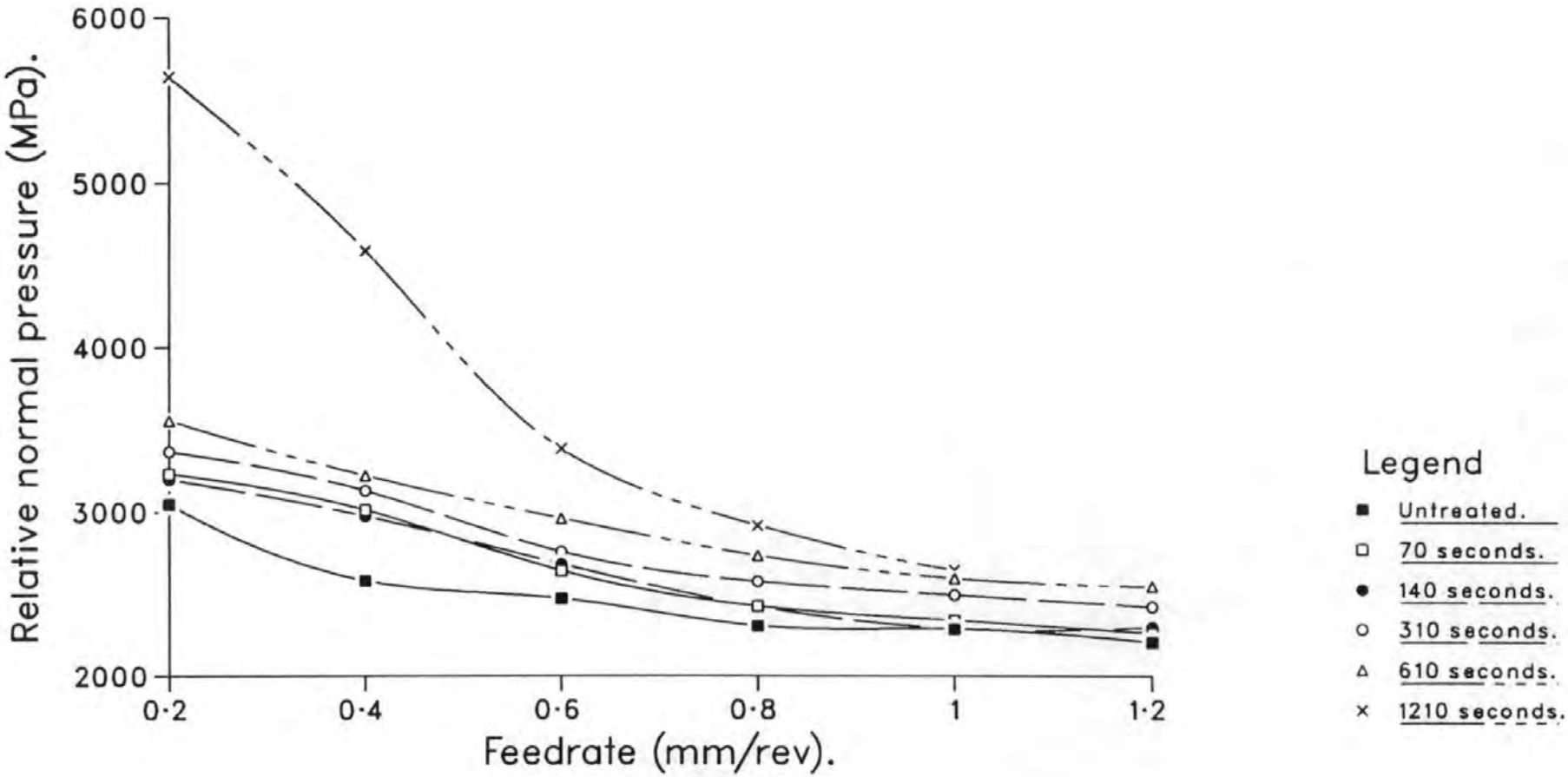

Figure 4.10 Variation In Relative Normal Pressure With Feedrate

pressures are experienced over the chip / tool contact area at lower feeds.

The second factor is the finite cutting edge radius present on the tool. Even after minimal use, some blunting of the edge will occur. For the very low undeformed chip thickness found at high values of theta this will cause a reduction in the primary shear angle.

Graphs of the variation in undeformed chip thickness with theta for a range of chip flow angles (see figure 4.9) were obtained during the development of the minimum global pathlength model. At high values of theta, undeformed chip thickness is reduced to below 0.2 mm, and the trend towards higher frictional coefficient might be expected to continue. Thus the primary shear angle in this region is reduced and the primary shear plane length is increased. More power is required to operate the shear mechanism per unit undeformed chip thickness in the high theta region of the shear system. The value of gamma satisfying the minimum energy condition is modified by the increased energetic benefits of minimising undeformed chip thickness at high values of theta. Figure 4.9, drawn using data from the MGP model (section 2.10.3), illustrates that a higher chip flow angle will reduce undeformed chip thickness in the high theta region. (i.e. in the region where $\theta > 70$ degrees in figure 4.9).

Although undeformed chip thickness in the low theta region is increased, work done per unit undeformed chip thickness under these conditions is relatively small, (due to the lower frictional coefficient and higher primary shear angle), and an overall reduction in work done is achieved. It is to be expected that this effect, causing higher chip flow angle, will be most pronounced for tools exhibiting higher values for frictional coefficient at lower feedrates (i.e. nitrided tools (figure 4.7)). This is found to be the case (figure 4.4).

4.4.2 Variation In Built Up Edge Stability.

Data from simultaneously recorded cutting forces and tool temperatures indicates that nitriding tends to inhibit the formation of a built up edge (see section 4.8). Thus, in the case of an untreated tool, the built up edge is to be expected to extend further around the nose, increasing the effective rake angle at high theta (figure 4.8). The corresponding increase in primary shear angle and chip velocity in this region will tend to reduce the chip flow angle. Although there are some supporting indications in the data, further investigation is required in order to determine the magnitude of this effect.

4.4.3 Through Hardening Of The Cutting Edge.

The trend in chip flow angle with nitriding process time may be considered in terms of the failure of the cutting edge due to through hardening. At a feedrate of 0.2 mm/rev the tool treated for 1210 seconds exhibits a frictional coefficient of 0.96. It is likely that the anomolously high longitudinal force component measured in this case is due to either contact between the tool flank face and the workpiece and bulge formation in the work material, or to poor surface condition, possibly high roughness of the tool.

In general, failure of the through hardened cutting edge is expected to occur at lower undeformed chip thickness, which are found at high theta (figure 4.9), due to the higher normal pressure found under these conditions (figure 4.10). The effective rake angle over the damaged cutting edge will be more negative, causing a reduction in primary shear angle in this region. Thus a velocity gradient is imposed across the chip, with higher velocities towards the outside of the cut tending to cause the chip to flow in a more longitudinal direction.

This is consistent with the slight general trend towards increasing chip flow angle with increasing nitriding process time determined experimentally and illustrated in figure 4.4.

4.4.4 Contribution Of Effects.

From the information available it cannot be stated categorically that one of these above mechanisms is responsible for the variation in chip flow angle with nitriding time. It is likely that more than one mechanism is involved.

4.5 Stick - Slip Behaviour.

The critical frictional force required to cause sticking in the chip / tool contact zone was obtained using a value for yield shear stress and an approximate chip / tool contact area. To simplify the problem, the component of frictional force caused by sliding contact outside the sticking contact zone was ignored. The contact area within which the bulk of the frictional work was done was evaluated after [56] as

$$A = (F.DOC) + \frac{(F.DOC)}{\mu.\tan\phi}$$

where A = Area of significant chip / tool contact.

F = Feedrate.

DOC = Depth of cut.

μ = Coefficient of friction

ϕ = Primary shear angle.

The primary shear angle was estimated as twenty degrees from measurements of chip mass per unit length. Attempts were also

made to estimate primary shear angle from chip microstructure, but the value obtained was found to vary across the thickness of the chip, so the bulk value given from the mass was believed to be better.

The yield shear stress was calculated from the shear plane area and the primary shear force. In addition these calculations were made over a range of surface speeds, in order to determine the strain rate sensitivity of the yield shear stress. Primary shear plane area was calculated using the global pathlength integrals derived in section 2.10.3. Primary shear force was determined as

$$Fs = Fn.\cos\phi - Ff.\sin\phi$$

where Fn = Force acting normal to the tool rake face.

Ff = Frictional force exerted on the tool by the chip

Shear velocity was determined as

$$Vs = S/\cos\phi$$

where S = surface speed.

Results determined using this method are shown in table 4.4.

Table 4.4

Variation In Work Material Yield Shear Stress With Strain Rate.

S (m/min)	Vs (m/min)	Aps (mm^2)	Fs (Newtons)	τs MPa
20	22.07	1.36	689	505.4
30	33.10	1.36	658	484.1
40	44.14	1.36	658	484.8
50	55.17	1.36	638	470.5
60	66.20	1.36	630	465.9
70	77.24	1.36	615	454.0

Figure 4.11 illustrates the variation in yield shear stress with shear velocity. A linear relationship was assumed, and a least squares fit calculated, giving:

$$\tau s = 520 \text{ MPa} - 0.84 \text{ Vs}$$

where Vs = shear velocity (m/min).

The above values for BS EN8 are intermediate between values of 480 MPa for 0.13 % carbon steel [57] and 700 MPa for AISI 4340 (BS EN 24) [58], as is to be expected. Having derived an expression for the yield shear stress in terms of shear velocity, and an appropriate value for the chip tool contact area, the critical frictional force above which secondary shear and sticking in the chip tool contact zone will occur may be calculated as

$$Ffc = \tau s . A$$

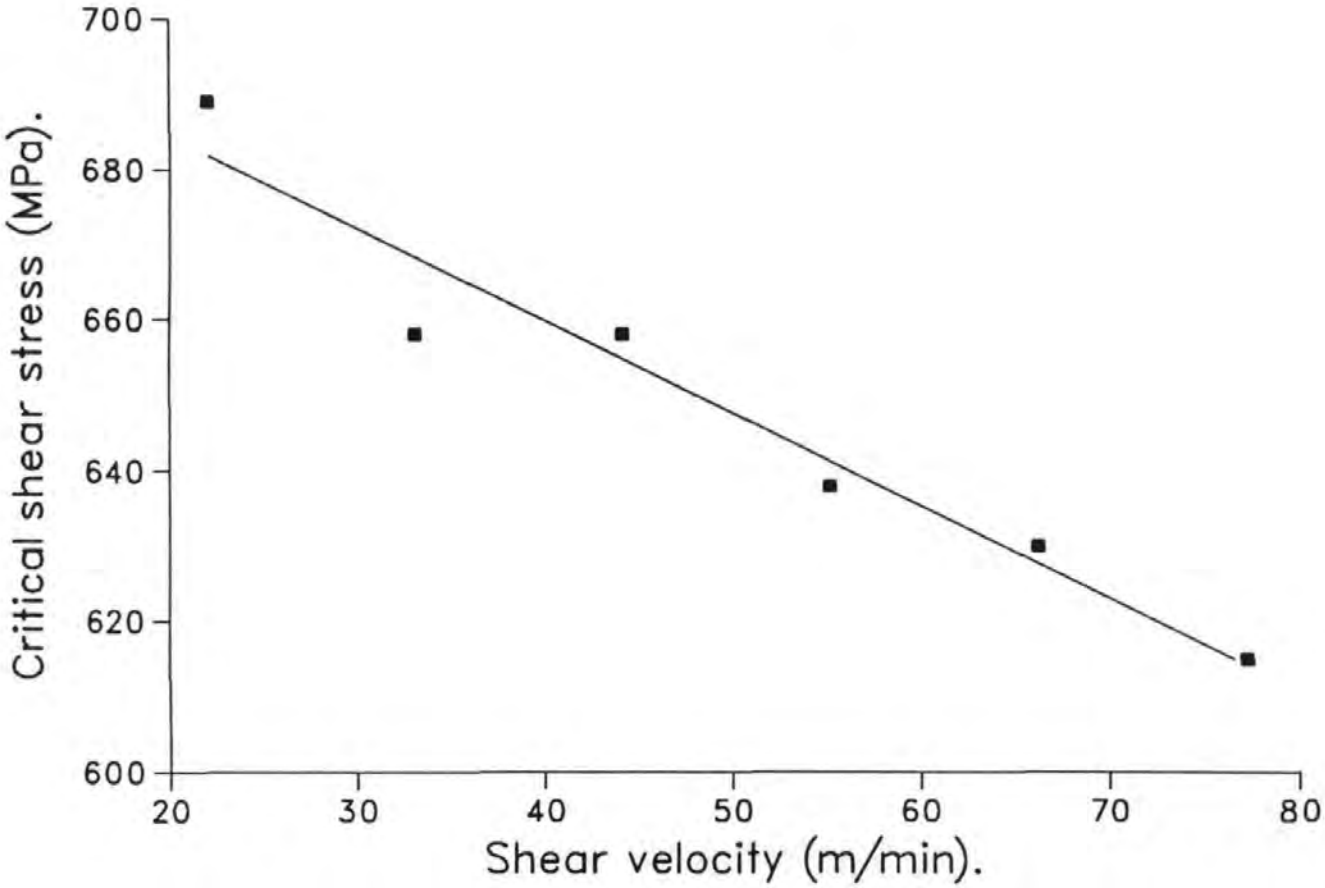

Figure 4.11 Variation Critical Shear Stress With Shear Velocity.

where A = area of significant chip / tool contact.

Results from such a calculation are set out in table 4.5, for a feedrate of 0.5 mm/rev and a depth of cut of 1.0 mm.

Table 4.5.

Variation In Critical Frictional Force With Cutting Speed.

S (m/min)	Vc (m/min)	τ_s (MPa)	Ffc (Newtons)
20	9.33	511.5	639
30	13.99	507.5	634
40	18.65	503.6	630
50	23.32	499.7	625
60	27.98	495.7	620
70	32.64	491.8	615

Figure 4.12 illustrates the variation in frictional force with cutting speed determined experimentally, with reference to the predicted critical frictional force, Ffc. Frictional forces above the critical value indicate that secondary shear is occurring in the chip rather than slipping at the chip / tool interface. The benefits of promoting sliding in the chip tool contact zone are discussed in section 4.8.

Similar tables may be drawn up for other feedrates.

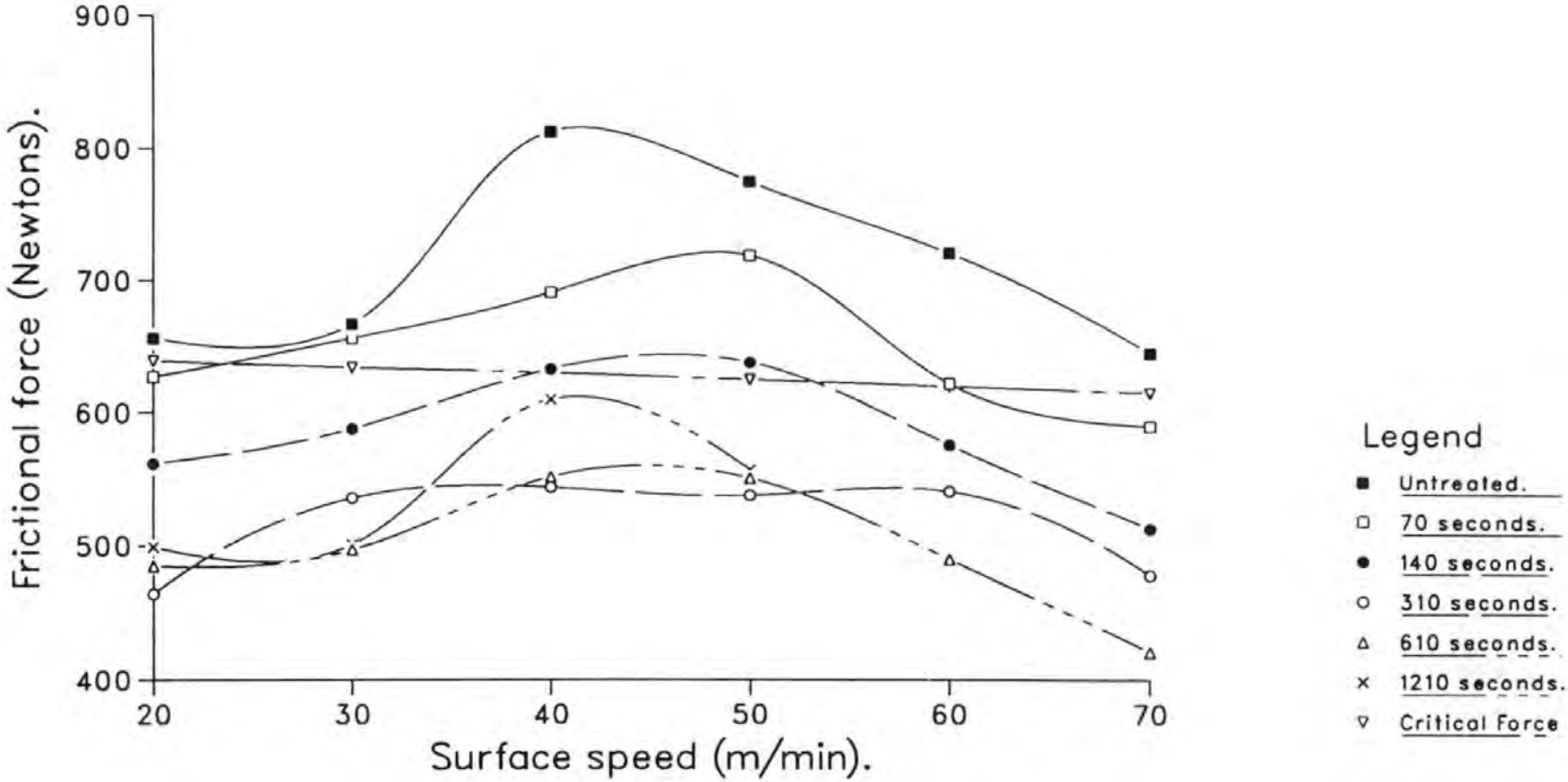

Figure 4.12. Variation In Frictional Force With Surface Speed.

4.6 Built Up Edge (BUE) Stability.

Recorded force data contained fluctuations caused by the formation and loss of a built up edge on the rake face of the tool. (Electrical noise in the dynamometer amplifiers was attenuated to much lower levels using passive low pass filters).

It was expected that the standard deviation of these fluctuations from the mean value of force measured would correlate with built up edge stability. However, no systematic variation in standard deviation with nitriding time or any other test variable was observed

The frequency of formation and loss of the built up edge was established by examination of the underside of the chip, and was found to be higher (up to 40 Hz) than the frequency at which force data was sampled (3.3 Hz). Increasing the rate at which the force data was sampled would enable the frequency of the formation / loss events to determined, and the variation in cutting forces during these events to be measured. This is suggested as a topic for future work.

4.7 Surface Effects.

Two sources of data concerning the performance of the nitrided surface itself are discussed. These are the frictional coefficient, and the change in tool temperature per frictional work per second.

4.7.1 Frictional Coefficient.

From figure 4.7, no single trend in frictional coefficient is apparent. It appears, however, that at feeds in excess of 0.6 mm per revolution nitriding confers a slight reduction in frictional coefficient. Due to the short duration of the tests it is improbable that this is a result of clearance face contact, since flank wear will have remained a negligibly small factor. The tool nitrided for 70 seconds exhibits a trend in frictional behaviour similar to the untreated tool at low feedrates. Feedrates of between 0.6 and 1.0 mm per revolution seem favourable for nitrided tools. Nitriding times of between two and ten minutes all lead to a slight reduction in frictional coefficient. (figure 4.7).

4.7.2 Benefits Conferred By Nitriding.

Figures 4.13 and 4.14 demonstrate similar variations in frictional force and frictional coefficient over a range of

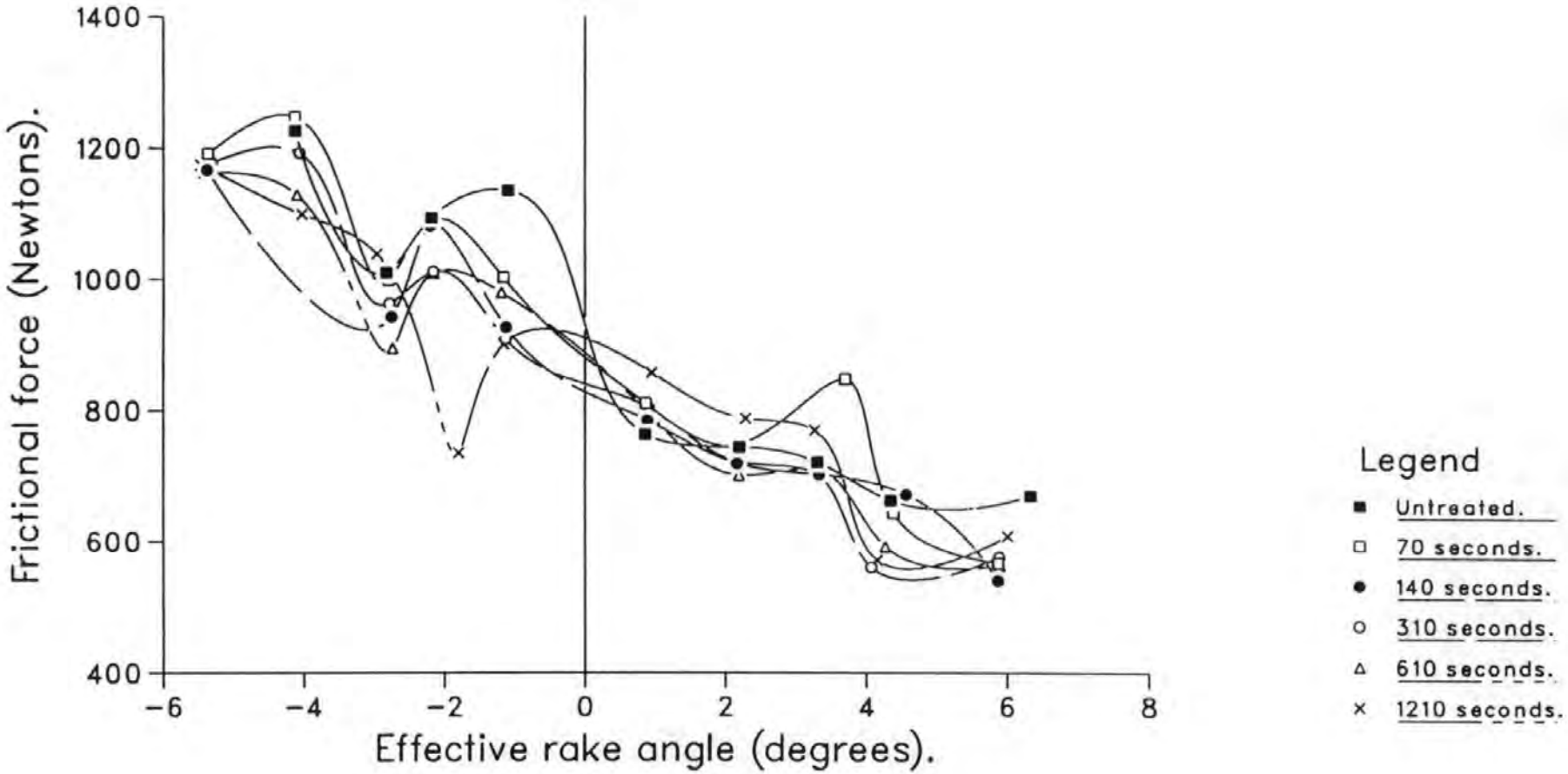

Figure 4.13 Variation In Frictional Force With Rake Angle.

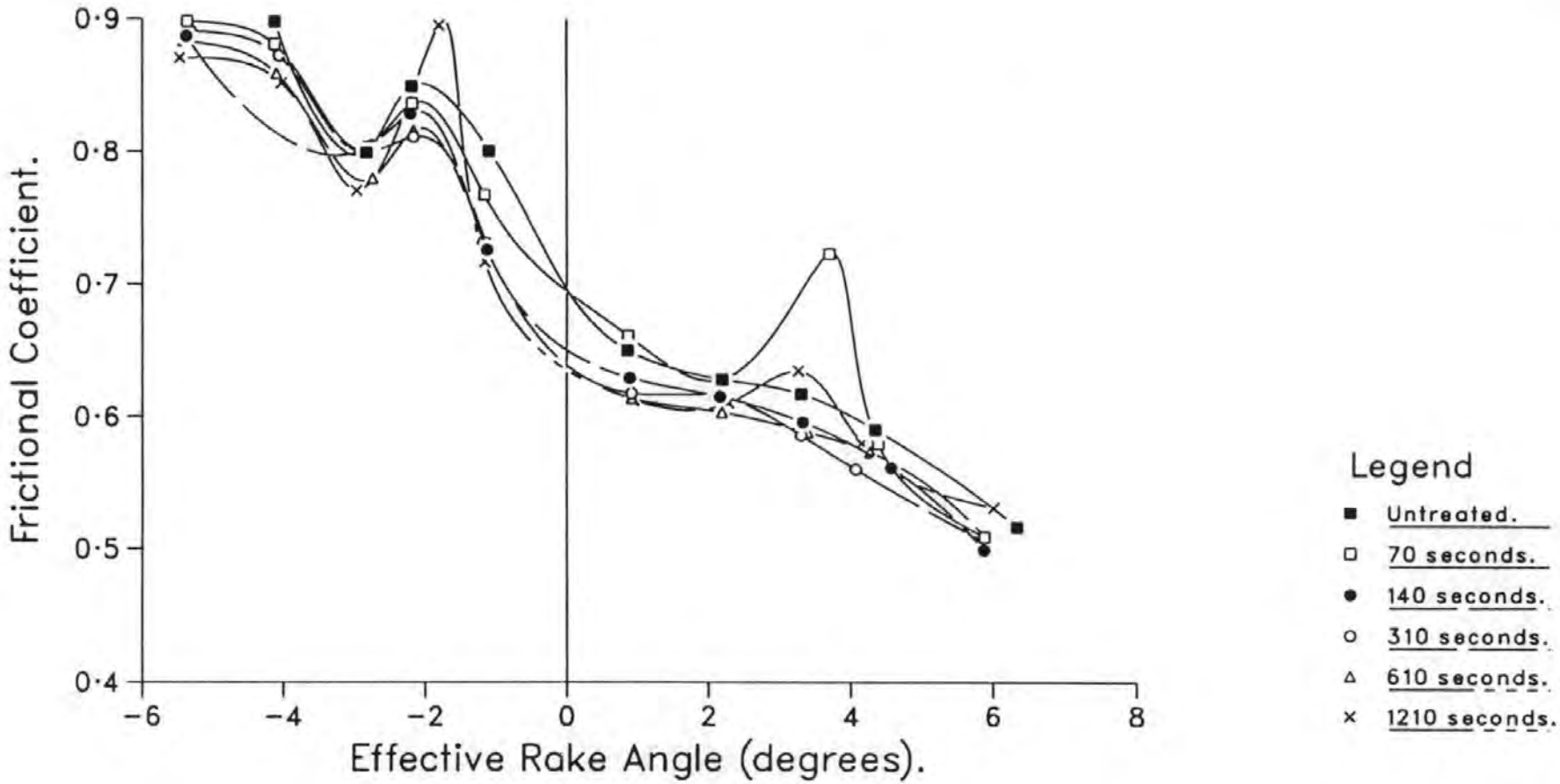

Figure 4.14 Variation Frictional Coefficient With Rake Angle.

rake angles. A general trend towards lower values at more positive rake angles is consistent with a reduction in sticking contact in the chip tool contact zone with lower normal loads. However, figure 4.15 shows little systematic reduction in normal force with increasing rake angle. The anomalously high frictional coefficient recorded for tools nitrided for 1210 seconds at -4 degrees rake angle is not considered representative of nitrided tips, and is possibly caused by edge embrittlement, leading to premature failure of the cutting edge.

Frictional coefficient is slightly decreased due to nitriding across the entire range of rake angles within which the tests were conducted. Tools nitrided for 70 and 1210 seconds exhibit higher frictional coefficients across a limited range of rake angles. It is likely that these detrimental effects are related to process factors. Process times of between two and ten minutes produce optimum improvements in cutting tool performance.

The coefficient of friction is a widely applicable parameter. Higher frictional forces may accompany increased normal forces resulting from some peculiarity in the shear mechanism under a certain set of cutting conditions. Frictional coefficient is largely unaffected by system geometry, and it is likely that variations in frictional coefficient accurately reflect the performance of the surface in loaded sliding contact.

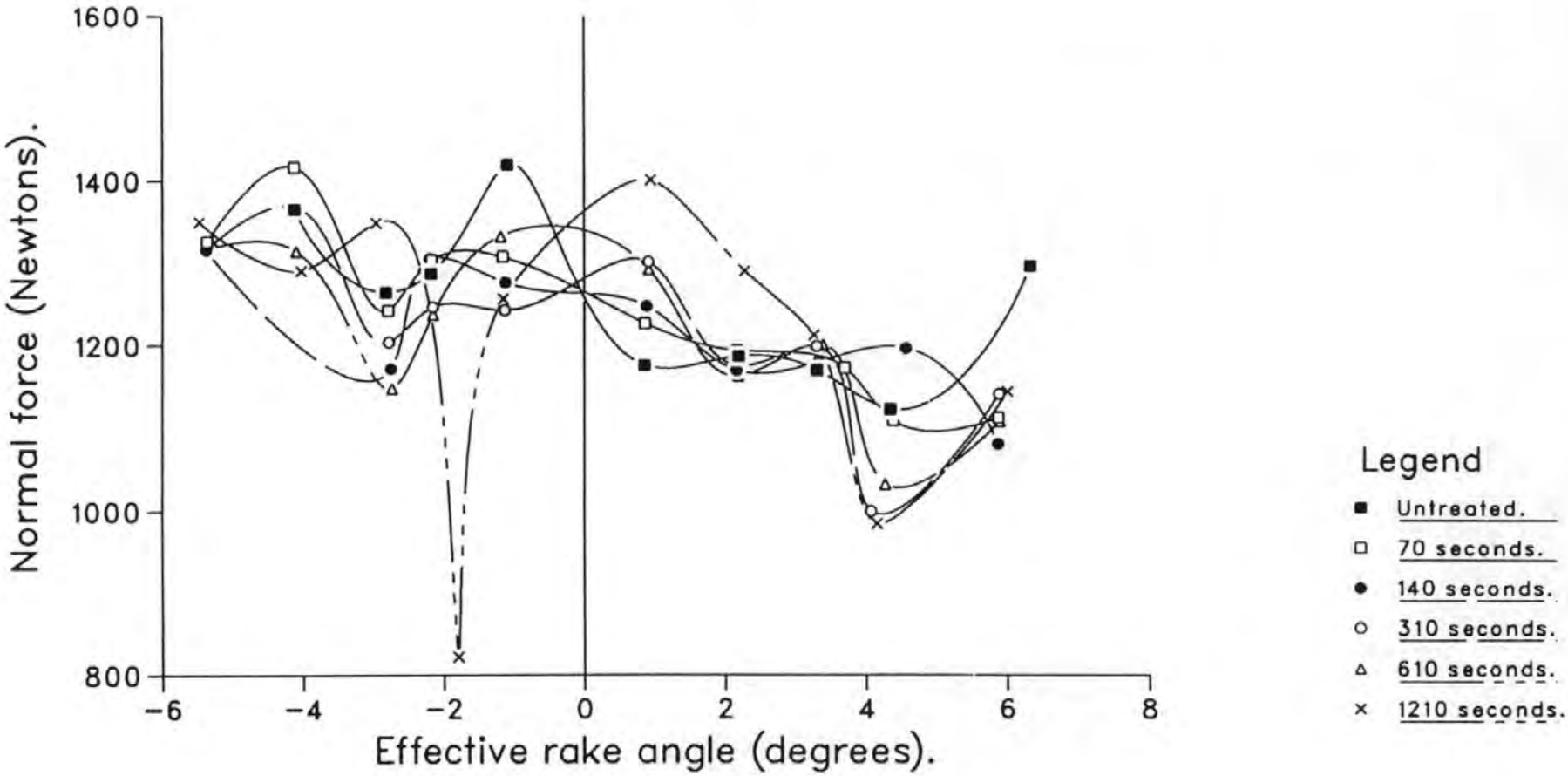

Figure 4.15 Variation In Normal Force With Rake Angle.

4.7.3 Frictional Coefficient.

A significant reduction in frictional coefficient for nitrided tools is observed in figure 4.16 at surface speeds in excess of 40 m/min. Tools treated for 310 seconds exhibit the lowest values of frictional coefficient, and the most significant reduction in frictional force at surface speeds between 40 and 50 m/min (figure 4.12).

4.8 Tool Performance.

The notion of a transition from sticking to sliding in the chip tool contact zone below a critical frictional force, Ffc, was introduced in section 4.5. The performance of the rake surface of a cutting tool may also be assessed using temperature change per frictional work done per second, or, assuming the variation in chip velocity with nitriding to be negligible, in terms of the tool temperature change per frictional force.

Nitriding has been found to modify the primary shear mechanism, causing variation in the chip flow angle and thus in the frictional force experienced by the tool. Thus temperature change per frictional force provides more information on the performance of the tool rake face than temperature change or frictional force alone.

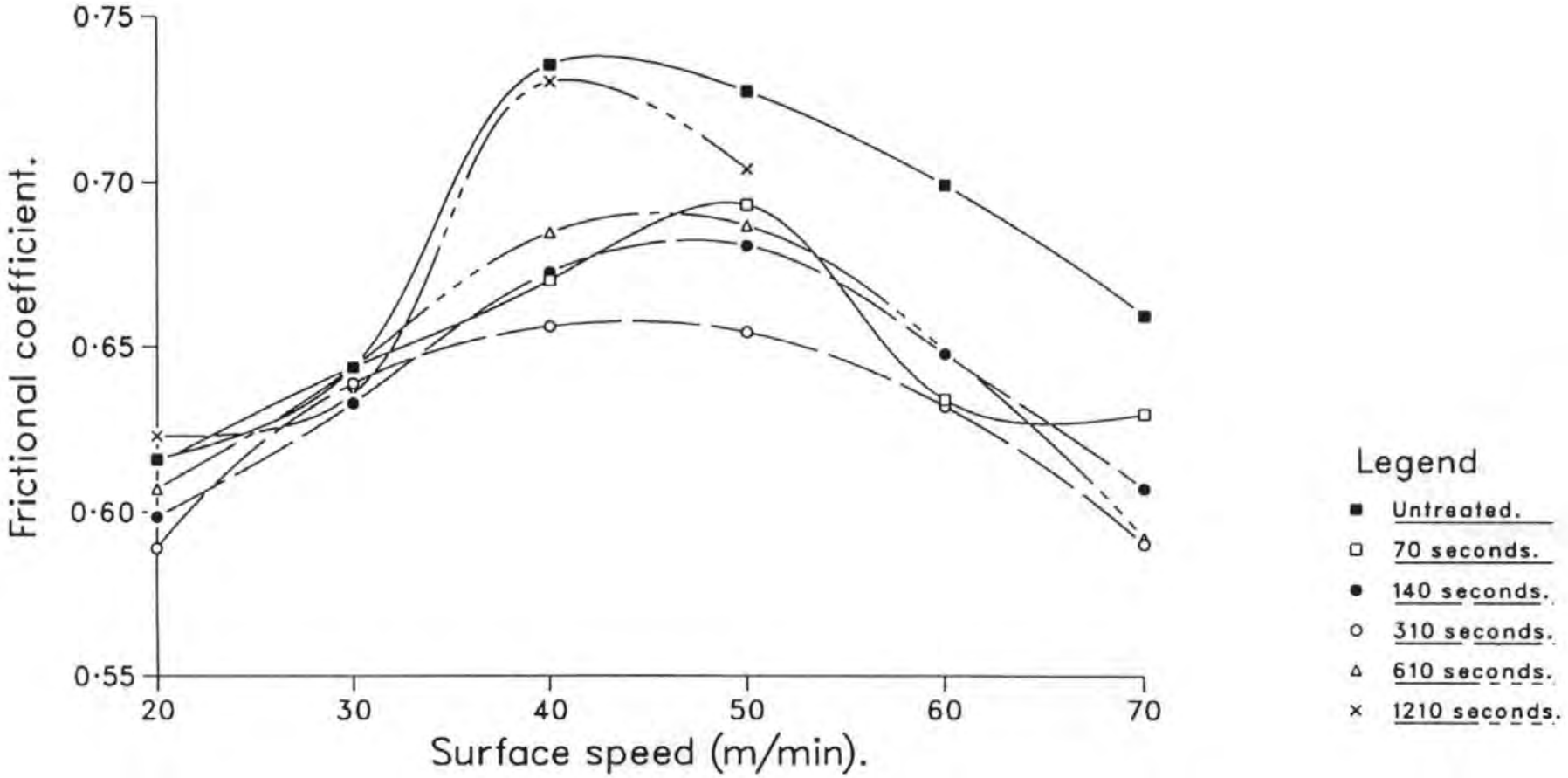

Figure 4.16 Variation In Frictional Coefficient With Surface Speed.

Figure 4.17 shows the variation in temperature change per frictional force with surface speed. Below the critical secondary shear stress, sliding occurs in the chip / tool contact zone. Heat transfer between the sliding chip and tool might be expected to be less efficient than heat transfer between a siezed chip and tool. Thus less of the heat liberated in primary shear will be lost from the chip into the tool through a sliding contact. The protection afforded to the tool by the built up edge in distancing the site of secondary shear from the tool rake face is minimal. The built up edge functions as a thin section of highly conductive material, metallurgically bonded to both the secondary shear site, and the tool rake face. The transition from sticking to slipping in the chip tool contact zone may be observed as maxima in figure 4.17.

The untreated tool maintains sticking contact with the chip at all surface speeds, and the graph of T/Ff versus surface speed is a strait line with a gradient reflecting the rising surface speed. However, for the case of a tool treated for 140 seconds, the maximum present in figure 4.17 at a surface speed of 40 m/min is associated with the transition from sticking to sliding behaviour as the secondary shear stress falls below the critical value.

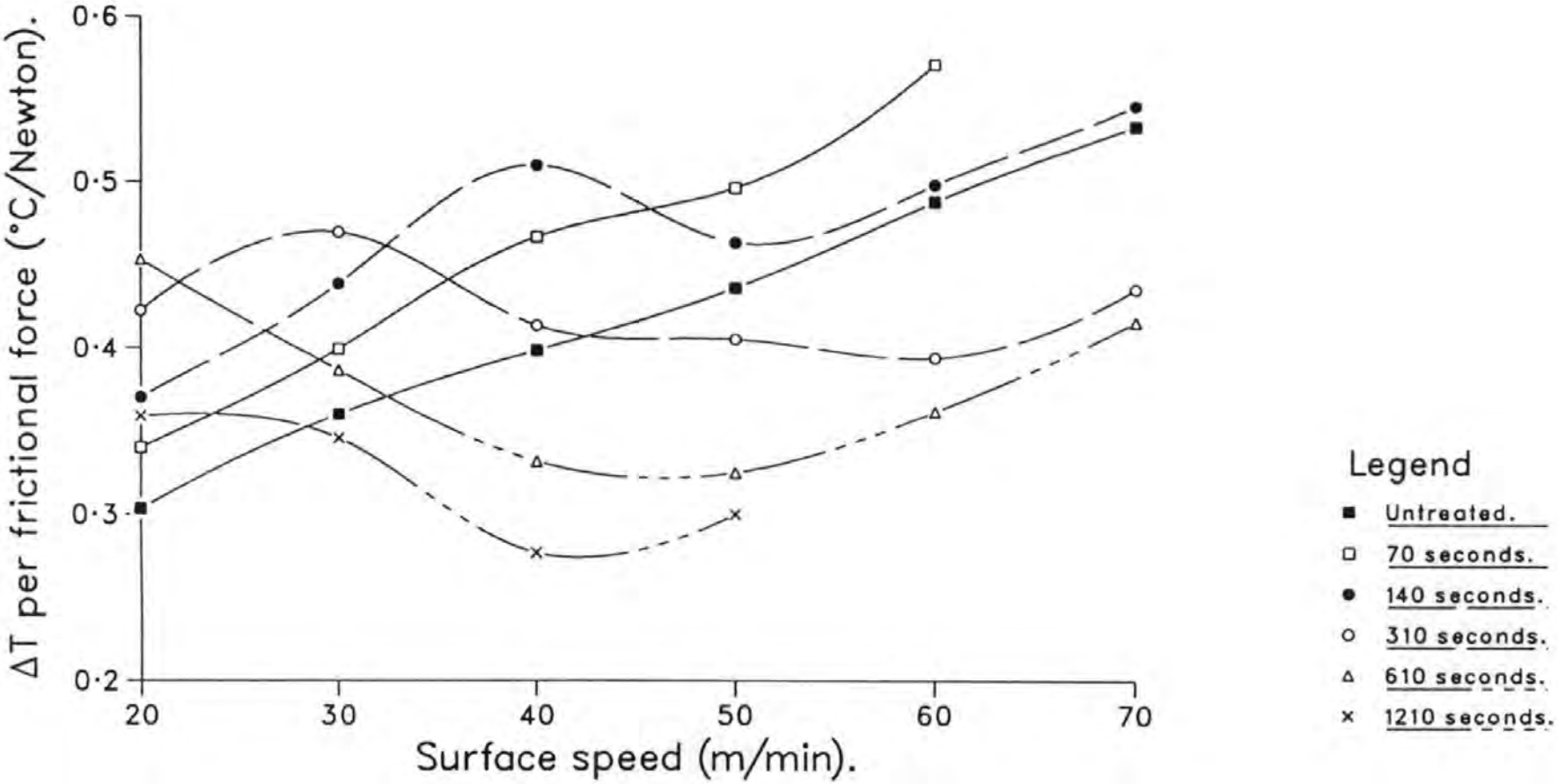

Figure 4.17 Variation In Temperature Change Per Frictional Force With Surface Speed.

For the case of a tool treated for 310 seconds, this maximum occurs at a surface speed of 30 m/min, and for treatment times in excess of 610 seconds, sliding contact is observed at surface speeds greater than 20 m/min.

The main factor contributing to the trend towards sliding rather than stick slip contact at higher surface speeds is the reduction in critical shear stress with temperature.

The reduction in tool temperature resulting from the promotion of sliding in the chip tool contact zone is illustrated in figure 4.18.

4.9 Summary Of Results.

Nitriding increases the variation in frictional coefficient with normal pressure. This is associated with an increase in the value of cutting forces and normal pressures. Nitriding reduces frictional coefficient when cutting at higher feedrates. Nitriding reduces frictional heating of the tool. It is likely that this is due to a reduction in the extent of sticking in the chip tool contact zone.

The minimum global pathlength model produces accurate predictions of chip flow angles.

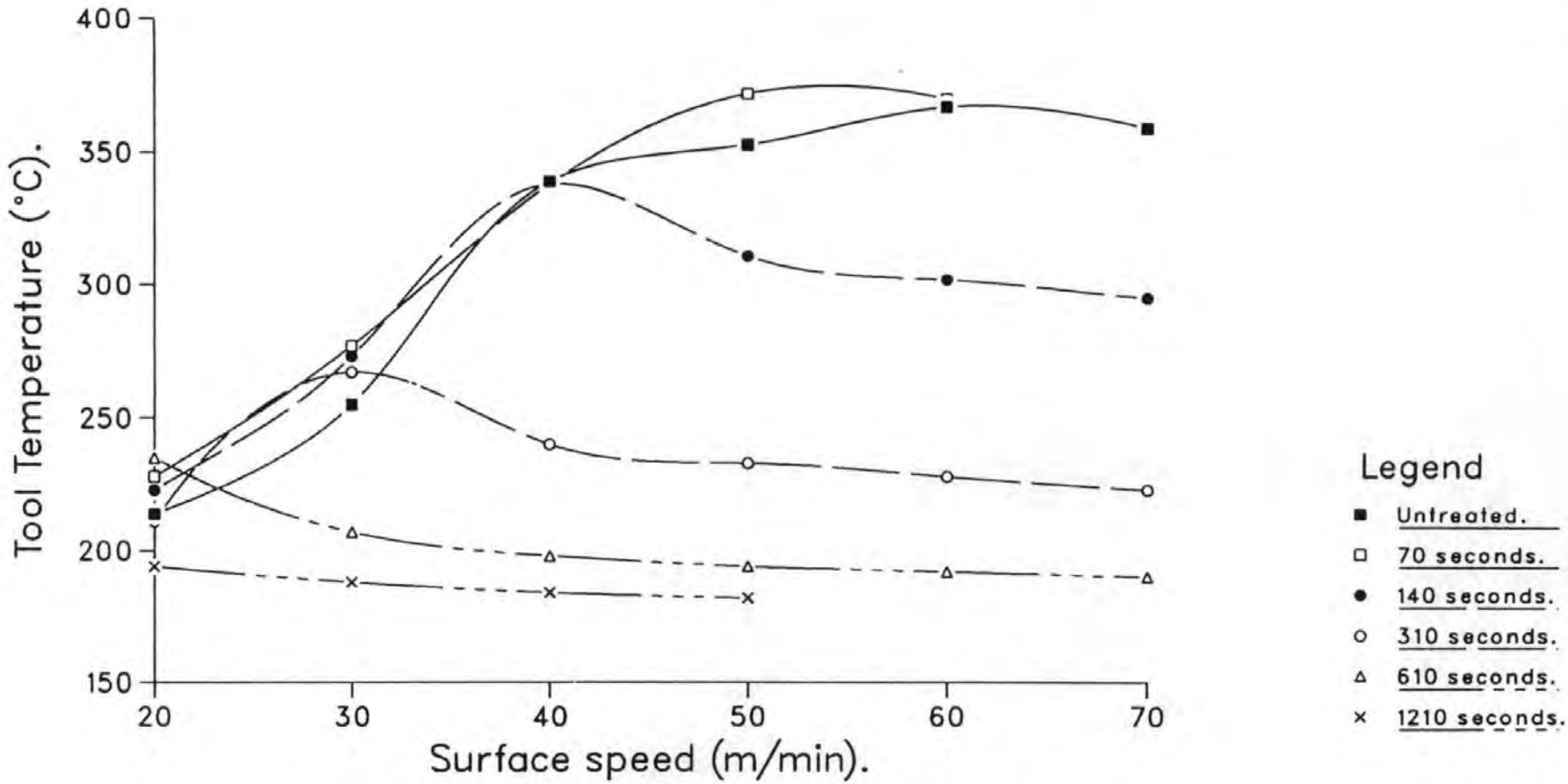

Figure 4.18 Variation In Tool Temperature With Surface Speed.

Chapter 5. Modelling Tool Temperature.

5.1 Introduction.

Considerable effort was applied to the development of a finite element model of the temperature distribution within the cutting tool. The temperature distribution was found to be extremely sensitive to boundary conditions, and determining these is a complex problem in itself. Both heat transfer between the insert and tool holder and the heat input into the tool through the chip / tool contact must be determined in order to describe heat flow in the insert accurately.

The heat transfer coefficient at the boundary between the insert and tool holder is dependent on a number of factors.

(i) Contact pressure.
(ii) Insert surface roughness.
(iii) Insert surface hardness.
(iv) Tool holder surface roughness.
(v) Tool holder surface hardness.

Roughness and hardness may be determined, but the contact pressure is less easily evaluated. The insert is clamped into the tool holder towards the corner most distant from the cutting corner, and it is likely that some variation in

clamping force is present across the boundary. In addition, the face of the tool holder to which the insert is clamped contains a depression which further complicates the analysis of heat flow.

The sensitivity of the tool temperature to heat transfer between the insert and tool holder is further discussed in appendix 7. In view of the uncertainty associated with this boundary condition, the author suggests that a wrought tool is better suited to heat transfer analysis.

The proportion of cutting energy entering the tool must also be determined. A method for evaluating this has been suggested by Blok [74]. However for a tool with a nose radius, some variation in primary shear angle and normal pressure around the engaged cutting edge is expected. The corresponding variations in frictional heating have not been investigated. In addition, data from infra red thermography (see section 5.2.3.1) indicates that significant heating occurs in the sliding zone towards the end of the chip / tool contact. Thus from the data available, it is not possible to model heat flow in the tool with sufficient accuracy to determine surface temperature distributions. For these reasons extensive use of a finite element model was abandoned, although the finite element method was used to provide some qualitative information.

5.1.1. Modelling Tool Heat Input.

The theoretical value for heat input to the tool was refined throughout the heat transfer modelling program. First approximations, based on experimentally determined frictional forces and chip velocities indicated that around 600 Watts was liberated in the chip tool contact zone. A first refinement was to assume that equal proportions of this energy entered the chip and tool, suggesting a tool heat input of around 300 Watts.

A second approach to the problem was to evaluate the heat input required to produce tool temperatures in the model similar to those recorded experimentally. This suggested values of the order of 40 Watts.

Uncertainty surrounding the heat transfer charactaristics of the boundary between the insert and the tool holder (see appendix 6) prevented evaluation of the tool heat input using the latter technique.

The several values for heat input used for aspects of the work (see section 5.3.2, appendix 4 and appendix 6) indicate the stage to which the heat transfer modelling had progressed. Information obtained from these sections is qualitative, and the trends and patterns discussed independent of the applied flux.

5.2 Experimental Investigations Of Temperature Distributions.

In service tool temperature distributions were initially investigated experimentally to qualify results expected from thermal modelling. This modelling requires further work before valid results may be obtained. Method and results from related experimental studies are presented below for the information of other workers in similar fields.

Two techniques were employed: temperature sensitive pigments and implanted thermocouples.

5.2.1 Temperature Sensitive Pigments.

Temperature sensitive paints were used to record temperature contours within the tool at a distance of 0.5 mm from the rake face. A temperature distribution obtained using the cutting conditions described in table 3.6 is shown in figure 5.1.

The effect of the pigment layer on heat flow in the tool should be considered when evaluating results from this method. This was assessed using a finite element model described in appendix 4.

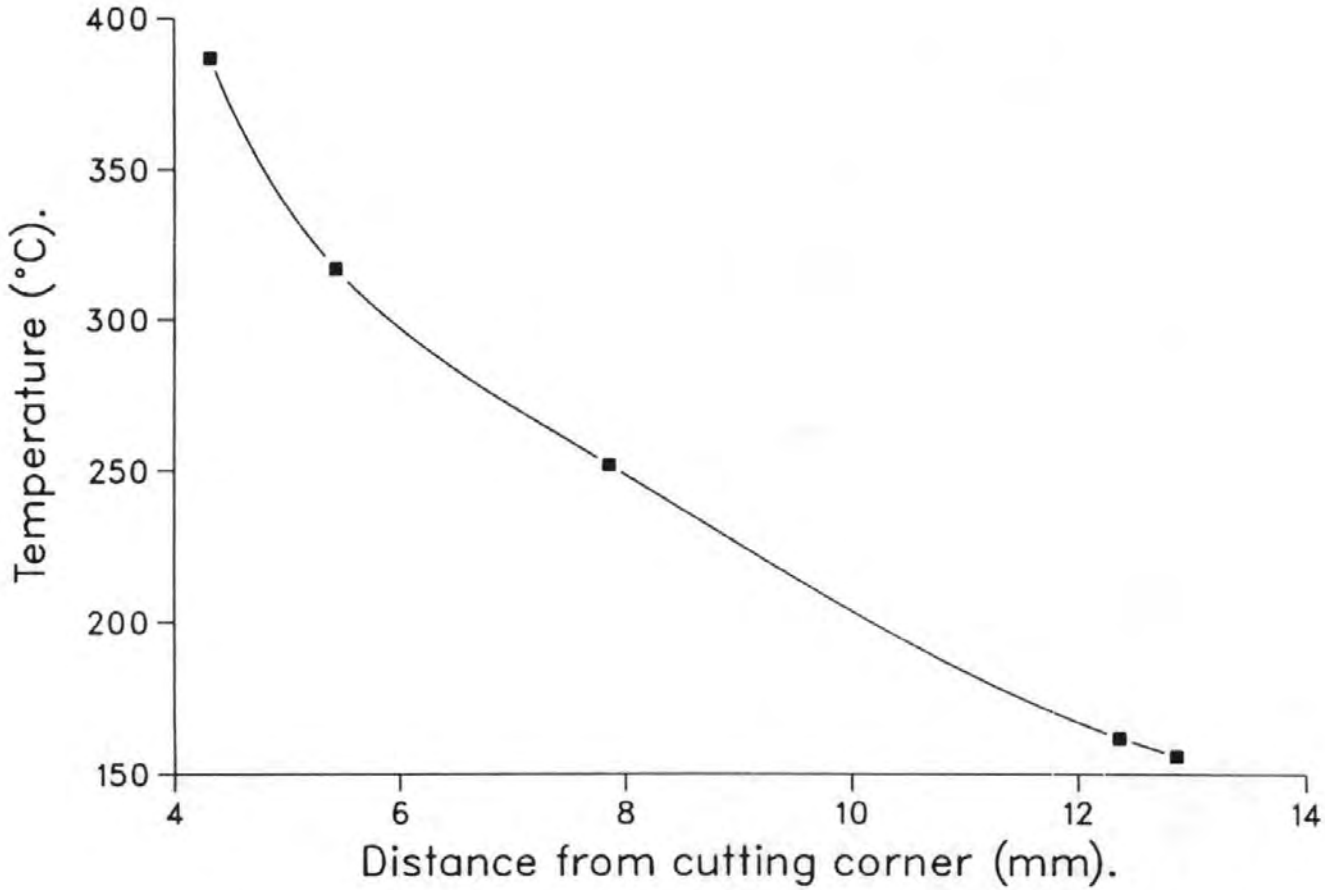

Figure 5.1. Tool Temperature Distribution Determined Using Temperature Sensitive Pigments.

5.2.2 Implanted Thermocouples.

A study using implanted thermocouples was undertaken to elucidate the variation in temperature through the thickness of the tool.

The method for mounting the thermocouple in the insert is described in section 3.3.4.2. The positioning of the thermocouple is illustrated in figure 5.2. A number of cavities were machined into un - nitrided insert tools to a range of depths. These tools were then used to turn medium carbon steel (EN8) on a lathe under the conditions in table 5.1, and mean steady state thermocouple temperatures were recorded.

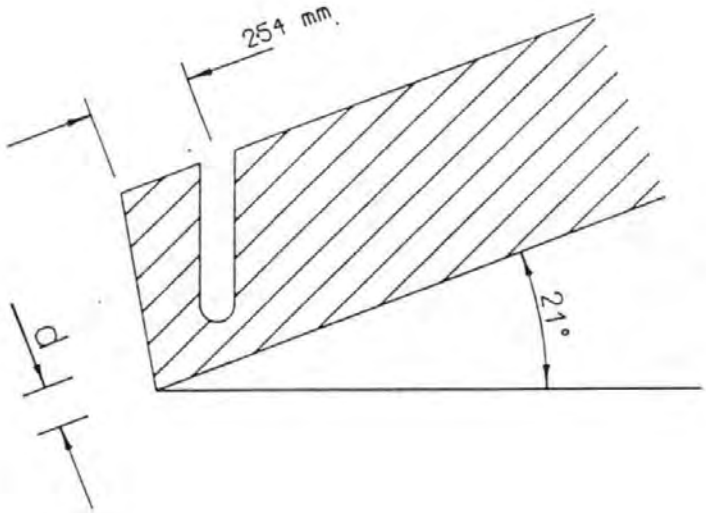

Figure 5.2 Diagonal Section Through An Insert Tool Indicating The Thermocouple Position.

Table 5.1

Test Conditions For Experimental Determination Of Tool Temperature Distribution.

Surface speed	= 20, 30, 40, 50, 60 m/min.
Feed rate	= 0.5 mm/rev.
Depth of cut	= 1 mm.
Side rake angle	= 0 degrees.
End rake angle	= 0 degrees.
Workpiece material	= Medium carbon steel (EN8).

The temperatures shown in table 5.2 and figure 5.3 were obtained.

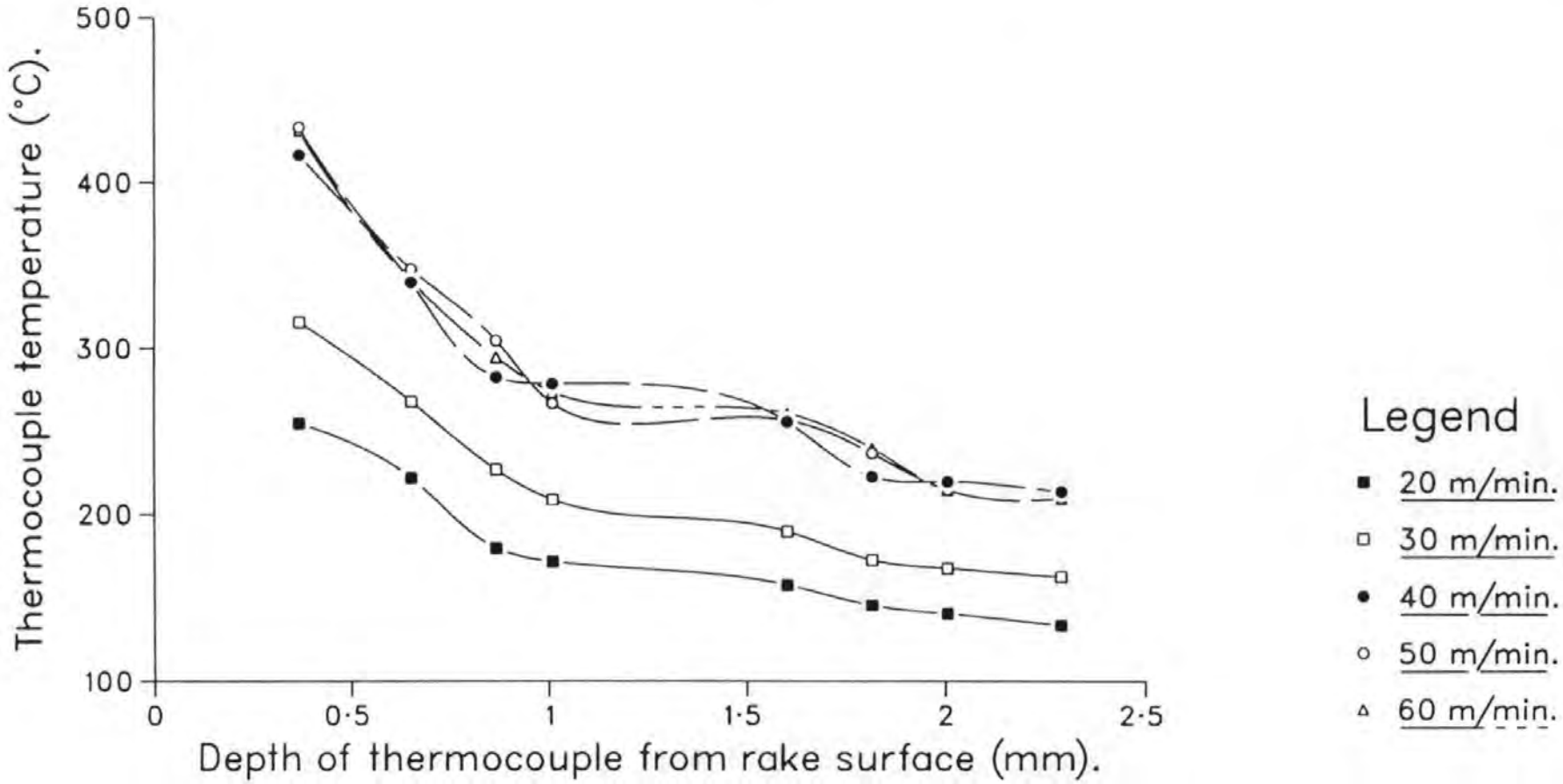

Figure 5.3 Tool Temperature Distributions Determined Using Implanted Thermocouples.

Table 5.2. Measured Tool Temperatures (°C).

Depth from rake face. (mm)	Surface speeds (m/min).				
	20	30	40	50	60
0.368	255	316	417	434	432
0.652	222	268	340	348	341
0.866	180	227	283	305	295
1.008	172	209	279	267	274
1.601	158	190	256	257	261
1.814	146	173	223	237	240
2.004	141	168	220	215	215
2.289	134	163	214	210	210

From figure 5.3, the overall variation in tool temperature with distance from the rake surface appears to be non - linear. However, in the region between 0.368 and 1.01 mm from the surface, the variation is sufficiently linear to justify the extrapolation of surface temperatures using the least squares method.

Surface temperatures evaluated using this method are presented in table 5.3 and figure 5.4.

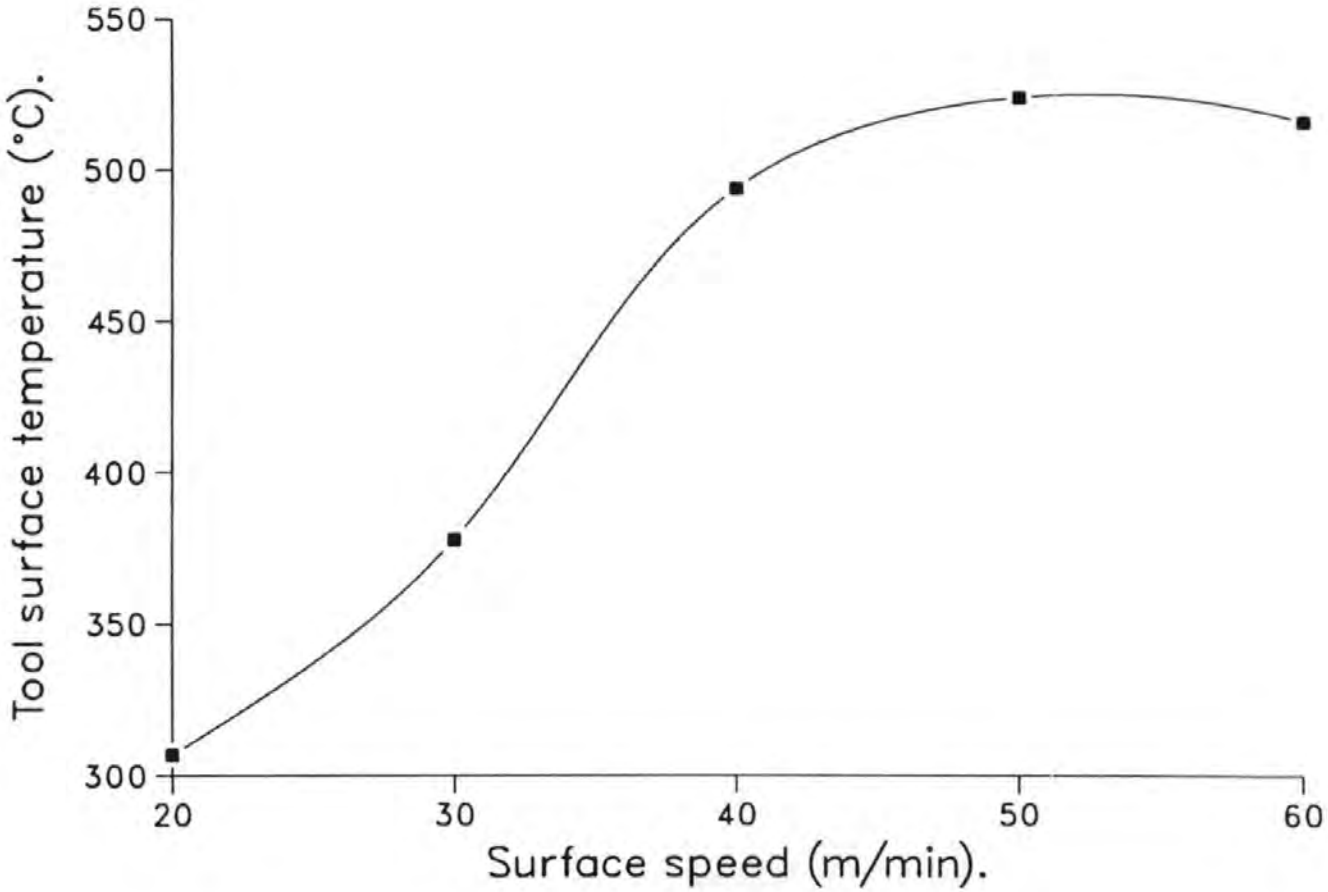

Figure 5.4 Variation In Tool Surface Temperature With Speed.

Table 5.3.

Extrapolated Tool Rake Face Temperatures.

Workpiece Surface Speed. (m/min).	Tool Surface Temperature. (°C).
20	307
30	378
40	494
50	524
60	516

For models developed to describe heat transfer in tools where the boundary conditions are well defined, surface temperature values such as these may be used to evaluate the heat flux entering the tool. Knowledge of cutting forces and primary shear angles may be used to calculate the total flux generated at the chip / tool contact.

The proportion of total flux entering the tool may be determined from these two quantities, and the effect of nitriding on heat transfer at this junction evaluated. The author suggests this as a topic for future work.

5.2.3 Thermography.

Figure 5.5 illustrates a typical temperature distribution at the cutting corner of the rake face determined using infra red thermography.

In service tool temperatures may be evaluated using temperature distributions determined by this method, in conjunction with a transient model of heat flow in the tool. To a first approximation, variation in tool temperature may be assumed to be first order with respect to time. This assertion was verified experimentally, and a time constant of around 3 seconds determined. Thus any error in measuring the time between disengaging the tool from the workpiece and recording a thermograph will introduce considerable inaccuracy in the calculated in service tool temperature value.

Two features of the rake face temperature distributions determined using infra red thermography are of particular interest. The temperature distribution is asymmetric, and the maximum temperature is found to be displaced from the toolnose edge.

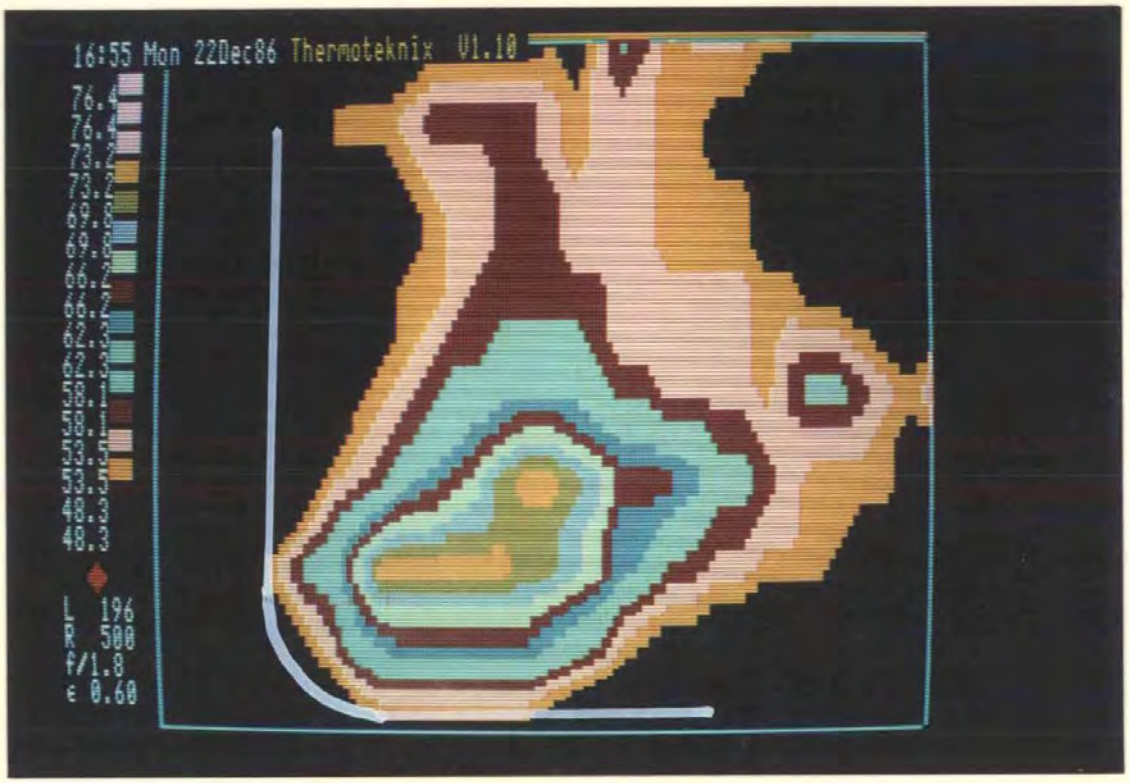

Plan view of rake face plane with toolnose profile (white).

Figure 5.5 Rake Face Temperature Distribution Determined Using Infra Red Thermography.

5.2.3.1 Temperature Distribution Asymmetry.

Taking the region of highest temperature as a central reference, surrounding temperature contours are seen to extend to the upper right of the frame in figure 5.5, following the approximate direction of chip flow. Clearly heating of the tool extends beyond that area of the rake face covered by the undeformed chip, and it is likely that significant heating of the tool is brought about by the sliding passage of the chip.

5.2.3.2 Position Of Maximum Surface Temperature.

In common with results recorded by workers such as Tay et al [56], the maximum rake face surface temperature was found to be displaced from the cutting edge of the tool. This was also a feature of results obtained from finite element work.

5.3 Finite Element Modelling.

Heat flow in the cutting tool was modelled using the finite element (F.E.) method. The underlying theory is well documented, and since this was not modified no description is given here. The packages used to perform the analysis were PAFEC (program for automatic finite element analysis) and PIGS (PAFEC integrated graphics system), both produced by PAFEC Ltd, and supported by a PRIME 9755 supermini computer. Extensive

documentation describing the use of these packages is available, and for this reason their operation is not discussed.

Uncertainty in the boundary conditions of the problem, described in section 5.1 and appendix 7, prevented any meaningful quantitative data being produced. However, some interesting qualitative information was produced, and this is set out below.

5.3.1 Two Dimensional Approximation.

Two dimensional analysis of heat flow in cutting tools has been carried out by Tay et al [56]. For bar turning where feedrate per depth of cut is either much greater or much less than one, a two dimensional heat flow analysis may be performed on some plane within the tool.

In order to model a three dimensional temperature distribution as equivalent to the temperature distribution in a two dimensional plane, the plane must be chosen to meet two criteria.

(i) Heat flow across the plane should be negligible.

(ii) The plane should represent the uniform cross section of adjacent material.

Figure 5.6 illustrates the geometry of the cutting tool. Modelling heat flow as two dimensional with respect to the end clearance face plane, AECF, the assumption must be made that heat flow in the R direction is negligible. Similarly, to model heat flow as two dimensional with respect to the side clearance face plane, ABCD, or the rake face plane, ABEG, involves assuming zero heat flow in the L and T directions respectively. Clearly such assumptions are invalid.

Figure 5.7 illustrates a plane within the tip across which heat transfer may be assumed to be zero. However, material lying perpendicularly adjacent to this plane has non - uniform cross section, and the second (geometric) criterion is not satisfied. Thus a three dimension model of heat flow in the cutting tool was developed.

Two projects were undertaken. The temperature distribution in the tool was modelled for comparison with a series of point temperatures determined experimentally. This is described in section 5.3.2.

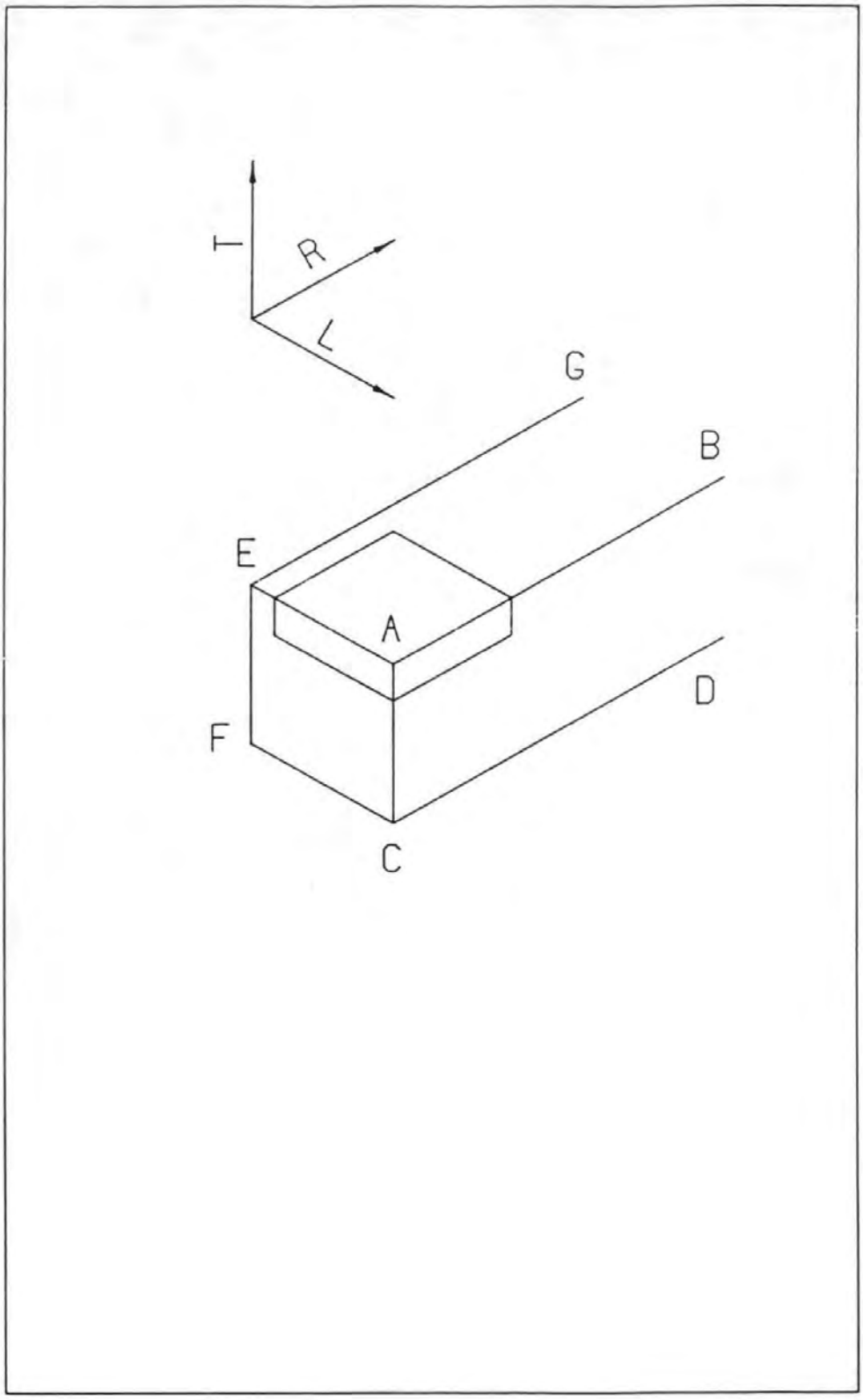

Figure 5.6 Basic Geometry Of An Insert Tool and Holder.

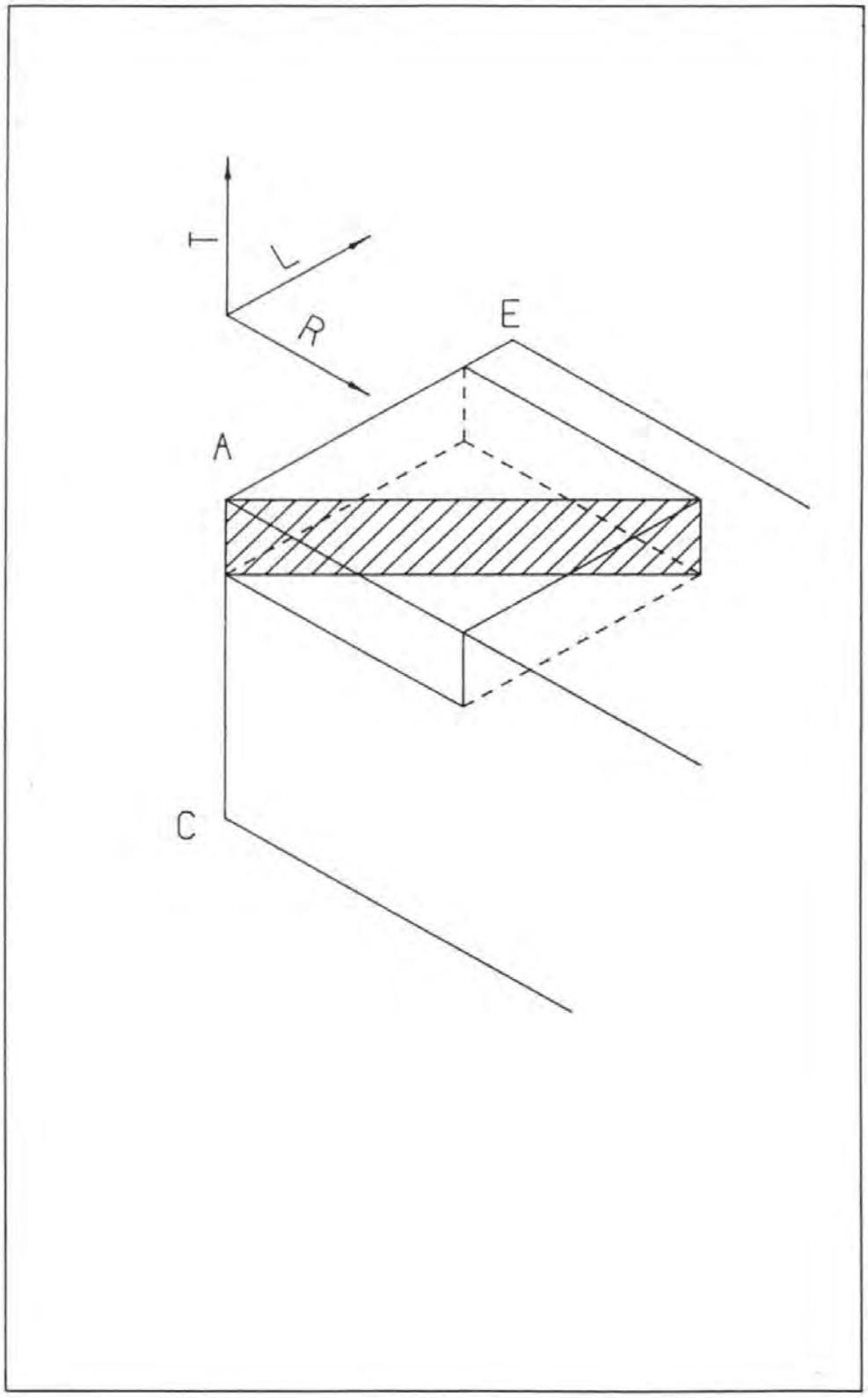

Figure 5.7

General Position Of A Plane Of Minimal Normal Heat Transfer.

The effect of a layer of temperature sensitive pigment on heat flow in the tool tip was modelled for comparison with temperatures contours recorded experimentally using temperature sensitive pigments. This is described in appendix 4.

5.3.2 Tool Temperature Distribution.

Because of uncertainty in the boundary conditions of the problem , a meaningful temperature distribution through the thickness of the tool was not determined.

Figure 5.8 illustrates the mesh constructed to investigate heat flow within the tool. Thermal properties of the materials are given in appendix 8. Heat input was modelled as a 1mm square at the corner of the insert corresponding to the cutting corner, over which a flux of 280 Watts was applied uniformly (see section 5.1.1). Boundary heat flow was modelled with a heat transfer coefficient of 1000 $W/m^2/^oc/s$ between all faces of the insert in contact with the tool holder, and a body maintained at ambient temperature. Heat transfer from the tool into the chip was modelled with a heat transfer coefficient of 10500 $W/m^2/^oc/s$ applied to the area of the heat input, with an ambient temperature of 300 ^{o}c used to simulate the presence of the chip. A high heat transfer coefficient was specified over this junction to model the intimate chip / tool contact.

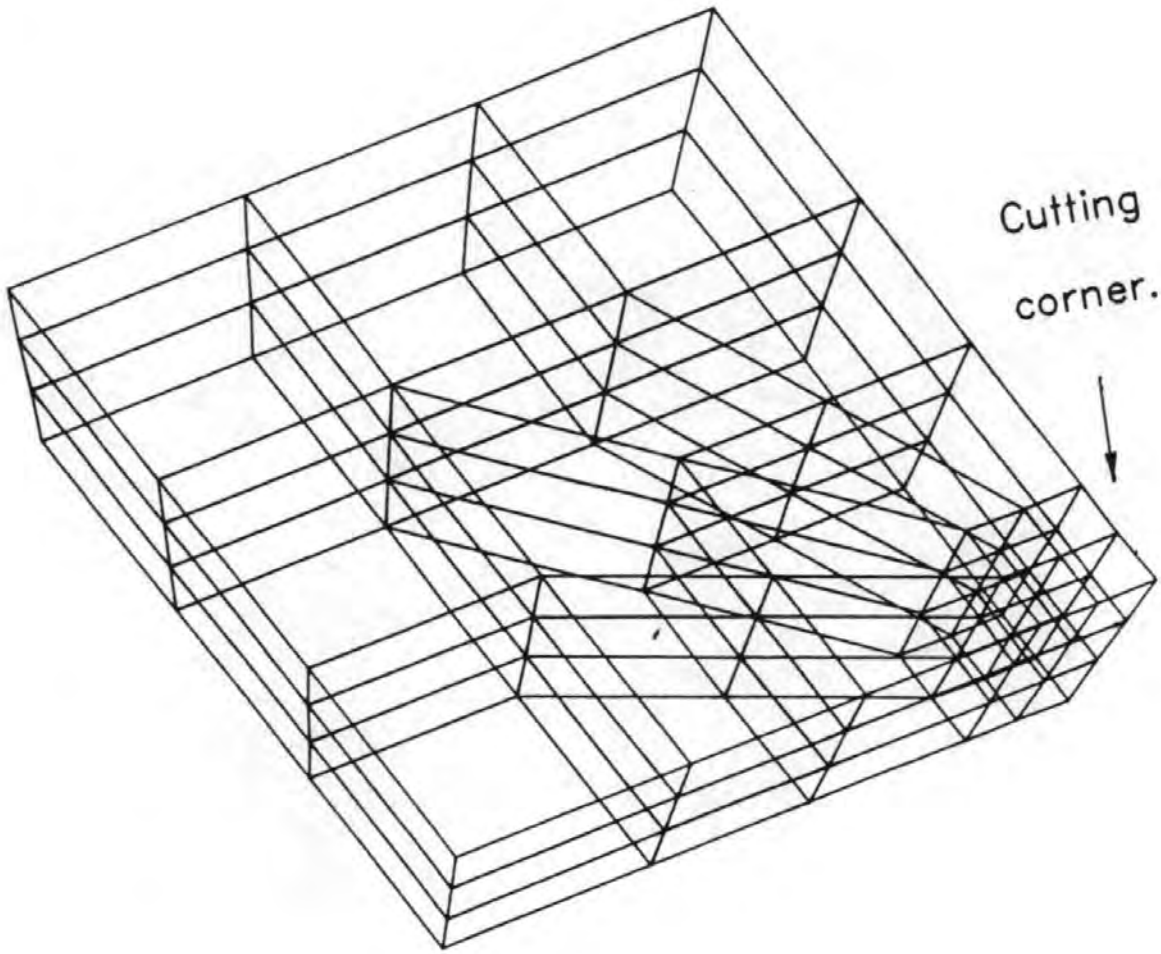

Figure 5.8 Finite Element Mesh Constructed In Order To Model Heat Flow In Cutting Tools.

A steady state solution was obtained. Figure 5.9 illustrates the general form of the temperature distribution around the toolnose. Figure 5.10 shows details of the temperature distribution. Although the magnitude of the temperatures is too high, two points are of interest.

The maximum rake face temperature is found, displaced from the cutting edge, lying approximately at the point around which crater wear features would be centred.

Two distinct bands of elevated temperature extend across the clearance faces of the insert.

This finding is of considerable interest. The relatively cool nose section of the tool is supported by warmer and ultimately softer material. This region will exhibit a reduction in yield stress, and will undergo plastic deformation above some critical combination of temperature and mechanical load.

It is likely that this is a common mechanism for catastrophic failure of the tool nose, and accounts for the fact that this phenomenon often occurs as a single short lived event, in contrast with other wear modes, such a cratering and flank wear, which progress incrementally.

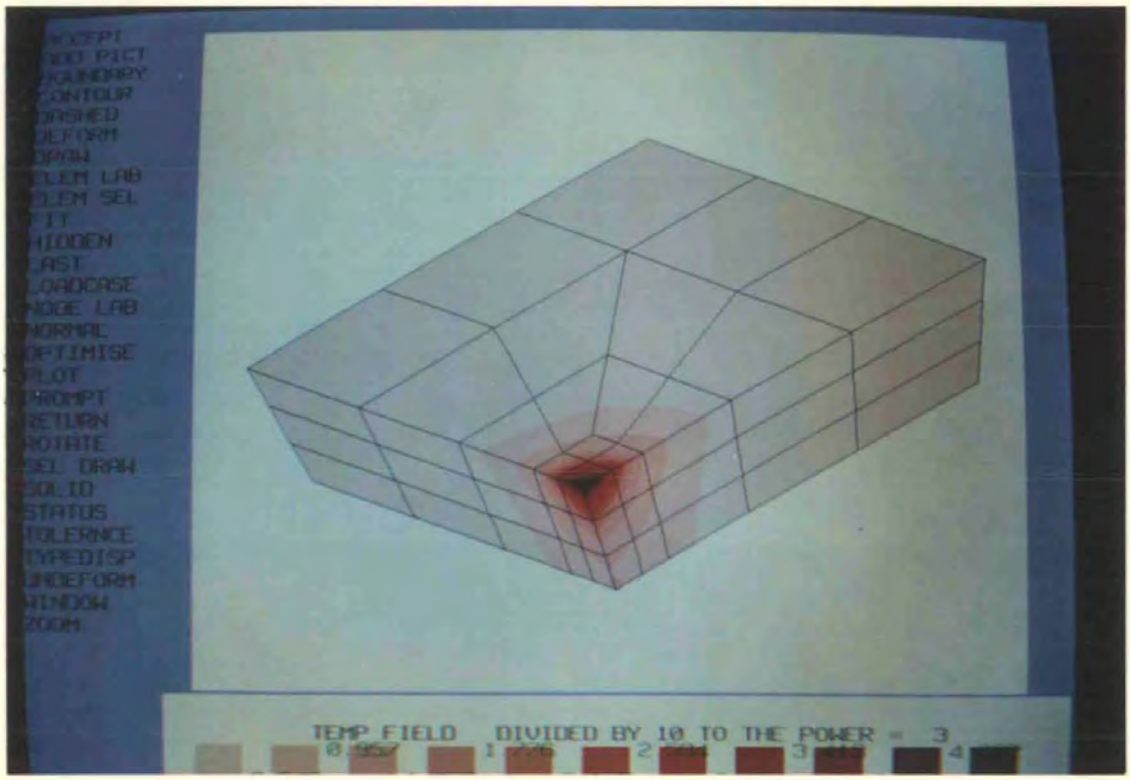

Figure 5.9 A Temperature Distribution Determined Using The Finite Element Method.

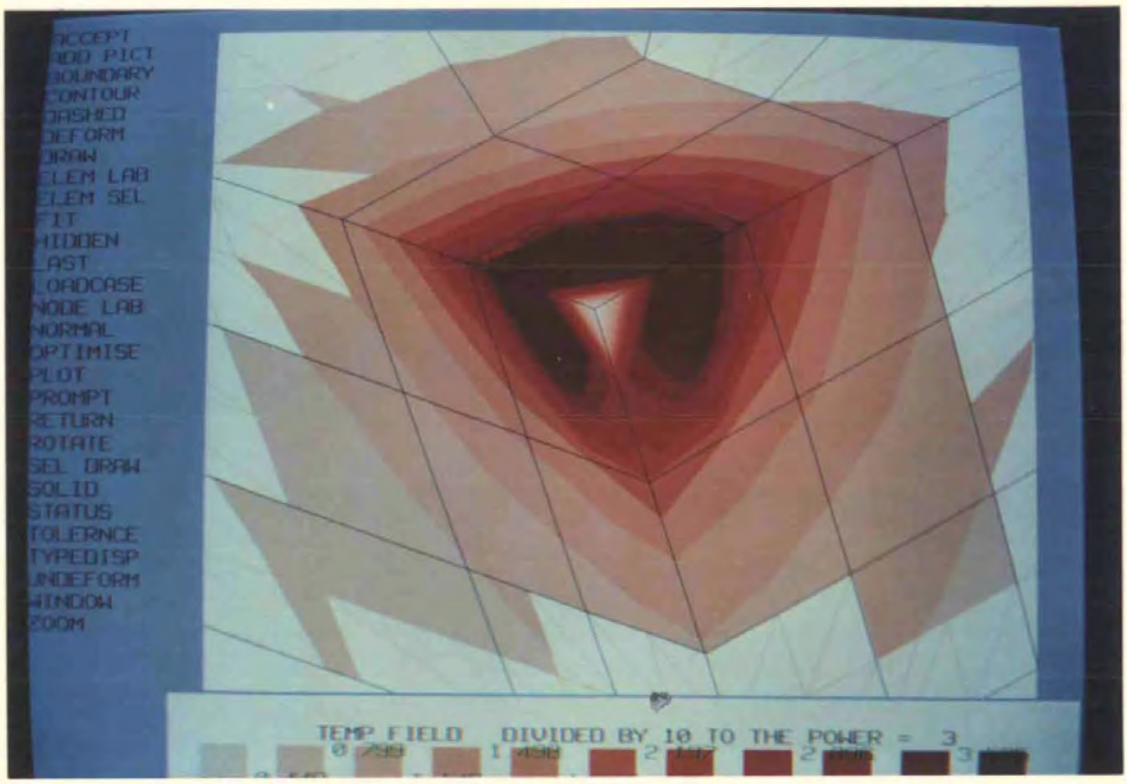

Figure 5.10 Detail Of A Temperature Distribution Around The Toolnose Determined Using The Finite Element Method.

5.4 Concluding Remarks.

Cutting temperatures obtained using implanted thermocouples were found to be in reasonable agreement with those generally available in the literature. The fact that data for direct comparison was not found in the literature demonstrates the diversity of interest underlying various authors' work and the complexity of the process variables.

Clear trends within the data presented above and correlation with measured forces provide some validation for the experimental method. However, the results themselves find few applications outside the range of test variables studied. Tool temperatures must be considered in the context of other process variables, such as the properties of the workpiece material, if it is to be used in the prediction of incremental wear.

Finite element modelling demonstrated the importance of considering heat transfer in three dimensions. Two dimensional analysis is a poor approximation to the majority of machining conditions employed commercially. Uncertainty surrounding boundary conditions limited the amount of quantitative data produced, although it seems likely that continued work in this field may yield more exact solutions.

The use of three dimensional heat transfer analysis was validated by the production of useful qualitative information. Tool temperature distributions derived using this method

indicate potential for the use of finite element heat transfer analysis in the design of tool geometries resistant to catastrophic failure of the toolnose.

Chapter 6. Concluding Remarks And Suggestions For Future Work.

6.1 Experimental Design.

The metal cutting experiments described in this thesis were designed to exclude geometric effects wherever possible. However, the effect of nitriding on chip flow angle introduced a variable which was not controlled. The effect of chip flow angle on primary shear plane area (and thus on normal force, chip tool contact pressure, and tool temperature) is discussed in appendix 2, and found to be relatively small.

The effect of chip flow angle on effective rake angle was established in section 2.9.1.1. The variation in chip flow angle with nitriding time complicates the interpretation of experimental results. A more comprehensive study of the behaviour of the built up edge around the toolnose over a range of rake angles is a promising field for future investigation.

A serious shortcoming of the experimental design was the absence of any repetition. Some spread in experimental data is commonly recorded in metal cutting tests. However, statistical analysis of the cutting force data yielded a number of well defined trends in the data. The critical conditions for the transition between sticking and sliding in the chip tool

contact zone are clearly identified in section 4.5, and the variation in chip flow angle with feedrate was sufficiently well defined to serve as the empirical basis for the development of a predictive model of chip flow.

6.2 Heat Transfer Modelling.

Establishing the heat transfer characteristics of the insert / holder contact proved to be beyond the scope of this study. However, it is important that this work should be carried out at some time, since the electrochemical machining of thermocouple cavities in wrought tools is an extremely tedious process.

The author suggests the following methods for the verification of temperature distributions derived using finite element heat transfer modelling.

The solution should be mesh independent, i.e. a finite element calculation should be repeated with another suitable arrangement of elements describing the system.

The transient response of the experimental system should be compared with that of the model. While the thermal response of the experimental system is approximately first order with respect to time, variation in the thermal conductivity of tool steel with temperature causes some deviation from the classic exponential behaviour. This effect should be modelled if the transient response is to be modelled and matched to the experimental response in a parametric study of heat transfer between the insert tool and tool holder.

Further verification may be obtained using temperature distributions determined experimentally using implanted thermocouples, temperature sensitive pigments and thermography.

6.3 Performance Of Nitrided Tools.

The performance of nitrided tools has been assessed using a number of parameters. These include change in tool temperature per frictional power generated in the secondary deformation zone, frictional coefficient, the critical condition necessary for sticking in the chip tool contact zone, and steady state tool temperatures. Optimum cutting conditions for cutting medium carbon steel (EN8) are indicated below.

6.3.1 Optimum Process Time.

Generally the optimum process time was found to be around three minutes, with much shorter or much longer process times often causing detrimental effects.

6.3.2 Optimum Rake Angle.

No well defined trend appeared in the rake angle study, although some reduction in normal force due to nitriding at negative rake angles was observed.

6.3.3 Optimum Feedrates.

Feedrates between 0.6 and 1.2 mm/rev were found to be most suitable for nitrided tools. Under such conditions normal pressure in the chip tool contact zone is less than that determined for lower feedrates. A minimal reduction in tool temperature was recorded for tools nitrided for 310 seconds between feedrates of 0.5 and 1.0 mm/rev.

6.3.4 Optimum Surface Speeds.

Optimum surface speeds vary with nitriding time. Table 6.1 has been constructed assuming the stick / slip transition as a performance criterion.

Table 6.1

Suggested Minimum Surface Speeds.

Nitriding process time. (seconds)	Minimum surface speed. (m/min)
140	40
310	30
610	< 20

However, tool temperature measurements indicate that very significant improvements in tool performance are found for tools nitrided for more than three minutes cutting at speeds far in excess of these minimum values. The author suggests that the performance of nitrided tools at surface speeds of up to and beyond 70 m/min should be investigated.

6.4 Mechanism Underlying Improved Performance.

Over a wide range of cutting conditions nitrided tools exhibit a reduction in frictional coefficient and in service temperature. Furthermore, the proportion of heat generated in the secondary shear zone entering the tool is reduced for process times of three minutes or more at all surface speeds tested. This is consistent with a reduction in the extent of sticking in the chip tool contact zone due to nitriding.

6.5 Topics For Future Work.

The author concludes that saltbath ferritic nitrocarburization brings about significant improvements in the performance of T42 high speed steel cutting tools under certain cutting conditions, and suggests that the following areas may warrant further investigation.

The performance of nitrided tools should be mapped over all combinations of a wide range of cutting conditions. Tool performance should be monitored using established wear parameters in addition to those adopted for this study in order to establish optimum process times and case depths for various cutting conditions. A variety of tool and workpiece materials

should be used.

A general appraisal of the effect of toolnose geometry should be made in terms of the effect on primary shear plane area, and related parameters such as chip / tool contact pressure and tool temperature.

The variation of chip flow angle with nitriding time and rake angle are not yet fully understood. While a number of explanations have been proposed by the author, further investigation is required in order to isolated the cause of these phenomena with any certainty. In this respect two fields of investigation warrant further work. The effect of flank wear damage due to through hardening of the cutting edge should be established, and the stability of the built up edge around the toolnose should be studied over a range of rake angles.

References.

1. Stanford K 1980

   Metallurgia, 47 (3), 109 - 111,113,114

2. Gabel M K and Donovan D M 1980

   Wear Control Handbook

   ASME 343 - 371

3. Yee K K 1978

   Int. Met. Rev. 23 19 - 42

4. Wolf D J 1977

   Wear of Materials

   ASME 263 - 330

5. Metals Handbook 1971

   8th Edition 6 63 - 65, 152 - 166, 587 - 592

   ASM

6. Sale J M 1979

   Metal Progr. 15 (4) 44, 45, 52 -55

7. Spalvins T 1977

Wear of Materials

ASME 358 - 330

8. Ramalingham S 1980

Wear Control Handbook

ASME 385 - 411

9. Bergel K Leidel B 1980

Haerterei Tech. Mitt. 35 (1) 11 - 16

10. Rupert W 1970

Baender Bleche Rohre 11 (4) 216 - 222

11. Tesaki M Yamada Y 1981

Kobe Steel Eng. Rep, Japan. 31 (3) 8 - 11

12. Takase T 1979

Denki Seiko, Japan 50 (3) 192 - 201

13. Dashfield D 1975

Heat Treatment '73

The Metals Society

14. Ecer G M Wood S Boes D Schreurs J 1983
Friction and Wear Properties Of Nitrided and N+ Implanted 17 - 4 PH Steels
Industrial Heating, April 30 - 38

15. Opitz H Konig W 1970
Basic Research On The Wear Of High Speed Steel Cutting Tools
Proc. Conf. on Materials For Metal Cutting
ISI 6 - 14

16. Henderer W E von Turkovich B F 1978
The Influence Of Heat And Surface Treatments On The Performance Of M1 High Speed Steel Taps
Influence of Metallurgy on Holemaking Operations
ASM

17. Cibaldi C 1975
Influence of Temperature On The Softening Of The Nitrided Layer...
Metal., Ital. 67 (10) 551 - 554

18. Paranjpe V G, Cohen M, Bever M B Floe C F 1950

Trans AIME 188 261 - 267

19. Dijkstra L J 1949

Trans. AIME 185 252 - 260

20. Borelius G Berglund S Avsan O 1950

Arkiv Fysik 2 551 - 557

see also Borelius G 1951

Trans. AIME 191 477 - 484

21. Anstrom H U 1954

Arkiv Fysik 8 495 - 503

Anstrom H U Borelius G 1954

Acta Met., 2 547 - 549

22. Hagg G 1927

Nature 121 826 - 827

Hagg G 1928

Nature 122 314, 962

Hagg G 1929

Nova Acta Regae Soc. Sci Upsaliensis 4 (7) 6 - 22

Hagg G 1930

Z. Physik. Chem. B8 455 - 474

23. Epstein S Cross H C Groesbeck E C Wymore I J 1929
J. Research Natl. Bur. Standards. 3 1005 - 1027
Epstein S 1929
Trans. ASST. 16 19 - 65

24. Lakhtin Yu M Kogan Ya D Solodkin G A 1983
Strengthening Mechanisms of Nitrided Layers of Alloy Steels
Moscow Automobile Highway Institute, No. 2 25 - 29

25. Osawa A Iwaizumi S 1928
Z. Krist 69 26 -34
Osawa A Iwaizumi S 1929
Science Repts. Tohoku Univ. 18 79 - 89

26. Jack K H 1951
Proc. Roy. Soc. (London). A208 200 - 215

27. Jack K H 1948
Proc. Roy. Soc. (London). A195 34 - 40

28. Jack K H 1952
Acta Cryst. 5 404 - 411.

29. Bell T Birch B J Koreatnenko V Evans S P 1975

Heat Treatment '73 51 - 57

The Metals Society

30. Mitchell E Dawes C 1964

Molten Salt Bath Nitriding

Metal Treatment and Drop Forging 31 220 3 - 16

31. Naumann F K 1965

Langersheid, G. Arch Eisenhutten. 36, 667 - 682

32. Grieve D J 1981

Optimum Heat Treatment Of Tools

TIPTOM 1981 149 - 153

The Metals Society

33. Refractory Materials, vol 7 1967

Academic Press

34. Encyclopaedia Of Chemical Technology

John Wiley & Sons Inc 1963

35. Astley P 1975

Liquid Nitriding. Developement and Present Applications

Heat Teatment '73 93 - 97

The Metals Society

36. Nitriding of ferrous materials

WIRE 30 3 139 - 140 1980

37. Pulkkinen R E E 1982

Formation Of Surface Iron Nitrides

J. Mater. Sci. Letters, 1 10 421 - 422

38. Goldschmidt H J 1967

Interstitial Alloys

Butterworth

39. Martin W J 1968

Precipitation Hardening

Pergamon

40. Trent E M 1979

Wear Of Metal Cutting Tools

Treatise on Materials Science and Technology

13 443 - 489

41. Takayama Y Ono T 1966

Study on The Roughness Of Turned Surfaces

The Japan Soc. of Prec. Eng. 1 4 274 - 280

42. Solaja V 1972

Contribution to Surface Finish.Evaluation in Machining

Annuals CIRP 21 151 - 2

43. Childs T H C Smith A B 1982

TIPTOM 1982 235 - 239

The Metals Society

44. Singh J Khare M K 1983

Machining Ratio As A Basis For Tool Life Assessment

Wear 88 2 145 - 154

45. Rao I V and Lal G K 1977

Tool Life At High Cutting Speeds

Int. J. Mach. Tool. Des. Res. 17 233 - 243

46. Uehara K 1975

Charactaristics of Tool Wear Based On Flank and Crater Wear

- A Proposal on Measurement of Tool Life

Ann. CIRP, 24 59 - 64

47. Pandit S M Kashou S 1983

Variation In Frictional Coefficient With Tool Wear

WEAR 84, (1), 65 - 79

48. Schey J A 1983

Tribology In Metal Working

ASM

49. Zorev N N 1963

Proc. Int Production Engineering Research Conf. 42

ASME

50. Kato S Yamaguchi K Yamada M Yamada, 1972

Trans. ASME Ser B.J.Eng Ind, 94 683 - 689

51. Montag G Hoppner J 1974

Fertigungtech Betr. 24 407 - 412

52. Sampath W S Shaw M C 1983

Proc 11th NAMRC

SME

53. Warneck G 1977

Proc 5th NAMRC 229-236

SME

54. Oxley P B L 1982

Proc. 22nd Int. MTDR Conf 279 - 287

Macmillan

55. Matthew P Oxley P B L 1981

Wear 69 219-234

56. Tay A O Stevenson M G De Vahl Davis G Oxley P B L 1976

Int. J. Mach. Tool Des. Res. 16 335 - 349

57. Trent E M 1984

Metal Cutting

Butterworths

58. Tool and Manufacturing Engineers Handbook 1983

4th Edition Volume 1 Machining

SME

59. Ernst H Merchant M E 1941

in Surface Treatments of Metals 29 299

ASM

60. Merchant M E 1948

J. Appl. Phys. 19 876 - 881

61. Shaw M C 1984

Metal Cutting Principles

Clarendon Press

62. Bailey J A 1975

Wear 31 243-275

63. Thomson E G MacDonald A G Koayashi S 1962

Trans ASME Ser. B, J.Eng.Ind, 84 53-62

64. Zorev N N 1962

Metal Cutting Mechanics

Pergammon

65. Wallace P W Boothroyd G 1964

J.Mech Eng Sci. 6 74 - 78, 306 - 308, 422 - 423

Wallace P W Boothroyd G 1965

J Mech Eng Sci. 7 118 - 123

66. Abdelmoneim M Es 1980

WEAR 58 173 - 192

67. Kronenberg M 1966

Machining Science and Application

Pergammon

68. Abdelmoneim M Es Scrutton R F 1973

Wear 24 1-13

69. Hoshi T 1981

Cutting Tool Material

ASM

70. Stabler G V 1951

The Fundamental Geometry Of Cutting Tools

Proc. Instn. Mech. Engrs. 165 14 - 21

71. Young H T Mathew P Oxley P B L 1987

Proc Instn Mech Engrs 201 C3

72. Kronenberg M 1949

Am. Mach. 93 104

73. Shaw M C 1958

Technische Mitteilungen (Essen) 5 211 - 216

74. Blok H 1938

Proc. Gen. Discussion on Lubrication and Lubricants

Inst. Mech. Engrs. 152, 222

75. Knight G H

British Steel Swindon Laboratories

Private communication

76. Kaye G W C Laby T H 1968

Tables of Physical and Chemical Constants

Longmans

77. Iwata K Moriwaki T 1977

Annals of the CIRP 25 (1), 21 - 26

78. Lee H J Lee S K Lee C O 1983

Thermal Conductivity 17.

Plennum Press.

Appendix 1. Primary Shear Force For Non - Zero Rake Angle.

The applied tangential force Ft contains two components, one, Fts overcoming the primary shear yield force and the other, Ftf, overcoming the frictional force between the chip and the tool.i.e.

$$Ft = Fts + Ftf$$

Evaluation of Fts.

From conservation of work done per second, when $\mu = 0$,

$$Fts.vb = Fs.vs$$

$$Fts = \frac{Fs.vs}{vb}$$

From figure A1.1

$$\frac{va}{\sin\phi} = \frac{vb}{\cos(\phi - \alpha)} = \frac{vs}{\cos\alpha} \qquad -(i)$$

$$\frac{vs}{vb} = \frac{\cos}{\cos(\phi - \alpha)}$$

$$Fts = \frac{Fs.\cos}{\cos(\phi - \alpha)} \qquad -(ii)$$

Evaluation of Ftf.

From conservation of work done per second, when $s = 0$,

$$Ftf.vb = Ff.va$$

$$Ftf = \frac{Ff.va}{vb}$$

From -(i)

$$\frac{va}{\sin\phi} = \frac{vb}{\cos(\phi - \alpha)}$$

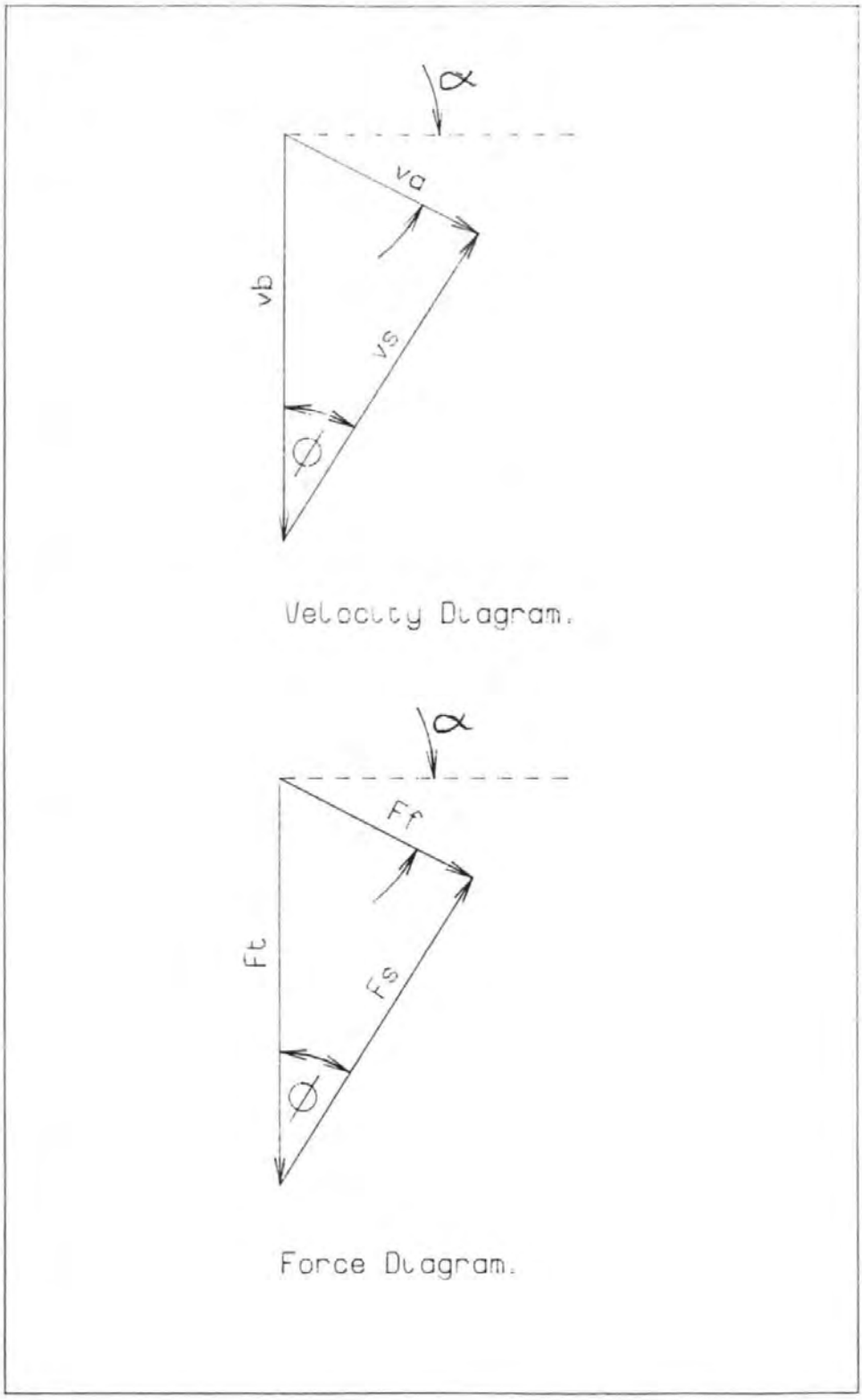

Figure A1.1 Chip Velocity For Non – Zero Rake Angle.

$$\frac{va}{vb} = \frac{\sin\phi}{\cos(\phi - \alpha)}$$

$$Ftf = \frac{Ff.\sin\phi}{\cos(\phi - \alpha)} \qquad -(iii)$$

Summing -(ii) and -(iii)

$$Ft = Fts + Ftf$$

$$= \frac{\cos\alpha}{\cos(\phi - \alpha)} + \frac{Ff.\sin\phi}{\cos(\phi - \alpha)}$$

$$Fs = \frac{Ft.\cos(\phi - \alpha) - Ff.\sin\phi}{\cos\alpha}$$

Appendix 2. Evaluation of Primary Shear Plane Area.

The expression

$$\frac{\tau_s . I}{\sin\phi} = Ft.\cos\phi - Ff\sin\phi \qquad \text{-Eq. A2.1}$$

where Ft = tangential (cutting) force

Ff = frictional force

τ_s = work material shear stress

ϕ = primary shear angle

derived in section 2.9.2.1 produced reasonable values for primary shear angle. It contains a term, $I/\sin\phi$, describing primary shear plane area as a function of, I, the integral of shear plane length over engaged cutting edge length. However, this method is only approximate for tools with a nose radius. A more precise method for determining the primary shear plane area is described in the following text. Figures illustrating shear around the toolnose contain a rectangular section of the rake face plane to act as a visual reference.

For orthogonal tube cutting, primary shear plane area may be determined as

$$Aps = \frac{F.DOC}{\sin\phi} \qquad \text{-Eq. A2.2}$$

where DOC = depth of cut

F = feed per revolution

This is illustrated in figure A2.1. However, for a tool with a nose radius, a curved shear plane, illustrated in figure A2.2, is produced, and expression A2.2 is no longer valid. Furthermore, the curvature of the shearplane varies as a function of primary shear angle.

In figure A2.3, a tool cutting at zero rake angle is considered. When the primary shear angle is 90 degrees, the shearplane lies in the tool rake face plane and occupies an area equal to the undeformed chip cross section. This area may be obtained as the integral of shear plane length (F in this case) over dS (see figure 2.10) in the general case, or when ϕ = 90 (see figure A2.3), over depth of cut.

In figure A2.4 the same tool is considered. The upper boundary of the work material has been imposed in order to define the shear plane length, again denoted F. When the primary shear

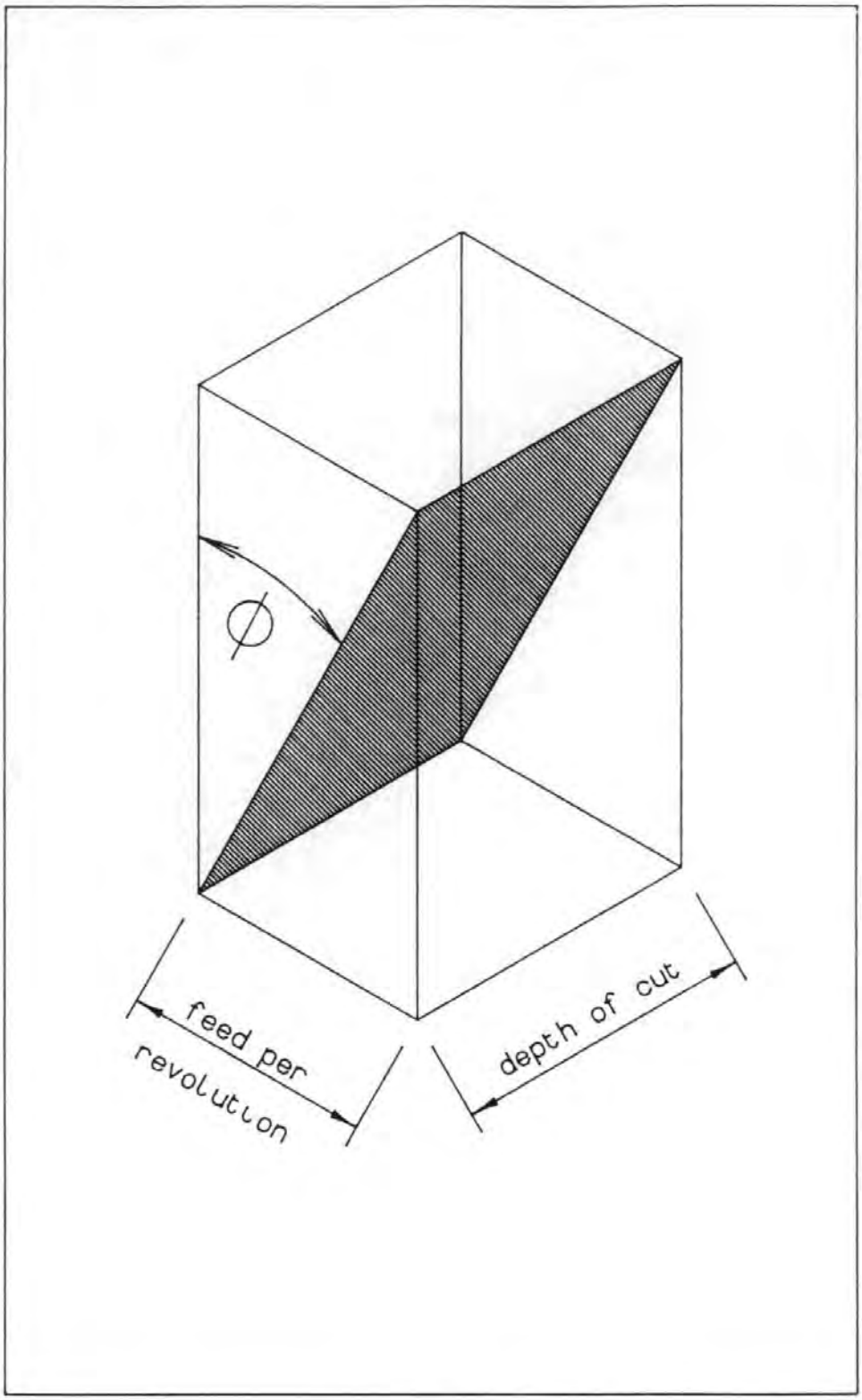

Figure A2.1

Primary Shear Plane Produced In Ideal Orthogonal Cutting.

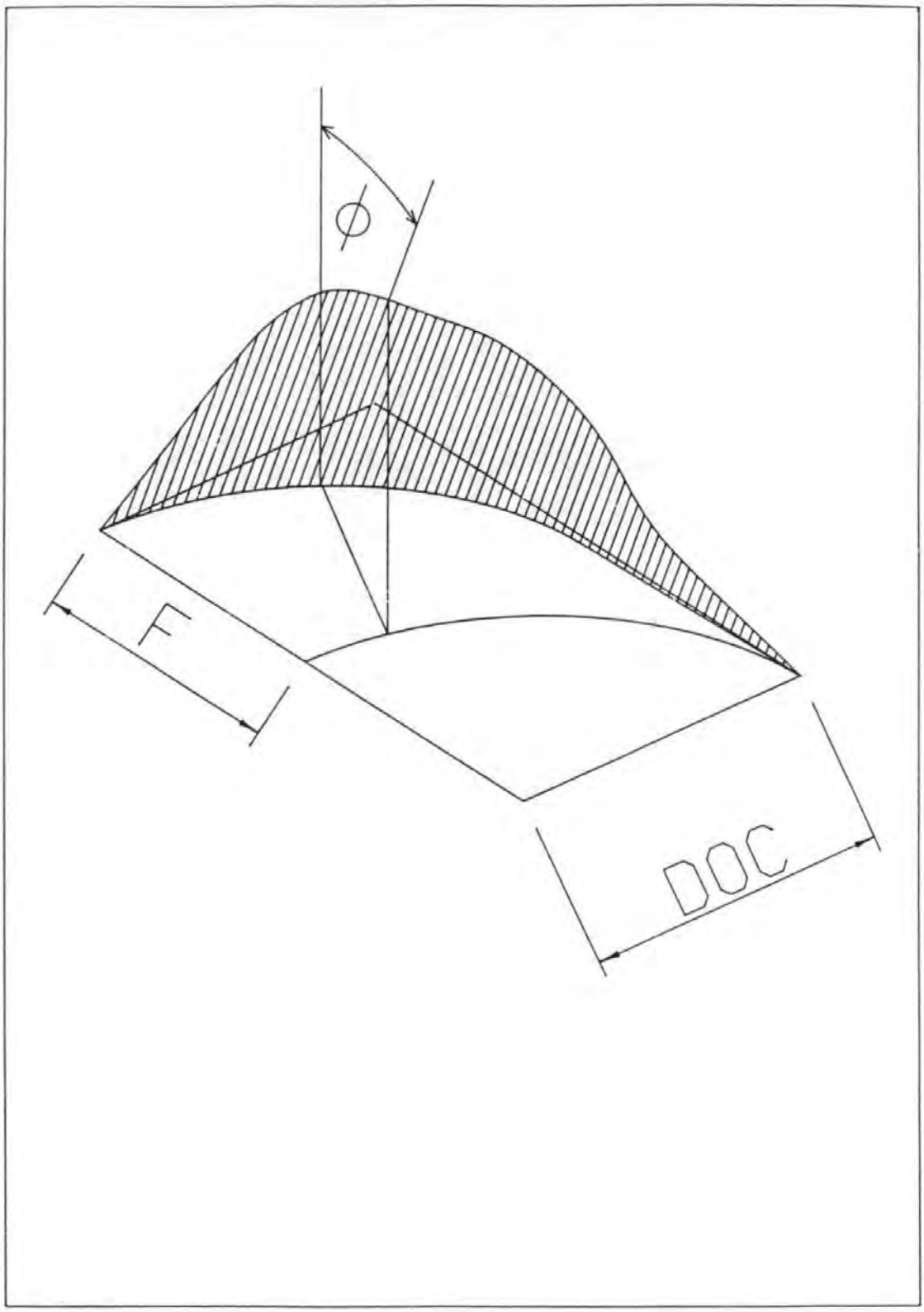

Figure A2.2

Primary Shear Plane Produced By A Tool With A Nose Radius.

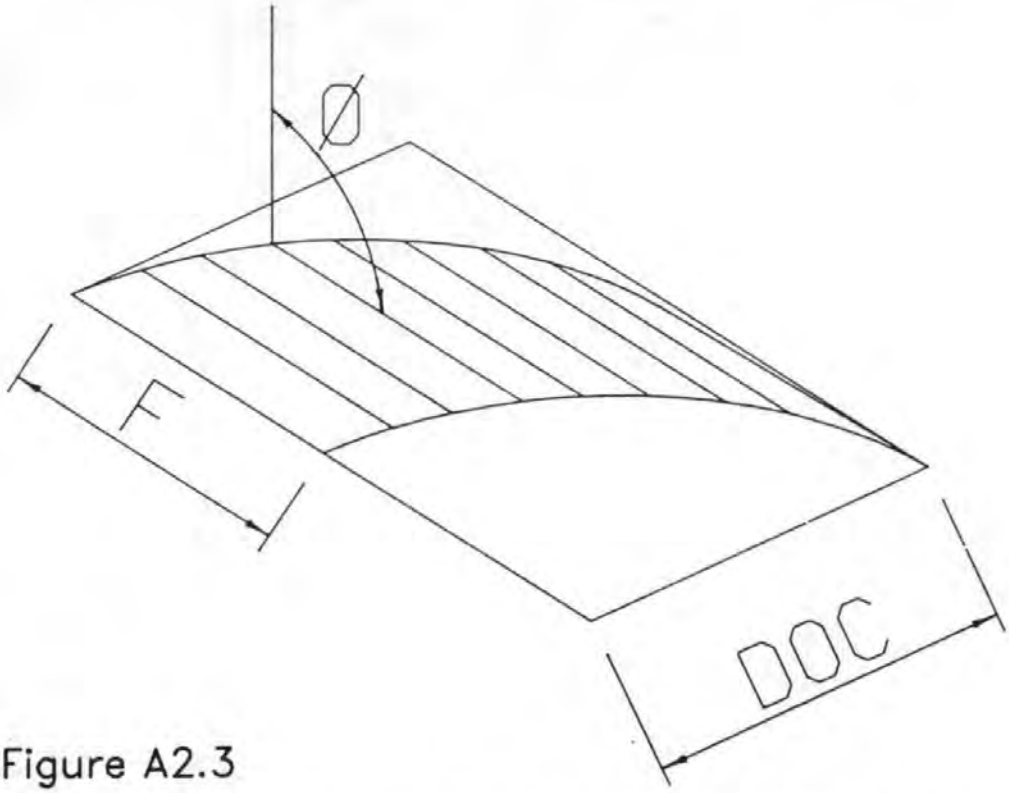

Figure A2.3

Primary Shear Plane Produced When $\phi = 90°$.

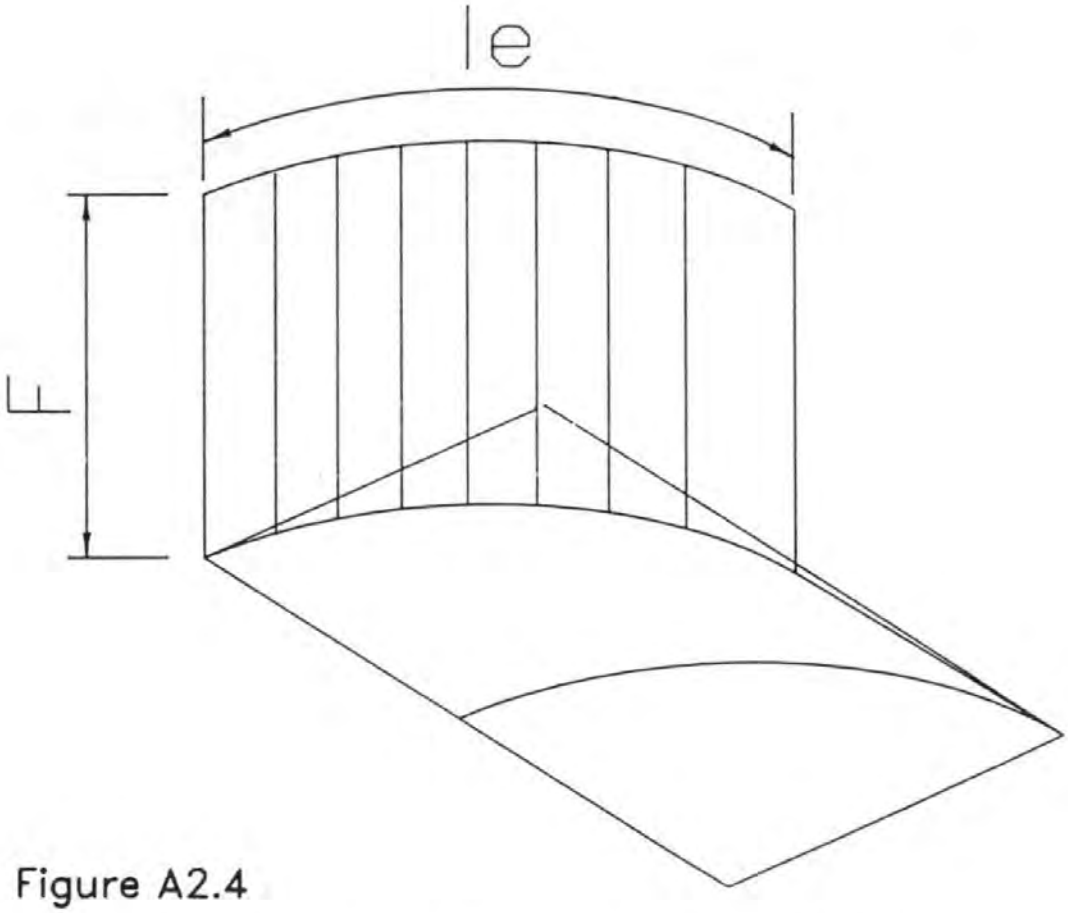

Figure A2.4

Primary Shear Plane Produced When $\phi = 0°$.

angle is zero, the shear plane area must be determined as the integral of shear plane length over the engaged cutting edge length, le.

For primary shear angle between 0 and 90 degrees, neither of these two methods is appropriate. Under such conditions, the curvature of the shearplane no longer adopts a clearly defined form, and it's area becomes dependant on chip flow angle.

The numeric method described below was used to evaluate primary shear plane area and demonstrate the variation with chip flow angle.

The primary shear plane was divided into a number of segments, figure A2.5, within each of which the curvature was assumed to be negligible. These then approximate to the trapezium in figure A2.6. The area of each trapezium was determined as the product of mean shear plane length and OC. Local shear plane length was determined from pathlengths described in section 2.10.3 and primary shear angle.

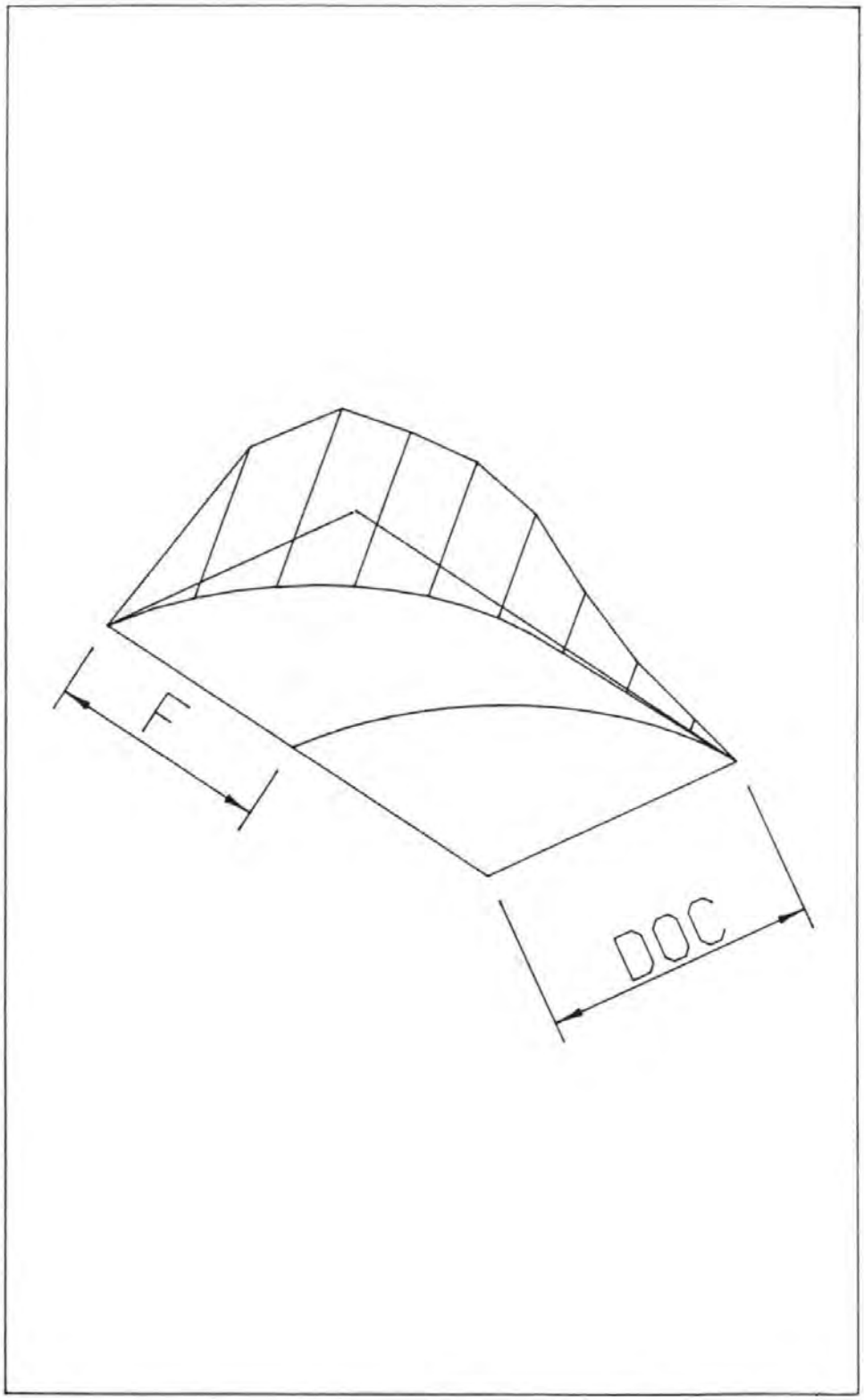

Figure A2.5 Division Of The Primary Shear Plane Into A Number Of Segments.

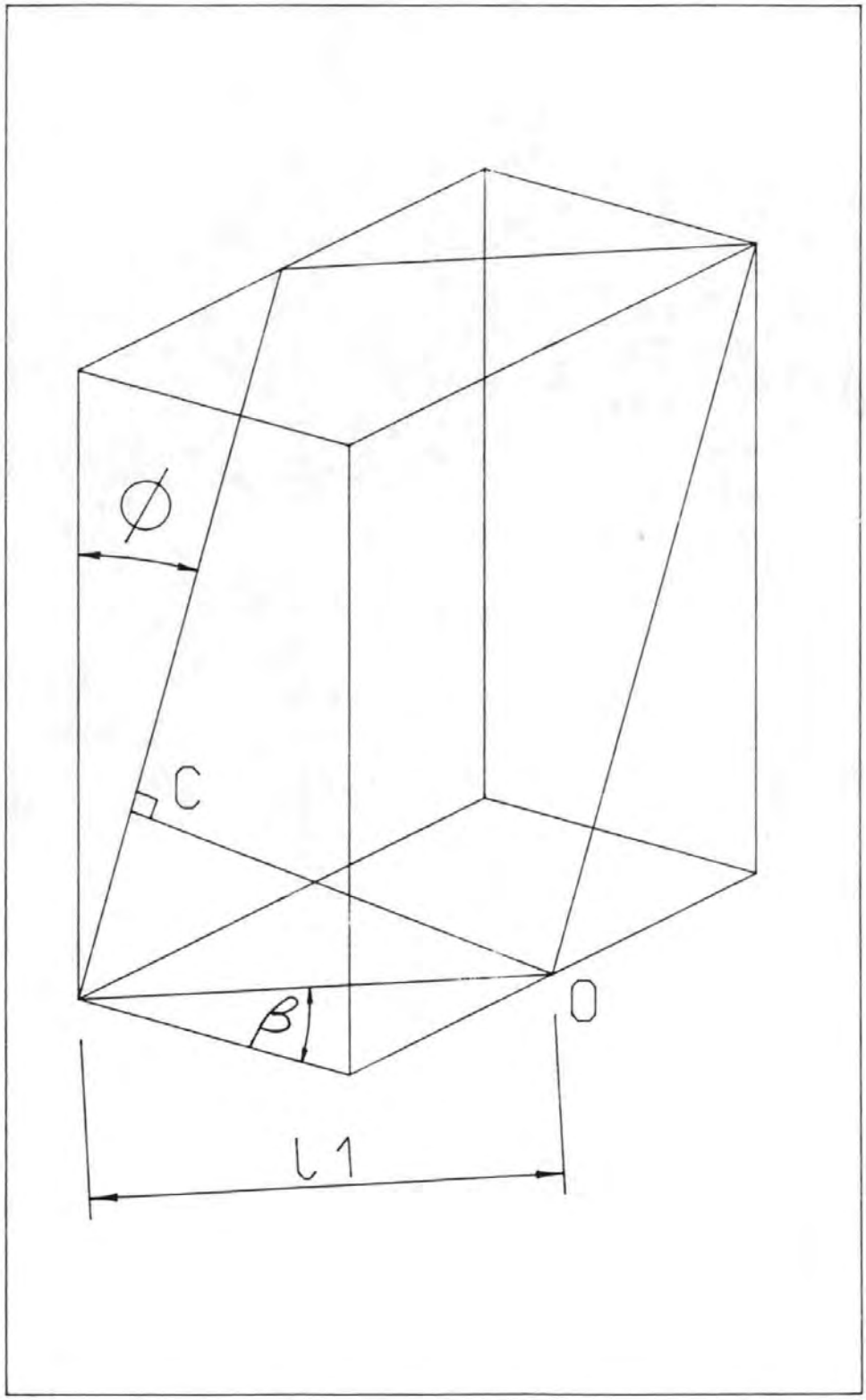

Figure A2.6 A Primary Shear Plane Segment.

The following expression for OC was derived.

$$OC = l1\sqrt{\sin^2\beta.\cos^2\phi + \cos^2\beta} \qquad \text{-Eq. A2.3}$$

where l1 = engaged cutting edge segment length

ϕ = primary shear angle

β = included angle between local tangent to the toolnose and the perpendicular to the direction of chip flow lying in the rake face plane.

Primary shear plane areas were obtained as the sum of the areas of these trapezium sections. Although each section is flat, the overall curvature of the plane is modelled by the inclusion of the β terms in expression A2.3, which vary around the toolnose. Three sets of values for primary shear plane area are set out in table A2.1. Unbracketed values were obtained using the trapezium segment method. These are the most accurate. Shear plane areas derived using two simple approximate methods are also shown. Those values marked () were obtained as the integral of local undeformed chip thickness over engaged cutting edge length, divided by $\sin\phi$. Those values marked [] were obtained as the integral of local undeformed chip thickness over dS (see figure 2.10), divided by $\sin\phi$. This third set of values exhibits no variation with chip flow angle, since the integral of local undeformed chip

thickness over dS is equal to the undeformed chip cross sectional area for any chip flow angle.

Table 2.1. Primary Shear Plane Areas.

Feedrate = 0.2 mm/rev.

ϕ	γ = 45	γ = 50	γ = 55	γ = 60	γ = 65
8	1.6350	1.6022	1.5807	1.5757	1.5864
	(1.6483)	(1.6109)	(1.5893)	(1.5850)	(1.5958)
	[1.4370]	[1.4370]	[1.4370]	[1.4370]	[1.4370]
12	1.0915	1.0700	1.0558	1.0525	1.0595
	(1.1033)	(1.0783)	(1.0639)	(1.0610)	(1.0682)
	[0.9619]	[0.9619]	[0.9619]	[0.9619]	[0.9619]
16	0.8203	0.8044	0.7940	0.7915	0.7967
	(0.8322)	(0.8133)	(0.8025)	(0.8003)	(0.8057)
	[0.7255]	[0.7255]	[0.7255]	[0.7255]	[0.7255]
20	0.6579	0.6456	0.6375	0.6355	0.6395
	(0.6707)	(0.6555)	(0.6467)	(0.6449)	(0.6493)
	[0.5847]	[0.5847]	[0.5847]	[0.5847]	[0.5847]
24	0.5501	0.5402	0.5336	0.5320	0.5352
	(0.5640)	(0.5512)	(0.5438)	(0.5423)	(0.5460)
	[0.4917]	[0.4917]	[0.4917]	[0.4917]	[0.4917]

Feedrate= 0.4 mm/rev.

ø	γ= 40	γ= 45	γ= 50	γ= 55	γ= 60
8	3.2746	3.2252	3.2047	3.2066	3.2302
	(3.3339)	(3.2829)	(3.2614)	(3.2355)	(3.2858)
	[2.8741]	[2.8741]	[2.8741]	[2.8741]	[2.8741]
12	2.1862	2.1539	2.1404	2.1417	2.1572
	(2.2317)	(2.1975)	(2.1831)	(2.1658)	(2.1994)
	[1.9238]	[1.9238]	[1.9238]	[1.9238]	[1.9238]
16	1.6431	1.6194	1.6096	1.6105	1.6219
	(1.6833)	(1.6576)	(1.6467)	(1.6336)	(1.6590)
	[1.4511]	[1.4511]	[1.4511]	[1.4511]	[1.4511]
20	1.3181	1.2998	1.2921	1.2929	1.3018
	(1.3566)	(1.3358)	(1.3271)	(1.3165)	(1.3370)
	[1.1695]	[1.1695]	[1.1695]	[1.1695]	[1.1695]
24	1.1023	1.0877	1.0815	1.0822	1.0893
	(1.1407)	(1.1233)	(1.1159)	(1.1071)	(1.1243)
	[0.9834]	[0.9834]	[0.9834]	[0.9834]	[0.9834]

Feedrate= 0.6 mm/rev.

ϕ	γ= 30	γ= 35	γ= 40	γ= 45	γ= 50
8	4.9659	4.8770	4.8329	4.8150	4.8200
	(5.1798)	(5.0879)	(5.0376)	(5.0182)	(5.0218)
	[4.3111]	[4.3111]	[4.3111]	[4.3111]	[4.3111]
12	3.3151	3.2565	3.2275	3.2158	3.2190
	(3.4673)	(3.4057)	(3.3721)	(3.3591)	(3.3615)
	[2.8858]	[2.8858]	[2.8858]	[2.8858]	[2.8858]
16	2.4912	2.4479	2.4267	2.4180	2.4204
	(2.6153)	(2.5689)	(2.5435)	(2.5337)	(2.5355)
	[2.1767]	[2.1767]	[2.1767]	[2.1767]	[2.1767]
20	1.9982	1.9642	1.9477	1.9410	1.9427
	(2.1077)	(2.0703)	(2.0498)	(2.0419)	(2.0434)
	[1.7542]	[1.7542]	[1.7542]	[1.7542]	[1.7542]
24	1.6707	1.6431	1.6298	1.6244	1.6258
	(1.7723)	(1.7409)	(1.7237)	(1.7170)	(1.7183)
	[1.4751]	[1.4751]	[1.4751]	[1.4751]	[1.4751]

Feedrate= 0.8 mm/rev.

ϕ	γ = 25	γ = 30	γ = 35	γ = 40	γ = 45
8	6.5695	4.4939	6.4363	6.4128	6.4271
	(7.066)	(6.9970)	(6.9215)	(6.8928)	(6.9460)
	[5.7482]	[5.7482]	[5.7482]	[5.7482]	[5.7482]
12	4.3865	4.3367	4.2986	4.2829	4.2923
	(4.7298)	(4.6837)	(4.6332)	(4.6139)	(4.6495)
	[3.8477]	[3.8477]	[3.8477]	[3.8477]	[3.8477]
16	3.2971	3.2605	3.2322	3.2205	3.2272
	(3.5677)	(3.5329)	(3.4948)	(3.4802)	(3.5071)
	[2.9023]	[2.9023]	[2.9023]	[2.9023]	[2.9023]
20	2.6454	2.6168	2.5945	2.5851	2.5903
	(2.8752)	(2.8472)	(2.8165)	(2.8048)	(2.8264)
	[2.3390]	[2.3390]	[2.3390]	[2.3390]	[2.3390]
24	2.2127	2.1896	2.1713	2.1635	2.1676
	(2.4177)	(2.3941)	(2.3683)	(2.3585)	(2.3767)
	[1.9668]	[1.9668]	[1.9668]	[1.9668]	[1.9668]

Feedrate= 1.0 mm/rev.

ϕ	γ = 25	γ = 30	γ = 35	γ = 40	γ = 45
8	8.0895	8.0423	8.0388	8.0577	8.1179
	(8.9809)	(8.9306)	(8.9284)	(8.9485)	(9.0146)
	[7.1852]	[7.1850]	[7.1852]	[7.1852]	[7.1852]
12	5.4006	5.3693	5.3669	5.3791	5.4187
	(6.0116)	(5.978)	(5.9765)	(5.9900)	(6.0342)
	[4.8097]	[4.8097]	[4.8097]	[4.8097]	[4.8097]
16	4.0585	4.0354	4.0336	4.0423	4.0714
	(4.5345)	(4.5091)	(4.5080)	(4.5182)	(4.5516)
	[3.6279]	[3.6279]	[3.6279]	[3.6279]	[3.6279]
20	3.2555	3.2372	3.2358	3.2423	3.2650
	(3.6544)	(3.6339)	(3.6331)	(3.6413)	(3.6682)
	[2.9238]	[2.9238]	[2.9238]	[2.9238]	[2.9238]
24	2.7221	2.7072	2.7060	2.7110	2.7293
	(3.0729)	(3.0557)	(3.0550)	(3.0619)	(3.0845)
	[2.4585]	[2.4585]	[2.4585]	[2.4585]	[2.4585]

Feedrate= 1.2 mm/rev.

ϕ	γ= 20	γ= 25	γ= 30	γ= 35	γ= 40
8	9.7078	9.6301	9.6334	9.6914	9.7710
	(11.0596)	(10.9970)	(11.0172)	(11.0811)	(11.1939)
	[8.6223]	[8.6223]	[8.6223]	[8.6223]	[8.6223]
12	6.4839	6.4319	6.4336	6.4717	6.5235
	(7.4031)	(7.3612)	(7.3747)	(7.4175)	(7.4930)
	[5.7716]	[5.7716]	[5.7716]	[5.7716]	[5.7716]
16	4.8758	4.8633	4.8374	4.8653	4.9029
	(5.5841)	(5.5525)	(5.5627)	(5.5950)	(5.6519)
	[4.3535]	[4.3535]	[4.3535]	[4.3535]	[4.3535]
20	3.9142	3.8827	3.8828	3.9045	3.9333
	(4.5003)	(4.4748)	(4.4830)	(4.5090)	(4.5549)
	[3.5085]	[3.5085]	[3.5085]	[3.5085]	[3.5085]
24	3.2761	3.2497	3.2493	3.2667	3.2895
	(3.7842)	(3.7628)	(3.7697)	(3.7916)	(3.8302)
	[2.9503]	[2.9503]	[2.9503]	[2.9503]	[2.9503]

For zero rake angle cutting, the experimental values for shear angle tend to be around 20 degrees. This is closer to 0 degrees than to 90 degrees, so values of shear plane area derived from the integral over engaged cutting edge length (Ile) are found to be in good agreement with those obtained using the trapezium segment method.

This is of interest because primary shear angles were determined from shear plane areas evaluated from the integral over engaged cutting edge length in the results sections. At higher feedrates these values are less accurate, and for a feedrate of 1.2 mm/rev the maximum error was found to be around +14 %. When such an error is carried over into the evaluation of shear angle, an error of around +2 degrees is observed.

To conclude, expression A2.1 is of particular use in determining primary shear angle in the orthogonal case, for which primary shear plane area may be determined as a sine function of undeformed chip cross section. For a tool with a nose radius, no general analytic expression for primary shear plane area was derived, and values were determined numerically.

However, the integral of shear plane length over engaged cutting edge length may be used in place of undeformed chip thickness in expression A2.1 to produce reasonably accurate

values for shear angles at low feedrates.

Appendix 3. Gauss Seidel Iteration.

Gauss Seidel iteration is analogous to a substitution method in which one variable is expressed explicitly as a function of the other.

In this case the following calibration equations must be solved for Ft, Fl and Fr.

$$Reading(1) = Ft(t1) + Fl(l1) + Fr(r1)$$

$$Reading(2) = Ft(t2) + Fl(l2) + Fr(r2)$$

$$Reading(3) = Ft(t3) + Fl(l3) + Fr(r3)$$

Where the readings 1 to 3 are the recorded amplified bridge imbalances and the bracketed coefficients are calibration constants. An initial solution set (a) is found by assuming zero cross - sensitivity.

$$Ft(a) = Reading(1)/t1$$

$$Fl(a) = Reading(2)/l2$$

$$Fr(a) = Reading(3)/r3$$

From the calibration equations it is clear that reading (1) contains components due to Fl and Fr. Using the values of Fl and Fr from the initial solution, these may be expressed as

$$Fl(a).l1 + Fr(a).r1$$

By subtraction a new value, Ft(b) may be derived.

$$Ft(b) = \frac{Reading(1) - (Fl(a).l1 + Fr(a).r1)}{t1}$$

Fl and Fr may be similarly re - evaluated and the calculation repeated.

For the nth case

$$Ft(n) = \frac{Reading(1) - (Fl(n-1).l1 + Fr(n-1).r1)}{t1}$$

$$Fl(n) = \frac{Reading(2) - (Ft(n-1).t2 + Fr(n-1).r2)}{l2}$$

$$Fr(n) = \frac{Reading(3) - (Ft(n-1).t3 + Fl(n-1).l3)}{r3}$$

Subsequent values may be substituted until the new approximation agrees with the old to within some small limit, in this case governed by the arithmetic precision of the computer. A typical solution series is given in table A3.1.

Table A3.1.

Typical Solution Series Produced Using Gauss Seidel Iteration.

Approximation Number	Tangential force.	Longitudinal force.	Radial force.
0	1051.06279	494.88240	412.44805
1	1028.33080	478.92376	466.78046
2	1027.57669	478.40112	465.08321
3	1027.62844	478.43179	465.07575
4	1027.62881	478.43205	465.03087
5	1027.62873	478.43200	465.03091
6	1027.62873	478.43200	465.03090
7	1027.62873	478.43200	465.03090

A drawback of the Gauss Seidel method is that the iterative series does not always converge. One hundred sets of readings were taken during each cutting test. Of these around one set in five hundred failed to generate a convergent iterative series. In these cases further iteration was abandoned after twenty steps and all solutions rejected. This lead to a loss of one per cent of data from that test.

Appendix 4.

The Effect of An Insulative Layer On Heat Flow In A Cutting Tool.

The mesh in figure A4.1 was developed to study the influence of a layer of temperature sensitive pigment on heat flow in the insert tool. Thermal properties of the tool material are detailed in appendix 8. Boundary heat transfer between the insert and tool holder was modelled using a heat transfer coefficient of 10000 $J/m^2/^oc/s$ between all faces of the insert in contact with the tool holder and a body maintained at ambient temperature. This value may be rather high, but was selected so that the results might be applicable to and similar work carried out using wrought tools.

From appendix 7 it is clear that the temperature distribution will vary as a function of heat transfer coefficient, and for this reason results presented below provide only qualitative information.

The heating effect of the chip / tool contact was modelled as a square of side 2mm in the cutting corner, over which a flux of 43 Watts was applied uniformly (see section 5.1.1). This zone

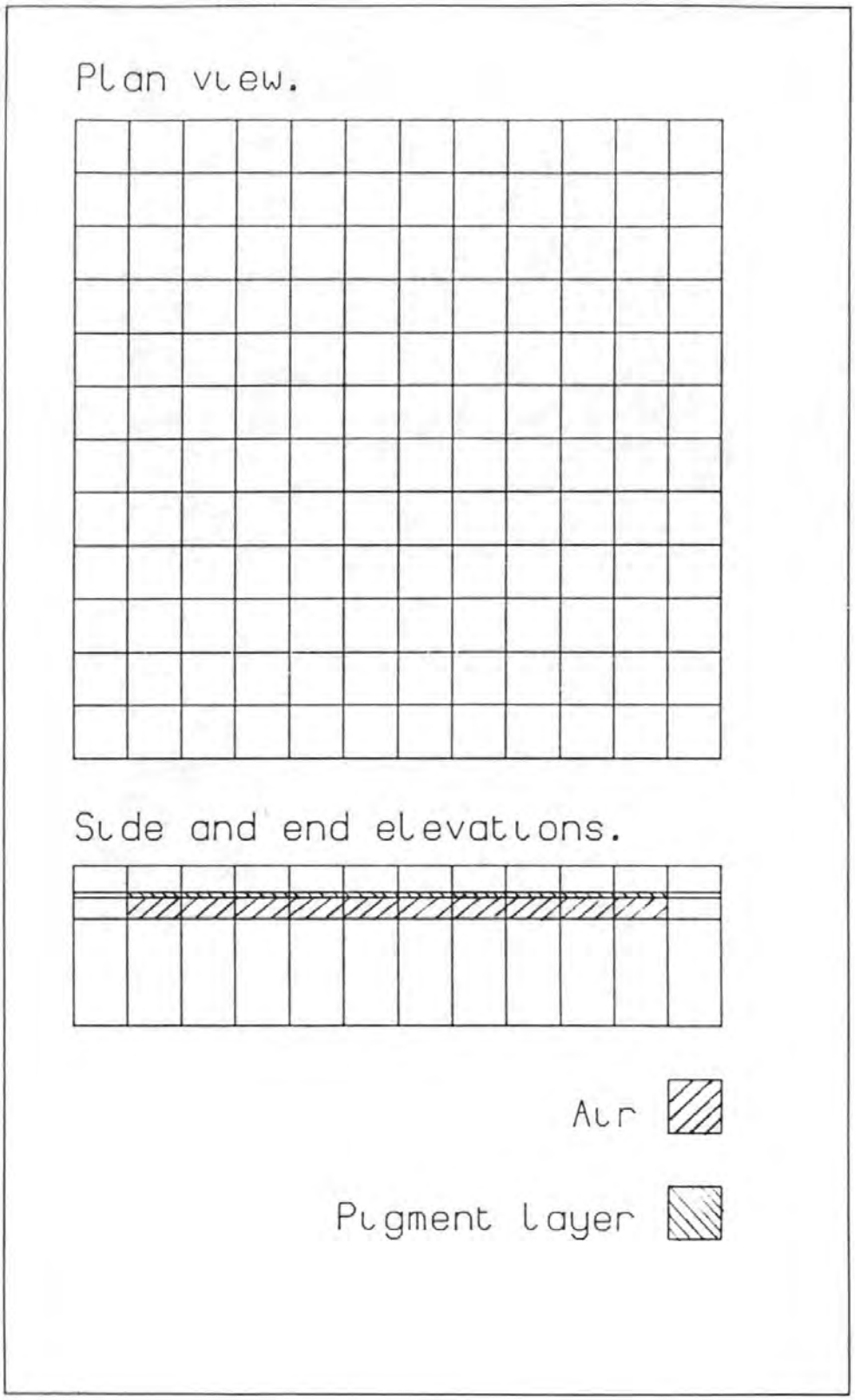

Figure A4.1

Mesh Constructed For Finite Element Analysis.

is somewhat larger than the chip tool contact zone in the majority of cutting tests described in the experimental sections, and the square geometry is a very basic approximation. However, for the purpose of studying the effect of the paint layer on the temperature distribution through the bulk of the insert tool, the geometry of the heat input is not of primary importance.

Two sets of steady state solutions were obtained.

In the first all material in the tip was assumed to be high speed steel.

In the second, thermal properties of air and paint were assigned to those elements indicated in figure A4.1.

Temperature contours were evaluated for a plane corresponding to the lower (visible) surface of the pigment layer in the painted tool, and the equivalent surface in the unmodified tool. These are presented in figures A4.2 and A4.3.

Two effects of introducing a pigment layer are illustrated. Significant elevation of temperatures around the tool nose occurs, and the area of elevated temperature is extended into the bulk of the insert.

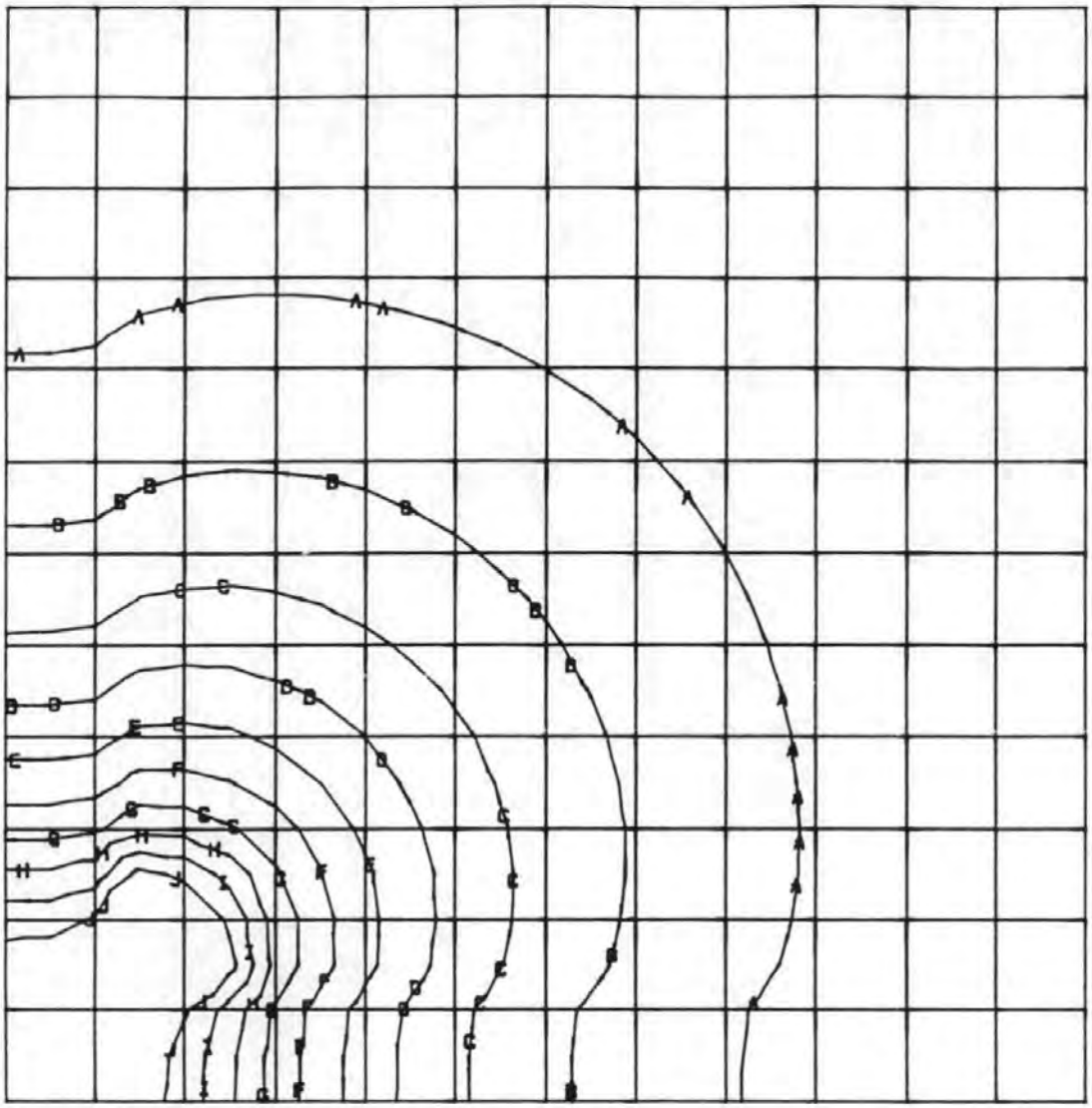

TEMP FIELD / 10^2	
A	0.53
B	0.76
C	0.99
D	1.22
E	1.45
F	1.69
G	1.92
H	2.15
I	2.38
J	2.62

Figure A4.2

Temperature Distribution Calculated Over The Lower Side Of The Pigment Layer.

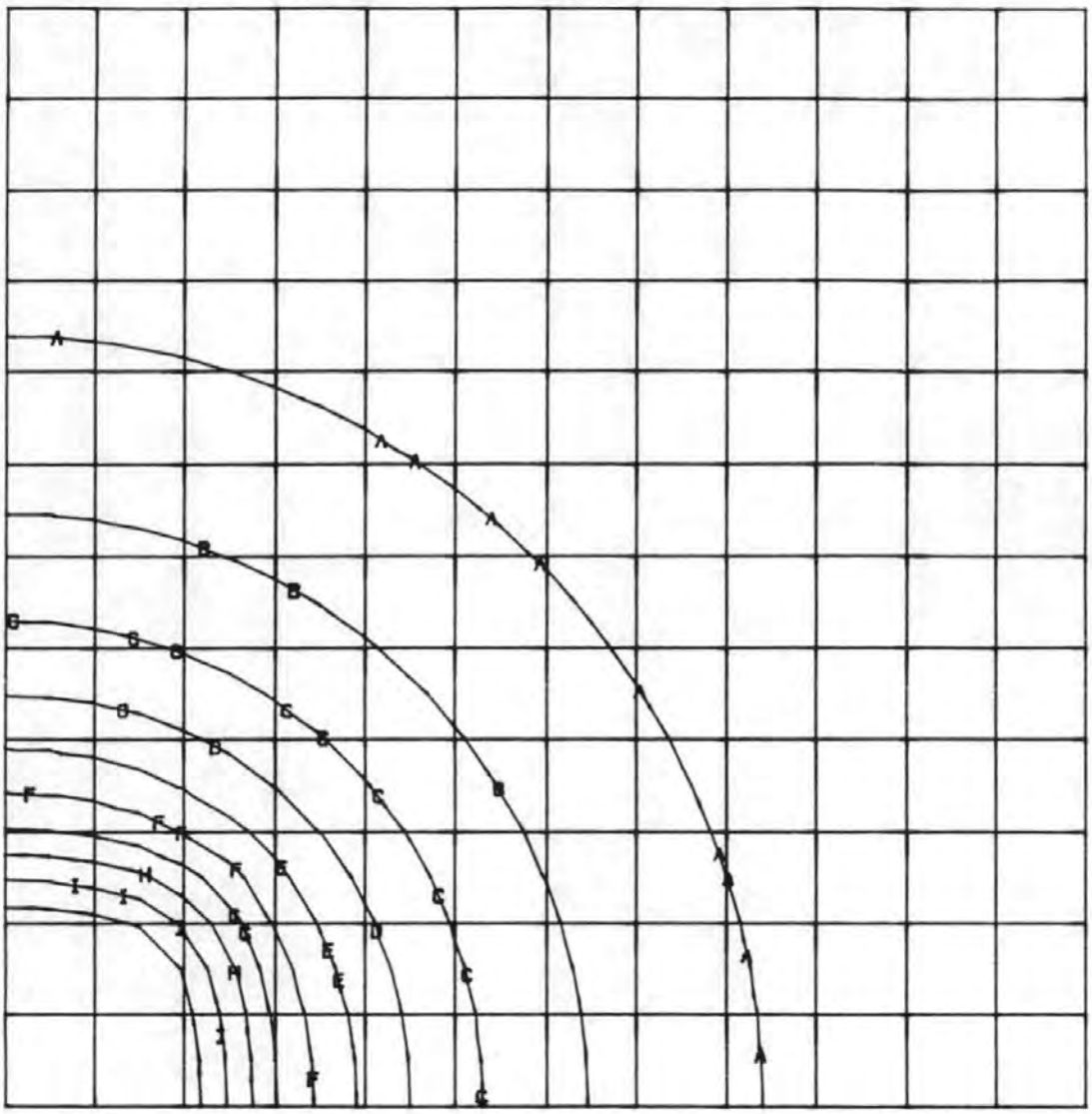

TEMP FIELD / 10^2	
A	0.46
B	0.64
C	0.82
D	1.00
E	1.18
F	1.36
G	1.54
H	1.72
I	1.90
J	2.08

Figure A4.3

Temperature Distribution Calculated Over The Equivalent Plane In The Unmodified Tool.

This effect is of importance if temperature distributions are to be measured using temperature sensitive paints. In addition, temperature contours in the painted tool no longer describe circular arcs.

For these reasons only approximate temperature distributions in unmodified tools may be inferred from information gathered using temperature sensitive paints and this method.

Appendix 5. Experimental Results.

Feedrate Tests.

F = Feedrate (mm/rev).

Ft = Mean steady state tangential force (Newtons).

Fl = Mean steady state longitudinal force (Newtons).

Fr = Mean steady state radial force (Newtons).

T = Mean steady state thermocouple temperature (deg.C).

() = Steady state standard deviation.

F	Ft	Fl	Fr	T
Untreated.				
0.2	610 (15)	360 (25)	254 (9)	178
0.4	1033 (28)	517 (24)	462 (11)	259
0.6	1483 (29)	707 (22)	794 (17)	336
0.8	1843 (34)	760 (31)	1050 (39)	368
1.0	2285 (35)	843 (35)	1262 (52)	396
1.2	2645 (28)	876 (23)	1521 (32)	426

F	Ft	Fl	Fr	T
70 seconds.				
0.2	647 (16)	412 (22)	274 (8)	180
0.4	1206 (29)	674 (26)	532 (21)	322
0.6	1585 (28)	771 (22)	773 (27)	378
0.8	1940 (28)	828 (27)	1026 (19)	411
1.0	2337 (89)	875 (27)	1274 (42)	433
1.2	2711 (50)	908 (36)	1538 (34)	459
140 seconds.				
0.2	640 (19)	398 (21)	270 (10)	184
0.4	1191 (29)	649 (22)	498 (12)	276
0.6	1610 (26)	769 (24)	748 (27)	331
0.8	1938 (29)	810 (32)	1012 (32)	362
1.0	2287 (65)	838 (52)	1273 (58)	385
1.2	2756 (54)	942 (35)	1541 (36)	421
310 seconds.				
0.2	674 (20)	427 (25)	266 (12)	171
0.4	1253 (18)	709 (17)	508 (12)	265
0.6	1655 (24)	809 (27)	758 (27)	321
0.8	2060 (23)	881 (28)	1024 (25)	358
1.0	2493 (33)	956 (42)	1310 (73)	396
1.2	2905 (42)	1027 (45)	1601 (49)	428

F	Ft	Fl	Fr	T
610 seconds.				
0.2	712 (15)	451 (23)	274 (10)	180
0.4	1290 (38)	745 (40)	536 (20)	298
0.6	1777 (22)	900 (23)	822 (20)	353
0.8	2187 (27)	970 (41)	1080 (28)	382
1.0	2595 (35)	995 (44)	1307 (62)	396
1.2	3055 (38)	1113 (38)	1652 (53)	435
1210 seconds.				
0.2	1128 (21)	960 (30)	506 (35)	345
0.4	1838 (65)	1378 (85)	791 (42)	432
0.6	2033 (45)	1129 (50)	912 (36)	411
0.8	2335 (48)	1092 (55)	1074 (91)	417
1.0	2645 (34)	1053 (37)	1326 (43)	424

Surface Speed Tests.

S = Surface speed (m/min)

Ft = Mean steady state tangential force (Newtons).

Fl = Mean steady state longitudinal force (Newtons).

Fr = Mean steady state radial force (Newtons).

T = Steady state temperature (deg.C).

S	Ft	Fl	Fr	T
Untreated.				
20	1065 (35)	458 (23)	468 (22)	214
30	1036 (15)	482 (13)	460 (11)	225
40	1105 (22)	599 (16)	547 (16)	339
50	1065 (18)	580 (23)	515 (19)	353
60	1031 (13)	544 (11)	474 (11)	367
70	978 (12)	490 (11)	420 (5)	359
70 seconds.				
20	1020 (46)	463 (21)	424 (15)	228
30	1019 (17)	499 (18)	422 (9)	277
40	1031 (19)	531 (25)	441 (14)	338
50	1037 (17)	556 (19)	455 (11)	372
60	981 (9)	505 (15)	392 (9)	370
70	937 (9)	461 (8)	368 (6)	***

S	Ft	Fl	Fr	T
140 seconds.				
20	939 (30)	423 (17)	368 (20)	223
30	929 (15)	450 (15)	374 (12)	273
40	941 (17)	494 (16)	395 (10)	338
50	937 (13)	509 (18)	383 (10)	311
60	889 (14)	464 (13)	343 (17)	302
70	845 (11)	415 (7)	300 (12)	295
310 seconds.				
20	788 (40)	325 (25)	330 (14)	211
30	839 (20)	405 (20)	348 (13)	267
40	829 (19)	423 (17)	340 (10)	240
50	822 (19)	423 (19)	331 (9)	233
60	856 (17)	444 (16)	309 (10)	228
70	810 (7)	389 (5)	278 (5)	223
610 seconds.				
20	799 (29)	348 (18)	336 (22)	235
30	772 (13)	373 (15)	328 (13)	207
40	806 (20)	424 (21)	352 (17)	198
50	802 (13)	427 (14)	349 (11)	194
60	755 (19)	380 (18)	309 (18)	192
70	711 (6)	328 (5)	264 (4)	190

S	Ft	Fl	Fr	T
1210 seconds.				
20	801 (28)	373 (21)	332 (23)	194
30	788 (11)	382 (13)	322 (9)	188
40	835 (22)	464 (28)	389 (24)	184
50	791 (15)	428 (16)	356 (13)	182

Side Rake Angle Tests.

SR = Nominal side rake angle (degrees).

Ft = Mean steady state tangential force (Newtons).

Fn = Mean steady state component of force acting normal to the rake face (Newtons).

Fl = Mean steady state longitudinal force (Newtons).

Fp = Mean steady state component of force acting parallel to the rake face in longitudinal direction (Newtons).

Fr = Mean steady state radial force (Newtons).

T = Mean steady state thermocouple temperature (deg.C).

() = Steady state standard deviation.

SR	Ft	Fn	Fl	Fp	Fr	T
Untreated.						
-7.3	1183 (34)	---	--- (--)	---	--- (--)	354
-5.7	1294 (23)	1366	807 (34)	946	781 (22)	362
-4.0	1222 (20)	1265	668 (22)	756	672 (16)	351
-3.0	1251 (27)	1287	758 (26)	827	717 (22)	376
-1.6	1331 (19)	---	754 (20)	794	814 (20)	355
1.2	1188 (17)	1176	558 (17)	533	548 (14)	326
3.0	1219 (22)	1187	578 (25)	515	539 (15)	325
4.6	1219 (12)	1170	562 (20)	469	549 (11)	329
6.1	1183 (10)	1123	524 (13)	406	524 (9)	309
8.0	1391 (14)	1290	627 (28)	449	497 (14)	344

SR	Ft		Fn	Fl		Fp	Fr		T
70 seconds.									
-7.3	1239	(26)	1327	767	(26)	945	726	(20)	350
-5.8	1345	(27)	1417	820	(28)	965	792	(29)	361
-4.0	1203	(19)	1243	651	(24)	740	671	(17)	335
-3.0	1267	(22)	1304	753	(32)	821	718	(22)	360
-1.6	1283	(26)	1308	699	(20)	746	671	(13)	351
1.2	1241	(21)	1227	599	(20)	572	575	(13)	324
3.0	1227	(18)	1194	573	(18)	511	548	(13)	311
4.6	1223	(24)	1173	558	(28)	464	550	(10)	322
6.1	1173	(12)	1109	503	(15)	398	505	(12)	313
8.0	1192	(9)	1113	483	(22)	332	459	(9)	328
140 seconds.									
-7.3	1229	(30)	1317	757	(28)	929	708	(20)	355
-5.7	1364	(39)	---	---	(--)	---	---	(--)	367
-4.0	1132	(20)	1172	607	(23)	690	643	(17)	330
-3.0	1268	(25)	1306	754	(40)	824	702	(22)	362
-1.6	1260	(16)	1277	664	(16)	698	642	(13)	337
1.2	1261	(23)	1248	596	(18)	570	540	(13)	312
3.0	1201	(17)	1170	548	(17)	488	529	(13)	306
4.6	1228	(16)	1180	553	(17)	459	533	(10)	314
6.1	1265	(19)	1197	565	(19)	440	508	(12)	317
8.0	1156	(12)	1081	460	(13)	313	439	(9)	315

SR	Ft	Fn	Fl	Fp	Fr	T
310 seconds.						
-7.3	1237 (25)	1322	752 (41)	928	725 (23)	349
-5.7	1296 (34)	1367	768 (36)	911	770 (25)	346
-4.0	1155 (22)	1204	628 (24)	711	649 (16)	331
-3.0	1212 (22)	1246	692 (25)	758	670 (14)	346
-1.6	1228 (17)	1243	627 (16)	661	624 (15)	333
1.2	1315 (16)	1302	629 (21)	602	533 (12)	295
3.0	1206 (14)	1175	559 (18)	498	523 (9)	273
4.6	1247 (18)	1199	550 (17)	453	537 (10)	288
6.1	1050 (10)	1000	413 (11)	308	468 (8)	244
8.0	1223 (13)	1141	495 (15)	338	467 (10)	293
610 seconds.						
-7.3	1231 (29)	1317	757 (34)	931	698 (24)	344
-5.7	1248 (28)	1315	735 (26)	870	721 (23)	340
-4.0	1111 (16)	1148	572 (16)	653	612 (17)	308
-3.0	1204 (21)	1238	692 (20)	756	670 (18)	346
-1.6	1315 (16)	1333	709 (15)	745	636 (11)	345
1.2	1306 (16)	1293	626 (13)	598	522 (9)	304
3.0	1193 (13)	1263	543 (12)	482	510 (9)	279
4.6	1251 (12)	1201	568 (14)	473	525 (10)	312
6.1	1089 (13)	1033	460 (15)	351	477 (8)	278
8.0	1189 (13)	1108	485 (13)	332	455 (11)	310

SR	Ft	Fn	Fl	Fp	Fr	T
1210 seconds.						
-7.3	1264 (26)	1350	766 (29)	948	695 (27)	313
-5.7	1229 (26)	1291	706 (21)	836	715 (24)	301
-4.0	1306 (22)	1350	715 (17)	810	651 (17)	306
-3.0	862 (20)	882	421 (20)	469	567 (16)	247
-1.6	1241 (14)	1257	635 (14)	667	606 (12)	307
1.2	1417 (15)	1401	697 (15)	667	540 (8)	306
3.0	1326 (14)	1291	636 (20)	570	544 (11)	304
4.6	1259 (22)	1213	586 (13)	494	590 (8)	296
6.1	1036 (11)	985	429 (11)	326	469 (10)	250
8.0	1231 (14)	1144	530 (17)	374	479 (14)	296

Appendix 6.

The Effect Of Boundary Heat Flow On Tool Temperature.

In order to investigate the sensitivity of cutting tool temperatures to thermal contact between the insert and tool holder, a simple finite element model was developed.

Results in table A6.1 were obtained using the mesh illustrated in figure A6.1. A heat flux of 600 Watts was applied uniformly over an area 1mm square in the cutting corner to simulate heating during metal cutting (see section 5.1.). (Retrospectively this was rather high, and accounts for the exaggerated surface temperatures calculated).

Thermal contact between the insert and tool holder was modelled as a uniform heat transfer coefficient between the insert base and an underlying body maintained at ambient temperature. Radiative losses were neglected, and all other surfaces were assumed to be perfectly thermally insulated. Although these assumptions will lead to some inaccuracy, the order of the effect of heat transfer may still be established. Thermal properties of the tool material are given in appendix 7.

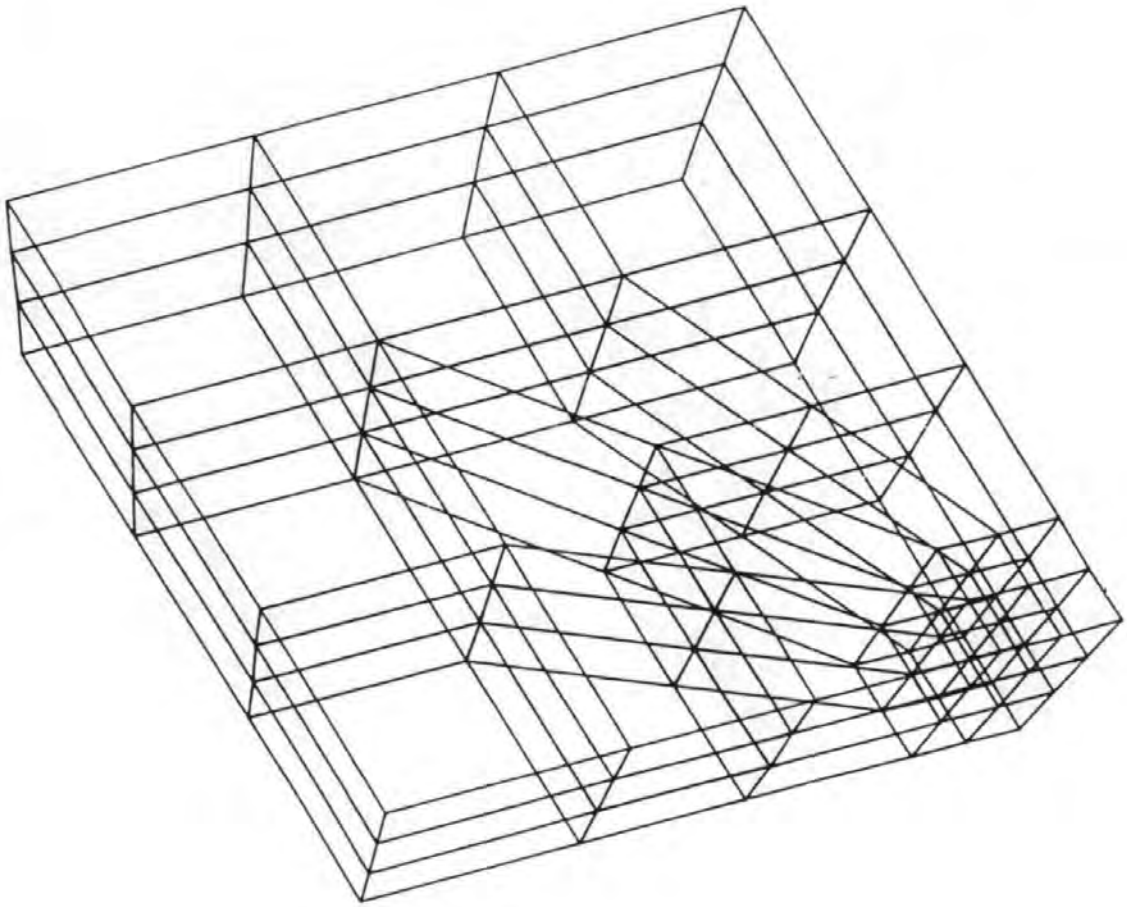

Figure A6.1

Mesh Constructed For Finite Element Analysis.

Figure A6.2 illustrates the sensitivity of steady state tool nose rake face temperatures to the value of the heat transfer coefficient specified at the junction between insert and tool holder.

Clearly an accurate description of the heat transfer characteristics of this boundary must be obtained if temperatures recorded experimentally within the body of the insert are to be used in evaluating the thermal power entering the tool.

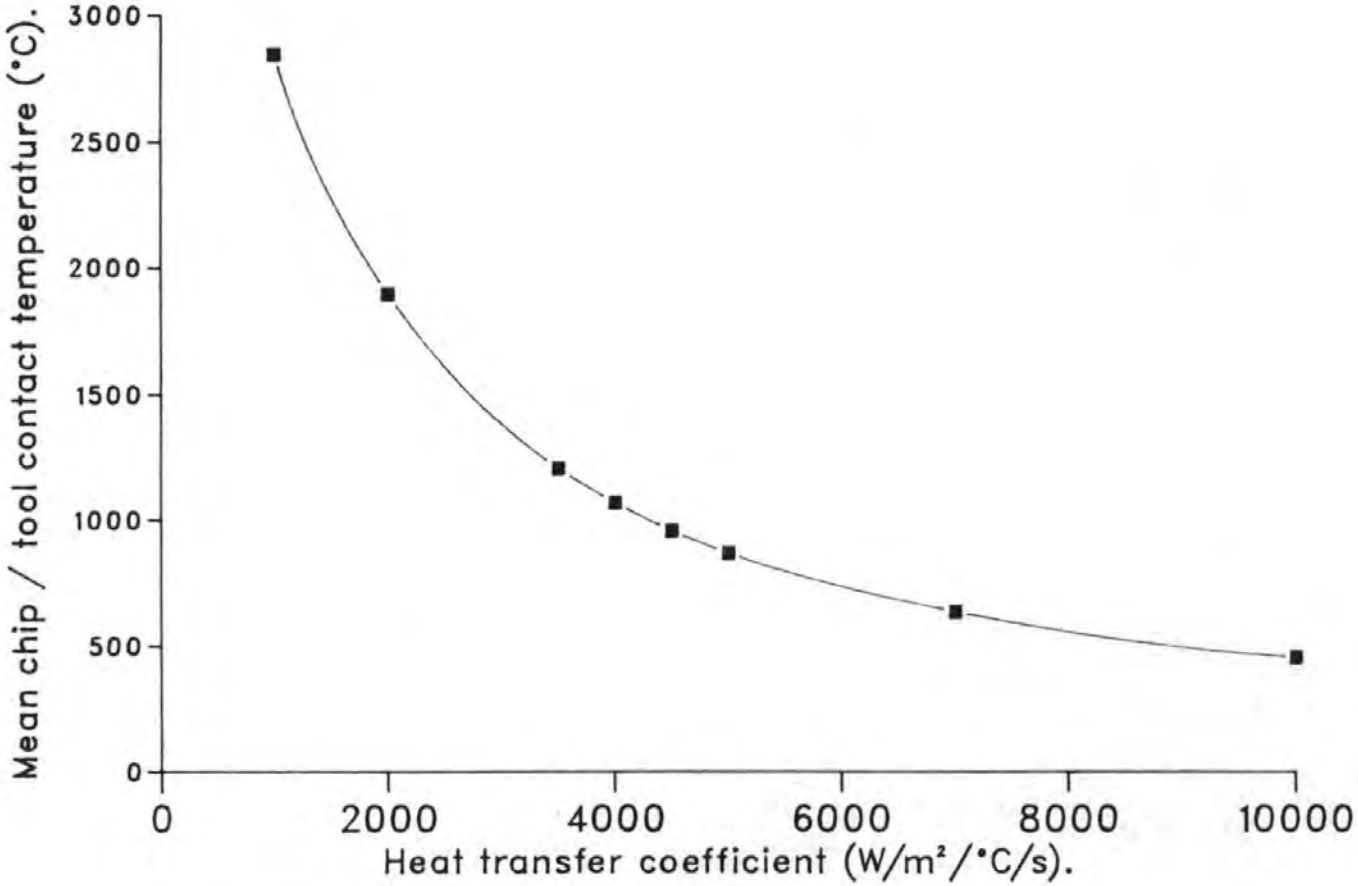

Figure A6.2 Variation In Tool Temperature With Heat Transfer Between Tne Insert Base And Tool Holder.

Table A6.1.

Heat Transfer Coefficients And Corresponding Rake Face Tool Temperatures.

Heat transfer coefficient. ($W/m^2/^oc/s$).	Temperature (^oC).
1000	2847
2000	1899
3500	1207
4000	1071
4500	960
5000	871
7000	637
10000	458

Appendix 7. Thermal Properties Of Materials.

Material	Ro	K	Cp
	(Kg/m^3)	(J/Kg/s/°C)	(J/Kg/ C)
T42	8300	52 at 20 °C	500 [75]
		103 at 700 °C	
Air	1.29	0.024 at 0 °C	1000 [76]
		0.032 at 100 °C	
		0.076 at 1000 °C	
Pigment layer	1000	0.2	1200 [76]

Thermal properties of the pigment layer were estimated from values for acrylic resins.

Appendix 8. Minimum Local Pathlength Method Flow Diagram.

The flow diagram set out below outlines the numeric method adopted to calculate the chip flow angle using the minimum local pathlength method. The value of RS/PR is discussed in section 2.10.2.

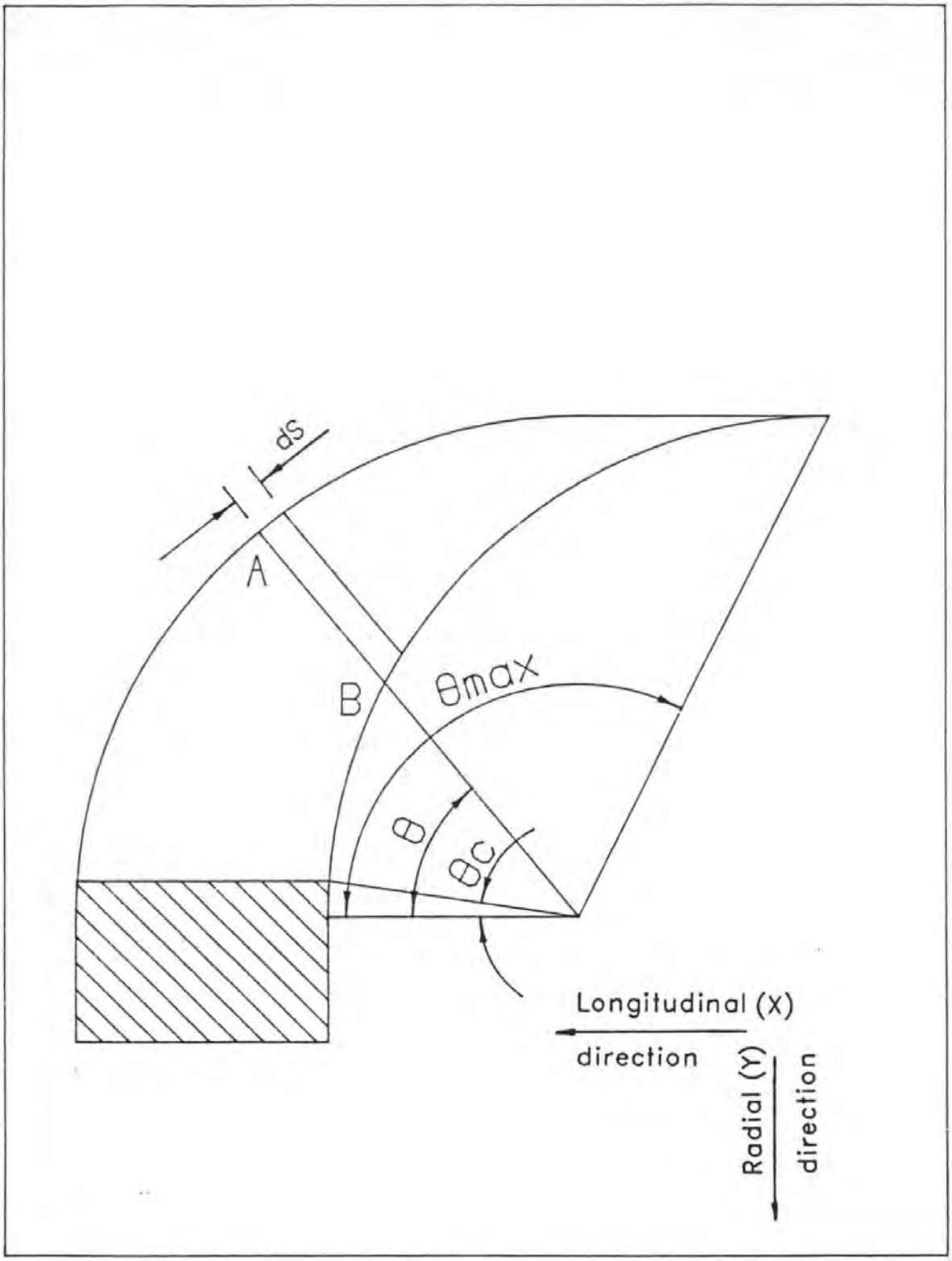

Figure A8.1 The Geometry Of The Minimum Local Pathlength Model.

Input :- Tool nose radius.
Depth of cut.
Feedrate.
Number of intervals, Q.
RS/PR.

↓

Set up equations describing the cartesian co - ordinates of points on the toolnose and workpiece boundary in terms of θ, figure A8.1.

↓

Calculate θc and the area of the undeformed chip undergoing edge effect shear (hatched in figure A8.1) from RS/PR.

All material undergoing edge effect shear ($\theta < \theta c$) flows in the y direction.

↓

Calculate area of undeformed chip flowing in the y direction.

For $\theta > \theta c$, material flows to minimise local pathlengths.

↓

For $\theta = \theta c$ to θmax, (figure A8.1), step $\frac{\theta max - \theta c}{Q}$

↓

(1) Determine the cartesian co - ordinates of A, the point on the toolnose.
(2) Determine the cartesian co - ordinates of B, the point on the workpiece boundary.
(3) Determine Xa - Xb and Ya - Yb.
(4) Multiply by dS, figure A8.1.
(5) Update dX.dS and dY.dS

↓

Next θ.

Determine the overall X and Y components.

$\tan\phi = X/Y$

Appendix 9.

The Effect Of Nitriding On The Thermal Properties Of Insert Cutting Tools.

In order that results from thermal modelling may be applied to nitrided tools, and that cutting temperatures recorded using untreated and nitrided tools may be directly compared, it is necessary to demonstrate that the effect of nitriding on the heat transfer characteristics of cutting tools is negligible.

A one dimensional analysis of thermal diffusivity in a nitrided insert tool is presented below.

Considering an insert tool 3mm thick, nitrided over all surfaces to a depth of 0.3mm, the thermal diffusivity of the complete system may be expressed as

$$\frac{lt}{\alpha eff} = \frac{l1}{\alpha 1} + \frac{.l2}{\alpha 2} + \frac{l1}{\alpha 1}$$

where :- $l1$ = thickness of nitrided (diffusion) layer.

$l2$ = thickness of untreated (core) tool material.

lt = total thickness of insert.

$\alpha 1$ = thermal diffusivity of the nitrided layer.

$\alpha 2$ = thermal diffusivity of the untreated (core) material.

αeff = effective thermal diffusivity of complete section.

The value of $\alpha 2$ is taken to be $1.1\alpha 1$, after [78].

Thus:-

$$\frac{3.0}{\alpha eff} = \frac{0.3}{\alpha 1} + \frac{2.4}{1.1\alpha 1} + \frac{0.3}{1\alpha} = \frac{2.95.\alpha 1}{3.00}$$

$$\alpha eff = \frac{3.00}{2.95} = 1.02.\alpha 1$$

Thus, assuming steady state conditions, the effect of nitriding on measured tool temperatures due to variation in the heat transfer characteristics of the tool material will be negligible.

Appendix 10. A Comparison Of The Global Pathlength Integral and Primary Shear Plane Area

The variation in primary shear plane area with chip flow angle may be studied indirectly using a simpler system exhibiting sufficiently similar properties. The integral of local undeformed chip thickness over engaged cutting edge length (global pathlength integral) is one such system.

The values of chip flow angle minimising the global pathlength integral and primary shear plane area are examined in figures A10.1. The first graph illustrates the variation in primary shear plane area with chip flow angle for the conditions set out in table A10.1.

Table A10.1. Cutting Conditions

Tool nose radius	= 0.8 mm
Feedrate	= 1 mm/rev
Depth of cut	= 1 mm
Rake angle	= 0 degrees
Side approach angle	= 0 degrees
End approach angle	= 0 degrees
Primary shear angle	= 8 degrees

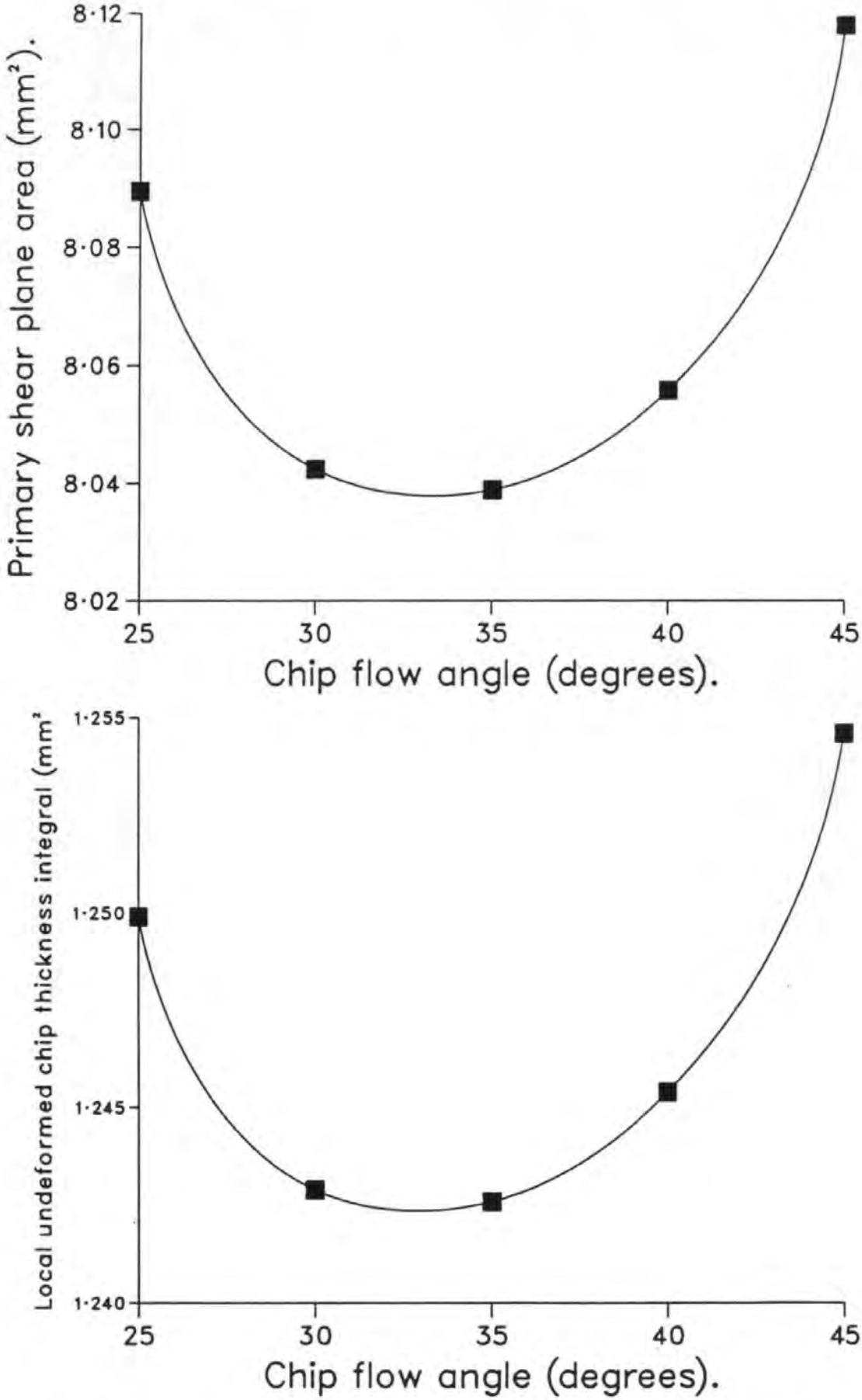

Figure A10.1. Variation In Shear Plane Area and Local Undeformed Chip Thickness Integral With Chip Flow Angle.

(The chip flow angle minimising primary shear plane area is the same for any primary shear angle if all other conditions remain unchanged).

The second graph illustrates the variation in the value of the global pathlength integral with chip flow angle for the conditions set out in table A10.1.

The position of the minimum values of these functions are found to be very similar. This seems to be the case for all examples.

In order to predict chip flow angles it is sufficient to determine the position of the minimum of either function. The integral of local undeformed chip thickness over engaged cutting edge length is the simpler to determine, and the author suggests that this should be used to predict chip flow angles for tools with a nose radius.